Final Report for ONR Grant No. N00014-92-J-1385

CSU Radiation Budget Pilot Study
for TOGA COARE

February 1995

GRAEME L. STEPHENS, Principal Investigator

Prepared for ONR
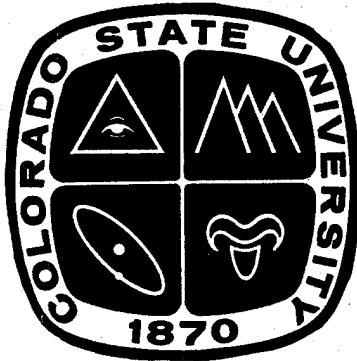
DEPARTMENT OF ATMOSPHERIC SCIENCE

COLORADO STATE UNIVERSITY

FORT COLLINS, COLORADO

19951012 005

FINAL REPORT

CSU Radiation Budget Pilot Study for TOGA COARE

by

Graeme L. Stephens

Department of Atmospheric Science
Colorado State University
Fort Collins, CO 80523

Accesion For		
NTIS CRA&I		☒
DTIC TAB		☐
Unannounced		☐
Justification		
By		
Distribution /		
Availability Codes		
Dist	Avail and / or Special	
A-1		

Funding Agency

February, 1995

DTIC QUALITY INSPECTED 4

REPORT DOCUMENTATION PAGE

Public reporting burden for this collection of information is estimated to average 1 hour per response, including the time for reviewing instructions, searching existing data sources, gathering and maintaining the data needed, and completing and reviewing the collection of information. Send comments regarding this burden estimate or any other aspect of this collection of information, including suggestions for reducing this burden, to Washington Headquarters Services, Directorate for Information Operations and Reports, 1215 Jefferson Davis Highway, Suite 1204, Arlington, VA 22202-4302, and to the Office of Management and Budget, Paperwork Reduction Project (0704-0188), Washington, DC 20503.

1. AGENCY USE ONLY (Leave blank)	2. REPORT DATE 2-10-95	3. REPORT TYPE AND DATES COVERED Final Report 7/1/92 -- 6/30/94

4. TITLE AND SUBTITLE
CSU Radiation Budget Pilot Study for TOGA COARE

5. FUNDING NUMBERS
N00014-92-J-1385 (03-2425)

6. AUTHOR(S)
Graeme L. Stephens

7. PERFORMING ORGANIZATION NAME(S) AND ADDRESS(ES)

Colorado State University
Department of Atmospheric Science
Fort Collins, CO 80523

8. PERFORMING ORGANIZATION REPORT NUMBER

9. SPONSORING/MONITORING AGENCY NAME(S) AND ADDRESS(ES)
Department of the Navy
Office of Naval Research
Resident Representative
University of New Mexico
Banderlier Hall West
Albuquerque, NM 87131

10. SPONSORING/MONITORING AGENCY REPORT NUMBER

11. SUPPLEMENTARY NOTES

12a. DISTRIBUTION/AVAILABILITY STATEMENT

Department of Atmospheric Science
Colorado State University
Fort Collins, CO 80523

12b. DISTRIBUTION CODE

13. ABSTRACT (Maximum 200 words)

A surface radiation pilot study was conducted in the region equatorial western Pacific Ocean in support of the Tropical Oceans Global Atmosphere Coupled Ocean Atmosphere Response Experiment (TOGA COARE). Downwelling infrared and solar hemispheric irradiances were measured at three island sites during a three year period beginning in June, 1991. In December, 1992, stations were deployed at Kavieng, Papua New Guinea and at Darwin, Australia and capability to measure the downwelling hemispheric ultra-violet radiation was added at all sites at this time. Data were transmitted through the GOES Data Collection Platform (DCP) facility from the island sites and sent on computer floppy diskettes from the remaining sites to the Department of Atmospheric Science at Colorado State University, where the data were processed by a quality control algorithm and archived in a publicly accessible ftp computer directory; see Cornwall et al. (1993). The data have been used by universities and by one foreign government research facility. The data were also used by Stephens et al. (1994) to help validate key relationships in deriving a parameter useful for detecting changes in the earth-atmosphere climate system. Except for installation at Kavieng, the performance of the stations was good. Approximately 80% of all possible data have been archived.

14. SUBJECT TERMS
TOGA COARE

15. NUMBER OF PAGES
18 + 3 appendices

16. PRICE CODE

17. SECURITY CLASSIFICATION OF REPORT	18. SECURITY CLASSIFICATION OF THIS PAGE	19. SECURITY CLASSIFICATION OF ABSTRACT	20. LIMITATION OF ABSTRACT
UNCLASSIFIED	UNCLASSIFIED	UNCLASSIFIED	no

Standard Form 298 (Rev. 2-89)

GENERAL INSTRUCTIONS FOR COMPLETING SF 298

The Report Documentation Page (RDP) is used in announcing and cataloging reports. It is important that this information be consistent with the rest of the report, particularly the cover and title page. Instructions for filling in each block of the form follow. It is important to *stay within the lines* to meet *optical scanning requirements*.

Block 1. Agency Use Only (Leave blank).

Block 2. Report Date. Full publication date including day, month, and year, if available (e.g. 1 Jan 88). Must cite at least the year.

Block 3. Type of Report and Dates Covered. State whether report is interim, final, etc. If applicable, enter inclusive report dates (e.g. 10 Jun 87 - 30 Jun 88).

Block 4. Title and Subtitle. A title is taken from the part of the report that provides the most meaningful and complete information. When a report is prepared in more than one volume, repeat the primary title, add volume number, and include subtitle for the specific volume. On classified documents enter the title classification in parentheses.

Block 5. Funding Numbers. To include contract and grant numbers; may include program element number(s), project number(s), task number(s), and work unit number(s). Use the following labels:

C	- Contract	PR	- Project
G	- Grant	TA	- Task
PE	- Program Element	WU	- Work Unit Accession No.

Block 6. Author(s). Name(s) of person(s) responsible for writing the report, performing the research, or credited with the content of the report. If editor or compiler, this should follow the name(s).

Block 7. Performing Organization Name(s) and Address(es). Self-explanatory.

Block 8. Performing Organization Report Number. Enter the unique alphanumeric report number(s) assigned by the organization performing the report.

Block 9. Sponsoring/Monitoring Agency Name(s) and Address(es). Self-explanatory.

Block 10. Sponsoring/Monitoring Agency Report Number. (If known)

Block 11. Supplementary Notes. Enter information not included elsewhere such as: Prepared in cooperation with...; Trans. of...; To be published in.... When a report is revised, include a statement whether the new report supersedes or supplements the older report.

Block 12a. Distribution/Availability Statement. Denotes public availability or limitations. Cite any availability to the public. Enter additional limitations or special markings in all capitals (e.g. NOFORN, REL, ITAR).

> DOD - See DoDD 5230.24, "Distribution Statements on Technical Documents."
> DOE - See authorities.
> NASA - See Handbook NHB 2200.2.
> NTIS - Leave blank.

Block 12b. Distribution Code.

> DOD - Leave blank.
> DOE - Enter DOE distribution categories from the Standard Distribution for Unclassified Scientific and Technical Reports.
> NASA - Leave blank.
> NTIS - Leave blank.

Block 13. Abstract. Include a brief (*Maximum 200 words*) factual summary of the most significant information contained in the report.

Block 14. Subject Terms. Keywords or phrases identifying major subjects in the report.

Block 15. Number of Pages. Enter the total number of pages.

Block 16. Price Code. Enter appropriate price code (*NTIS only*).

Blocks 17. - 19. Security Classifications. Self-explanatory. Enter U.S. Security Classification in accordance with U.S. Security Regulations (i.e., UNCLASSIFIED). If form contains classified information, stamp classification on the top and bottom of the page.

Block 20. Limitation of Abstract. This block must be completed to assign a limitation to the abstract. Enter either UL (unlimited) or SAR (same as report). An entry in this block is necessary if the abstract is to be limited. If blank, the abstract is assumed to be unlimited.

Table of Contents

1

List of Tables

List of Figures

3

1.0 Introduction

A surface radiation pilot study was conducted in the region equatorial western Pacific Ocean in support of the Tropical Oceans Global Atmosphere Coupled Ocean Atmosphere Response Experiment (TOGA COARE). Downwelling infrared and solar hemispheric irradiances were measured at three island sites during a three year period beginning in June 1991. In December 1992, stations were deployed at Kavieng, Papua New Guinea and at Darwin, Australia and capability to measure the downwelling hemispheric ultra–violet radiation was added at all sites at this time. Data were transmitted through the GOES Data Collection Platform (DCP) facility from the island sites and sent on computer floppy diskettes from the remaining sites to the Department of Atmospheric Science at Colorado State University, where the data were processed by a quality control algorithm and archived in a publicly accessible ftp computer directory; see Cornwall et al. (1993). The data have been used by universities and by one foreign government research facility. The data were also used by Stephens et al. (1994) to help validate key relationships in deriving a parameter useful for detecting changes in the earth–atmosphere climate system. Except for installation at Kavieng, the performance of the stations was good. Approximately 80% of all possible data have been archived.

1.1 Background of TOGA COARE

The western Pacific Ocean, from 140–180° East longitude and within 10° of the equator, has been identified as an area of interest for investigation of the atmospheric and oceanic interaction with major implications relating to climate change. The observed, nearly continuous sea surface temperature of 28 C or greater, coupled with a highly convective atmosphere and an uncertainty in net surface heat flux of about 80 watts per square meter prompted the planning committee of the TOGA experiment to initiate an intensive field experimental phase referred to as TOGA COARE. A major part of the uncertainty in the heat budget results from a lack of knowledge about the surface radiation budget.

The TOGA program is a major component of the World Climate Research Program (WCRP) which aims specifically at understanding the coupling between the tropical oceans and the global atmosphere. The goal of the program is to determine the extent to which the system is predictable on time scales of months to years and to understand the mechanisms and processes underlying its predictability. The program also aims at to establish the feasibility of modeling the coupled ocean–atmosphere system for the purpose of predicting its variations on time scales of months to years. For complete description of the goals of the TOGA program see Webster (1988).

The magnitude of the fluxes of heat, momentum and water and their spatial and temporal distributions were identified as poorly understood but crucial components of the coupled ocean–atmosphere system and the radiative exchanges at this interface constitutes a principal coupling of the ocean and atmosphere in the western Pacific. In planning for the COARE it was realized that a climatology of the surface radiation budget did not exist for the region which is referred to as the Large Scale Array (LSA) in the remainder of this

report. Therefore it was recommended that a surface radiation budget pilot study be conducted.

1.2 CSU's role in the TOGA COARE SRB

CSU responded to the recognized need for a surface radiation budget pilot study and was selected to deploy instrumentation to begin a collection in the LSA. The goal of CSU's participation was twofold: first, to develop an instrumentation deployment methodology that would lead to a data set of high quality; and second, to begin a compilation of a surface radiation budget climatology for the region. The scope of activity did not extend to the development of new instrumentation since, especially for the collection of broadband solar irradiances, reliable instrumentation existed. Also, for the infrared region, only slight instrument improvements had been achieved over at least the past two decades even though a degree of uncertainty in the overall accuracy of the measurement persisted. Rather, the primary concerns focused on selection of available sites for deployment and the configuration of a robust data collection station capable of withstanding the rigors of the tropical environment. The following sections document the nature of the deployments of the SRBs and the results of the effort.

2.0 Overview of the deployment

A complete summary of the deployment an initial calibration of the instrumentation may be found in the report which comprises Appendix A. The initial deployment took place during the summer of 1991. Based on availability of personnel with even minimal technical expertise stations were deployed on the atoll of Majuro in the Republic of the Marshall Islands at 7°05' N latitude and 171°23' E longitude and the islands of Pohnpei and Chuuk in the Federated States of Micronesia at 6°58' N latitude and 158°13' E longitude and 7°27' N latitude and 151°50' E longitude respectively. Although the sites are all located in the northern third of the LSA, they provide a good sampling longitudinally and benefit from the presence of Weather Station Office (WSO) personnel who are supervised jointly by the US National Weather Service, Pacific Region headquartered in Honolulu, and by an arm of the local governments. In December 1992, stations were deployed at the Bureau of Meteorology Office at Darwin, Australia and at Kavieng, Papua New Guinea. Fig. 1 indicates the locations of the sites (with the exception of Darwin) with respect to the LSA. Also indicated in the figure is the western extent of coverage of the GOES satellite used to transmit data back to the US in a timely fashion from the first three locations. Data were mailed on computer floppy diskettes from the last two locations.
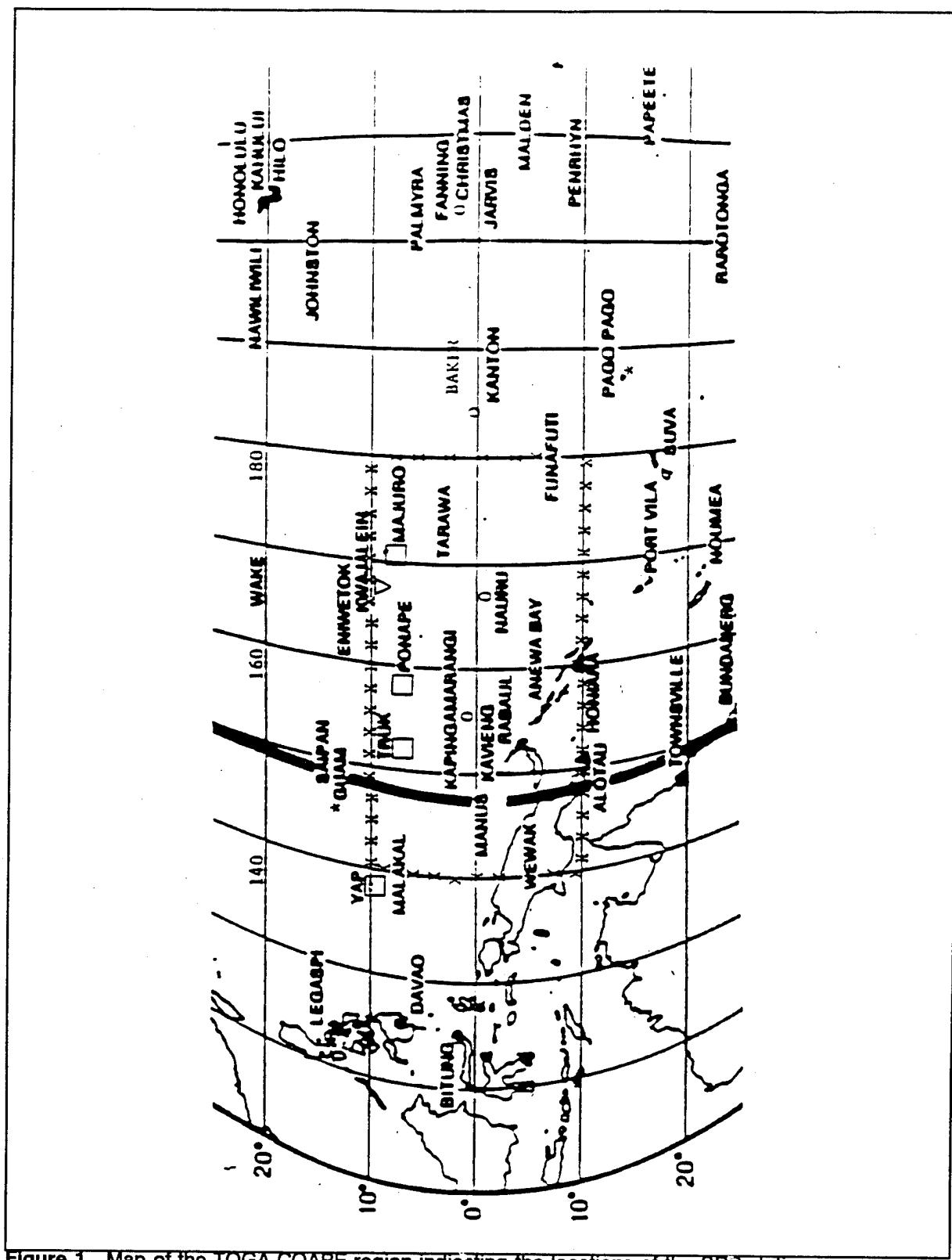
Figure 1. Map of the TOGA COARE region indicating the locations of the SRB stations

2.1 Station configuration

The primary project goals consisted of deploying stations capable of providing accurate measurements of the downwelling total solar and downwelling infrared, hemispheric irradiances and to archive these data for the LSA. All five stations were eventually equipped with the same instrumentation: an Eppley PIR pyrgeometer for measuring hemispheric infra-red (IR) irradiance, an Eppley PSP quartz dome pyranometer for measuring hemispheric solar irradiance, an Eppley ultra-violet (UV) radiometer and a Met-one model 014 wind speed sensor and Handar air temperature sensor to support the IR measurements. The hemispheric instruments were mounted looking upward from a plate on top a sturdy station tripod constructed from 1.25" diameter aluminum pipes. A Handar 540A datalogger, mounted low on the tripod for added stability, was used at the first three sites to record the data from these instruments and transmit that data over the GOES satellite to National Environmental Satellite Data and Information Service (NOAA NESDIS), from where it was accessed via telephone modem.. A Handar WWV radio receiver served to keep the station time correct to insure transmissions fall within allocated GOES transmission windows. Campbell Scientific CR-10 data loggers were used at the last two sites for reasons of economy since there was no opportunity to transmit data over the GOES DCP from these locations. The stations were powered by a solar-charged battery within the datalogger.. Fig. 2 is a photo of an SRB station.

Details on the particular radiometers which were selected, about the calibration procedures and on various other environmental considerations are given in Appendix A.

It is noteworthy that the stations were designed with a field calibration procedure was devised such that the performance of the pyrgeometer could be checked as required. The procedure consisted of a steel thermos that was coated with a high emissivity paint which could be used as a field calibration black body. A thermistor monitored the temperature of the interior wall of the thermos. By placing the thermos, which had been stored in an air conditioned field office, over the dome of the pyrgeometer and allowing the temperature to adjust to ambient, a calibration over a small range of temperature could be performed. This procedure was used early on in the deployments and was instrumental in detecting a problem with the IR data from Pohnpei. More details on the calibration and initial data problems are found in Appendix A. Fig. 3 shows the result of a typical field calibration event.

In October, 1992 the island sites were visited in order to investigate problems with the IR data in Pohnpei and to refurbish supplies at the weather station offices. During the visits the IR and solar radiometers were intercompared with secondary standard instrument taken to the sites.

7
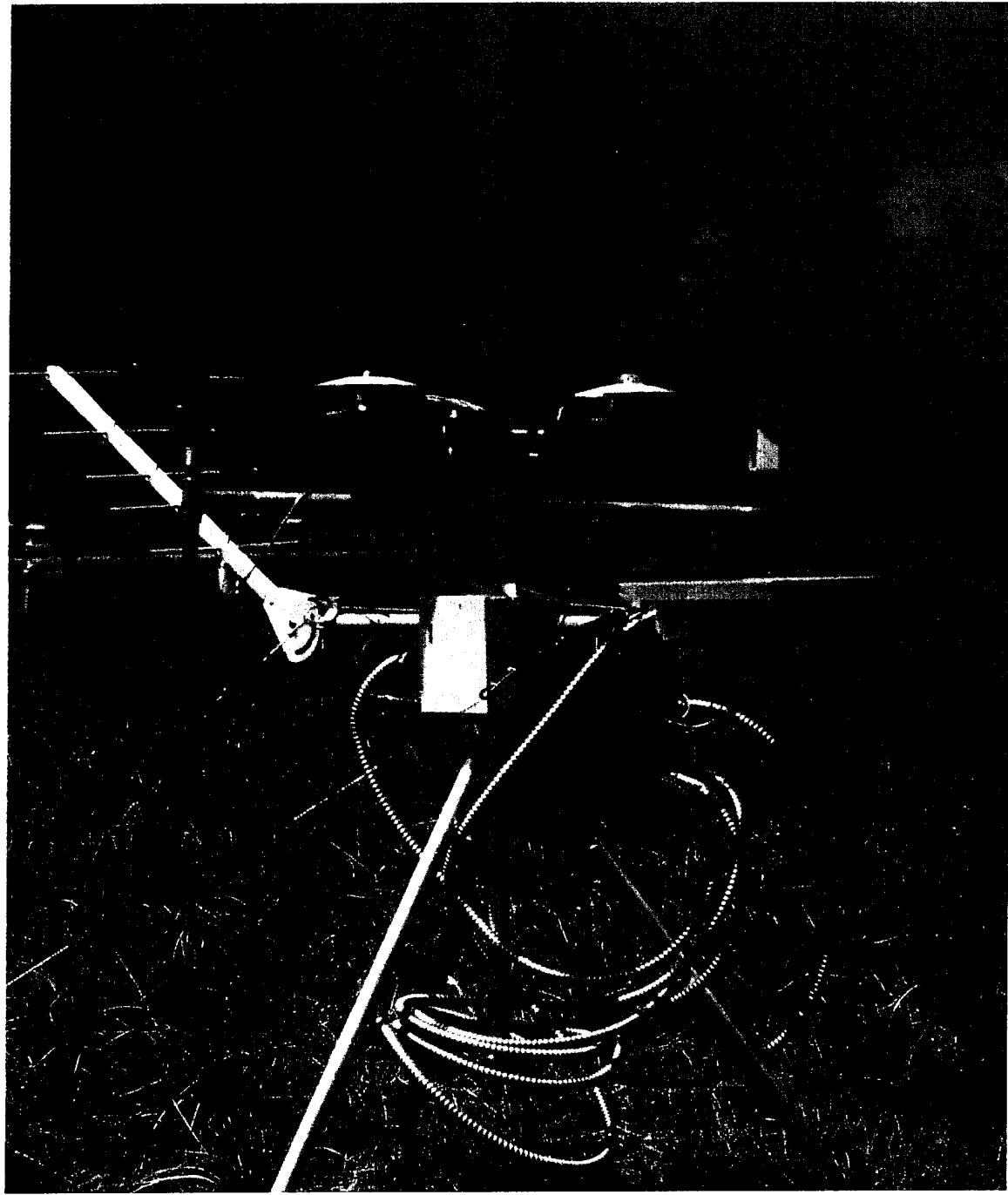
Figure 2. Photo of an SRB station during testing phase at Colorado State University.
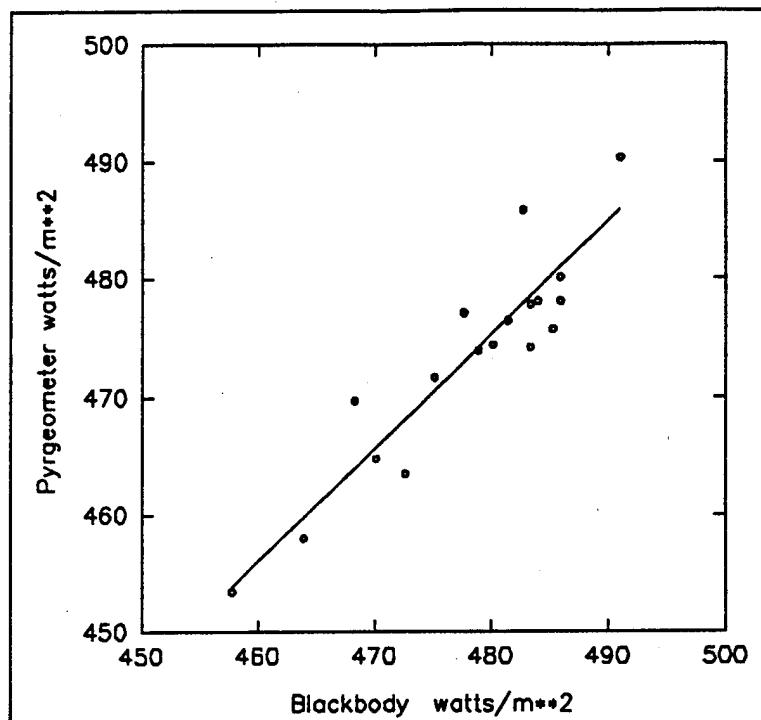
Figure 3. Comparison between the pyrgeometer at Chuuk and the thermos blackbody.
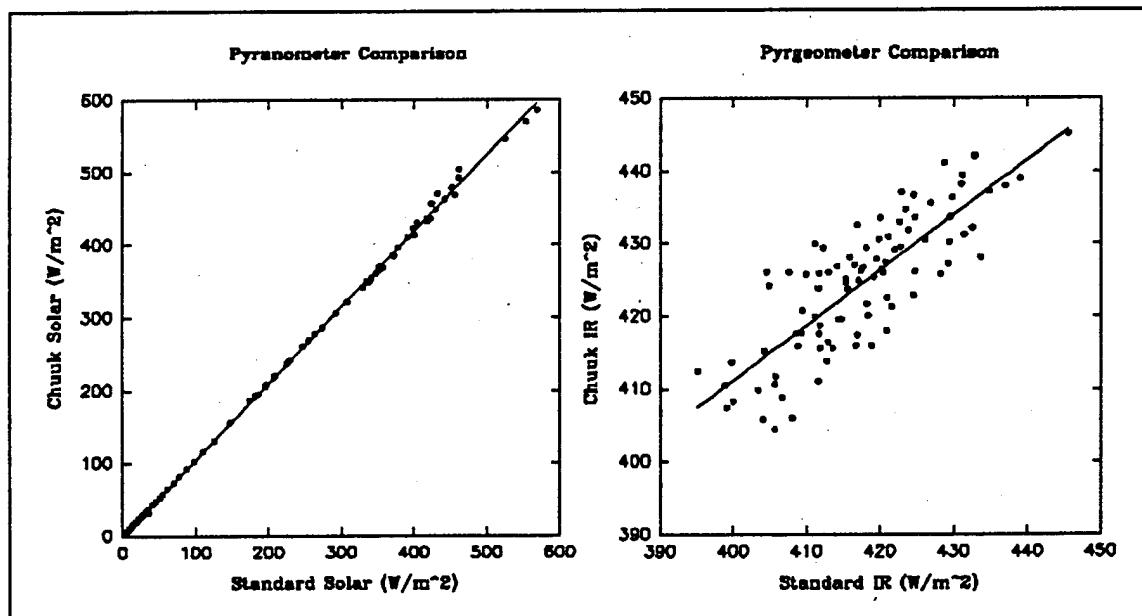

Figure 4. Results of the side-by-side comparison between the radiometers at Chuuk and standard instruments in October, 1992.

Tables 1 and 2 below show comparisons of the average, maximum and minimum values for the intercomparisons.

Pyranometers						
	Standard	Majuro	Standard	Pohnpei	Standard	Chuuk
Mean	552	558	325	334	61.6	63.3
Max	971	981	1397	1339	568	586
Min	0.61	0.60	5.33	5.33	1.78	1.97

Table 1. Comparison of the mean, maximum and minimum values of the standard pyranometer and the pyranometers in the LSA from the side–by–side data.

Pyrgeometers						
	Standard	Majuro	Standard	Pohnpei	Standard	Chuuk
Mean	414	421	422	423	417	424
Max	427	442	463	465	446	445
Min	398	391	391	395	395	404

Table 2. Comparison of the mean, maximum and minimum values of the standard pyrgeometer and the pyrgeometers in the LSA from the side–by–side data.

These intercomparisons established that the fielded instruments were performing within acceptable accuracy specifications.

4.0 Description of the retrieved data

Data were retrieved from the island stations via the GOES DCP facility and from downloads from the Handar data logger onto computer diskette from the island sites and from computer diskette from the sites at Kavieng and Darwin. The GOES data were retrieved three times per week and diskette downloads are performed once each month. The data retrieved from satellite are converted to ASCII and processed through a calibration program. The diskette data are processed separately. Appendix B is the procedural manual that was developed for processing the data. In all cases the quantities of interest are the instantaneous, downwelling, hemispheric solar and infrared irradiance values in watts/m^2. The original uncalibrated instrument output voltages, which were sampled once every three minutes up until October 1992, and once every five minutes thereafter. The data are archived at the Department of Atmospheric Science at Colorado

State University. Processed data are available to the community via an "anonymous ftp" account on a CSU work station. Files containing one month of processed data have been compressed and placed on the account. "README" files are also contained on the account to provide instructions and warnings about the usage of the data. For instructions on obtaining the data the reader may contact Dr. John M. Davis at the Department of Atmospheric Science, Colorado State University, Fort Collins, CO 80523; Tel 303–491–8583.

4.1 Discussion of data quality

There were three major episodes of loss of data quantity/quality. The first of these occurred early on in the IR dataset from Pohnpei. An inspection of the plots for Pohnpei for September of 1991 and subsequent months indicates a continually decreasing IR "emittance." At the onset of the decrease it was believed to be real and to be caused by a drier, clearer atmosphere associated with the El Nino event. This was a logical conclusion in view of telephone conversations with WSO personnel who indicated draught conditions had set upon the region to the extent that drinking water was being shipped in. Also, the signal affected was the thermophile output, which nominally ranges between –0.3 to + 0.2 millivolts. The degradation of this signal occurred at a very slow rate of about –0.1 millivolts per month. However, inspection of the plots reveals this was a continuing hardware induced problem and a reasonable guess as to its onset was sometime in October 1991. Thus all IR data after that should not be used. The problem was corrected during the site visit in October 1992.

The second major problem occurred in the solar data from Majuro. The problem was the result of water accumulation in the Handar data logger unit apparently after a change in personnel at the WSO. Apparently, the desiccant was not changed after the maintenance responsibility was transferred to new personnel. This problem manifested itself in the data after May, 1992. Although the IR data appear to be reasonable after that time some caution should be employed when using that data as well.

The third problem was an almost total data loss from the station at Kavieng. The station operated normally only for a period of three months after which the data station ceased loading new data into its memory. Despite attempts to instruct the operator on reloading the data logger program file, the problem was never corrected. Figs. 6 and 7 show the percentage of data which has been archived from each site over the period from June, 1991 to June, 1994.

As indicated in Fig. 6, there was a total loss of data after December 1993 at the Pohnpei site.

11

Chuuk

Majuro

Pohnpei
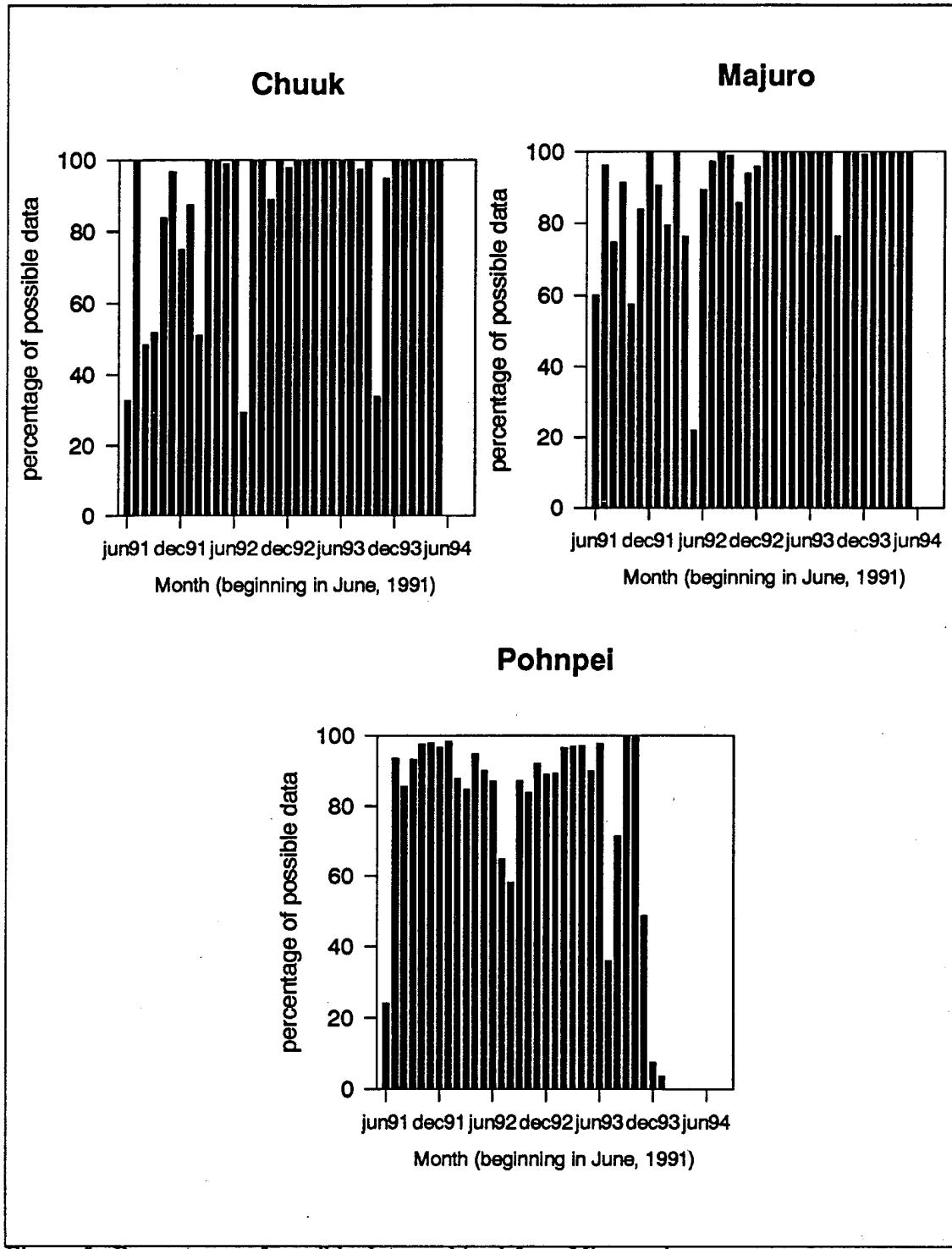
Figure 5. Percentages of possible data archived from Micronesia

12
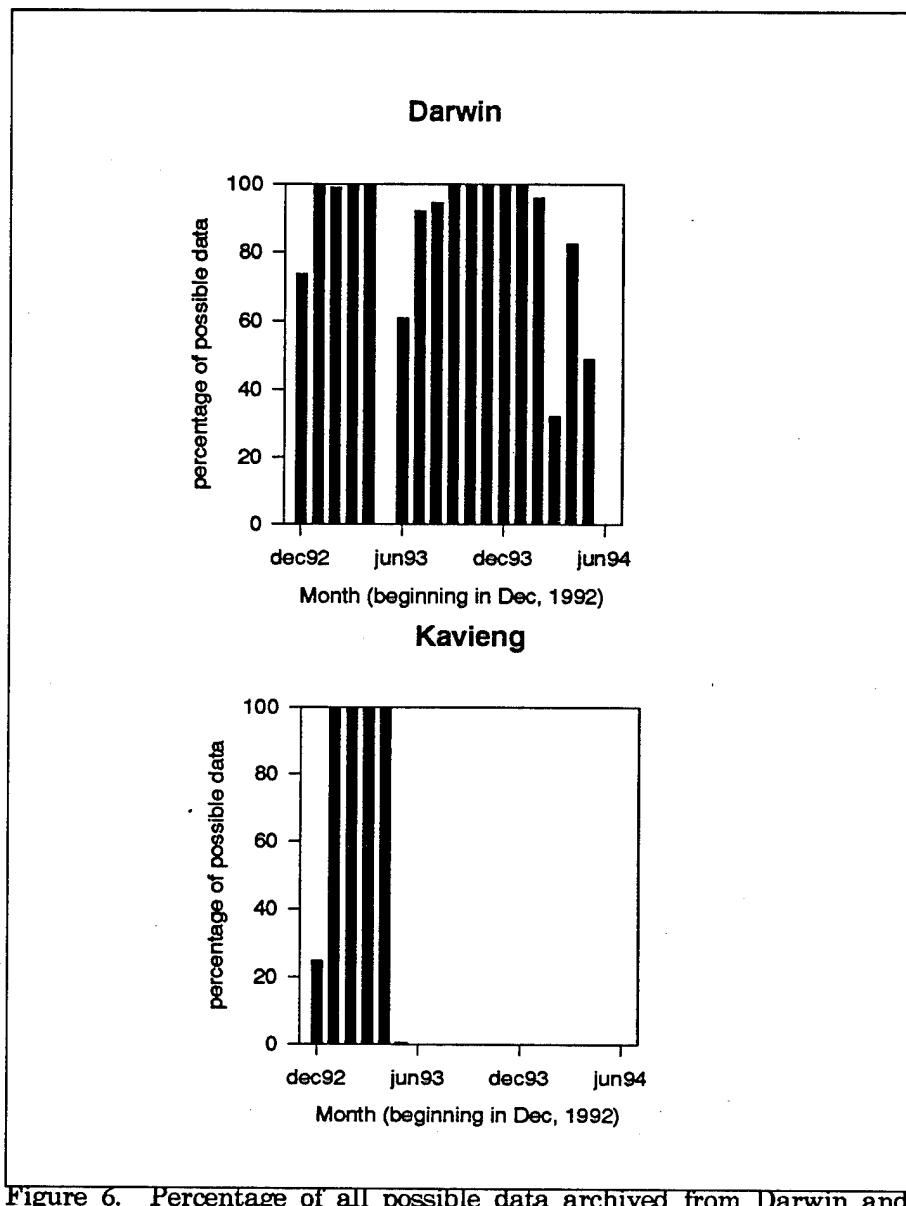
Darwin

Kavieng

Figure 6. Percentage of all possible data archived from Darwin and Kavieng

There were other problems with the data during the period covered by this report. Most of these "glitches" are trapped by the data processing software with the result that the data which are available on the "anonymous" ftp should be as error free as it can be without corroborating measurements. Regarding the large periods of loss of data it is noted that the remoteness of the installations made travel expensive and trips could only be made infrequently. The first maintenance trip was not undertaken until October, 1992. Also, the personnel at the sites had limited technical skills and were reluctant to attempt maintenance procedures. Finally, it is noted that the assistance of the WSO personnel was of a voluntary nature and at times their schedules did not allow immediate attention to the problems with the SRBs.

5.0 Users of the TOGA COARE radiation budget data

Although there is no means of logging all of the accesses to the "anonymous ftp" account on which the radiation data is archived, a few explicit requests have been received and these include:

The University of Hawaii
Scripps Institute of Oceanography
The Pennsylvania State University
The Renewables, Energy Division, The South Pacific Forum, Suva, Fiji

In addition, the data were used to validate relationships between the clear sky downward IR flux and the column integrated water vapor in Stephens et al. (1993,1994) ; see Appendix C. This relationship forms part of a method of diagnosing signals of climate change which result directly from induced changes in the atmospheric branch of the hydrological cycle.

6.0 Acknowledgements

This project was funded by the Office of Naval Research under Contract No. NOOO14–91–J–1422,P00002. We are pleased to acknowledge the cooperation of the National Weather Service Pacific Region for their assistance in coordinating operations with the local governments of The Federated States of Micronesia and The Republic of the Marshall Islands. We are indebted to the personnel at the WSOs at Majuro, Pohnpei and Chuuk for their assistance. This effort was also greatly assisted by the Bureau of Meteorology Office at Darwin, Australia. Certainly, without this assistance collection of this archive could not have been achieved.

7.0 References

Cornwall, C. R., C. L. Combs, J. M. Davis, G. L. Stephens, and S. K. Cox, 1993: CSU Radiation budget pilot study for TOGA COARE. Atmospheric Science Report No. 532, Department of Atmospheric Science, Colorado State University, Fort Collins, CO 80523, 41 pp.

Stephens, G. L., A. Slingo, M. J. Webb, 1993: On measuring the greenhouse effect of earth. NATO ASI Series, Vol. I 9, High Spectral Resolution Infrared Remote Sensing for Earth's Weather and Climate Studies. Springer–Verlag Berlin Heidelberg, 395–417.

Stephens, G. L., A. Slingo, M. J. Webb, P. J. Minnett. P. H. Daum, L. Kleinman, I. Wittmeyer, and D. A. Randall, 1994: Observations of the earth's radiation budget in relation to atmospheric hydrology. Part IV: Atmospheric column radiative cooling over the world's oceans. J. Geophys. Res., **99**, 18,585–18,604.

Webster P. J., 1988: The role of hydrological processes in ocean–atmosphere interaction. In Proc. of the U.S. TOGA Western Pacific Air–sea Interaction Workshop, R. Lukas and P. Webster, eds., USTOGA 8, U. Corp. Atmos. Res., 71–100.

APPENDIX A

Cornwall et al.

CSU RADIATION BUDGET PILOT STUDY FOR TOGA COARE

by: Christopher R. Cornwall, Cynthia L. Combs, John M. Davis, Graeme L. Stephens and Stephen K. Cox

Department of Atmospheric Science
Colorado State University
Fort Collins, CO 80523

Colorado State University

DEPARTMENT OF ATMOSPHERIC SCIENCE

PAPER NO. 532

CSU Radiation Budget Pilot Study for TOGA COARE

by

Christopher Cornwall
Cindy Combs
John M. Davis
Graeme L. Stephens
and
Stephen K. Cox

Department of Atmospheric Science
Colorado State University
Fort Collins, CO 80523

July, 1993

Table of Contents

List of Figures

2

List of Tables

1.0 Introduction

In July 1990, the Department of Atmospheric Science at Colorado State University (CSU) received a grant from the National Oceanic and Atmospheric Administration (NOAA) to deploy Surface Radiation Budget (SRB) measurement stations in a region of the equatorial western Pacific in order to collect data for a pilot study of the radiation budget. The study was performed in support of the Tropical Oceans Global Atmosphere Coupled Ocean Atmosphere Response Experiment (TOGA COARE). This report provides a summary of the activity funded by the grant over the period from October, 1990 when the first funding was received to November, 1992. The purpose of the report is to document the type of instrumentation used, its deployment and calibration history and the quality of the data collected during the period of interest.

1.1 Background of TOGA COARE

The western Pacific Ocean, from 140-180° East longitude and within 10° of the equator, has been identified as an area of interest for investigation of the atmospheric and oceanic interaction with major implications relating to climate change. The observed, nearly continuous sea surface temperature of 28 C or greater, coupled with a highly convective atmosphere and an uncertainty in net surface heat flux of about 80 watts per square meter prompted the planning committee of the TOGA experiment to initiate an intensive field experimental phase referred to as TOGA COARE. A major part of the uncertainty in the heat budget results from a lack of knowledge about the surface radiation budget.

The TOGA program is a major component of the World Climate Research Program (WCRP) which aims specifically at understanding the coupling between the tropical oceans and the global atmosphere. The goal of the program is to determine the extent to which the system is predictable on time scales of months to years and to understand the mechanisms and processes underlying its predictability. The program also aims at to establish the feasibility of modeling the coupled ocean-atmosphere system for the purpose of predicting its variations on time scales of months to years. For complete description of the goals of the TOGA program see Webster (1988).

The magnitude of the fluxes of heat, momentum and water and their spatial and temporal distributions were identified as poorly understood but crucial components of the coupled ocean-atmosphere system and the radiative exchanges at this interface constitutes a principal coupling of the ocean and atmosphere in the western Pacific. In planning for the COARE it was realized that a climatology of the surface radiation budget did not exist for the region which is referred to as the Large Scale Array (LSA) in the remainder of this report. Therefore it was recommended that a surface radiation budget pilot study be conducted.

1.2 CSU's role in the TOGA COARE SRB

CSU responded to the recognized need for a surface radiation budget pilot study and was selected to deploy instrumentation to begin a collection in the LSA. The goal of CSU's participation was twofold: first, to develop an instrumentation deployment methodology that would lead to a data set of high quality; and second, to begin a compilation of a surface radiation budget climatology for the region. The scope of activity did not extend to the development of new instrumentation since, especially for the collection of broadband solar irradiances, reliable instrumentation existed. Also, for the infrared region, only slight instrument improvements had been achieved over at least the past two decades even though a degree of uncertainty in the overall accuracy of the measurement persisted. Rather, the primary concerns focused on selection of available sites for deployment and the configuration of a robust data collection station capable of withstanding the rigors of the tropical environment. The following sections document the nature of the deployments of the SRBs and the results of the effort.

2.0 Overview of the deployment

The initial activity on the project concerned the selection of suitable deployment sites and designing the stations to be both robust and to require as little maintenance as possible. Initial considerations also extended to the development of stations which could be deployed at a remote location and which could operate unattended for long periods of time. This alternative was considered for some time but to date has not been seriously pursued. An examination of the geography of the region, especially the region west of 150° East longitude within the LSA indicated this to be a region of the globe with a paucity of suitable deployment sites. The number of possibilities is even smaller if it is required that personnel with some technical ability be available to participate. After some investigation the following sites were selected; they are the atoll of Majuro in the Republic of the Marshall Islands at 7°05' N latitude and 171°23' E longitude and the islands of Pohnepi and Chuuk in the Federated States of Micronesia at 6°58' N latitude and 158°13' E longitude and 7°27' N latitude and 151°50' E longitude respectively. Although the sites are all located in the northern third of the LSA, they provide a good sampling longitudinally and benefit from the presence of Weather Station Office (WSO) personnel who are supervised jointly by the US National Weather Service, Pacific Region headquartered in Honolulu, and by an arm of the local governments. Fig. 1 indicates the locations of the sites with respect to the LSA. Also indicated in the figure is the western extent of coverage of the GOES satellite used to transmit data back to the US in a timely fashion.

Recently, two more stations have been deployed in direct support of the COARE, one at Kavieng and one at the Bureau of Meteorology Office at Darwin, Australia; however, these deployments will be documented in a subsequent report. The following subsections detail the configuration of the stations and document the stations' deployment.

5
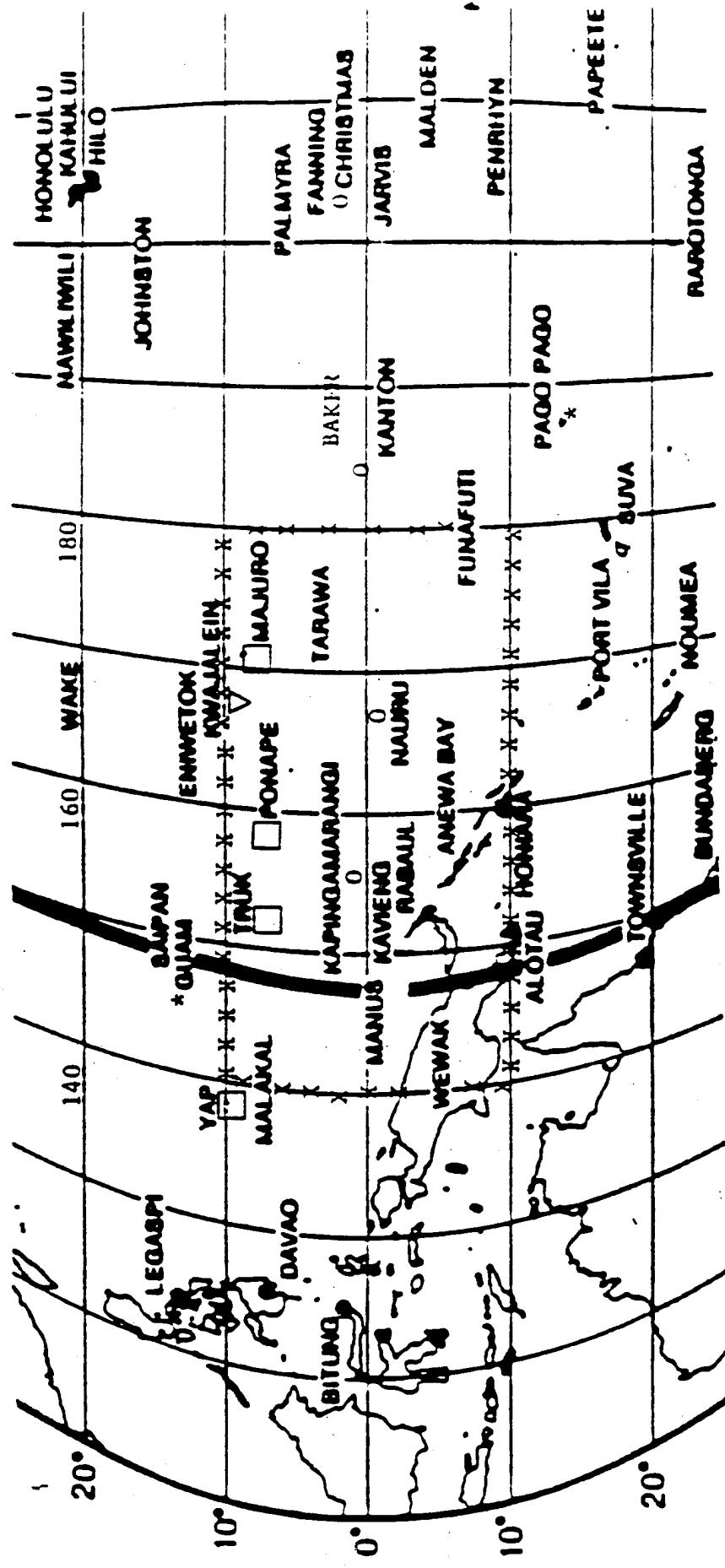
Figure 1. Locations of sites for deployment of SRB stations. The LSA is enclosed in the box bordered by X's. The heavy black line represents the western most coverage of the GOES West satellite.

6

2.1 Station configuration

The primary project goals consisted of deploying stations capable of providing accurate measurements of the downwelling total solar and downwelling infrared, hemispheric irradiances and to begin a compilation of climatologies of these data for the LSA. All three stations are equipped with the same instruments: an Eppley PIR pyrgeometer for measuring hemispheric infra-red irradiance, an Eppley PSP quartz dome pyranometer for measuring hemispheric solar irradiance, and a Met-one model 014 wind speed sensor and Handar air temperature sensor to support the IR measurements. The hemispheric instruments are mounted looking upward from a plate on top a sturdy station tripod constructed from 1.25" diameter aluminum pipes. A Handar 540A datalogger, mounted low on the tripod for added stability, is used to record the data from these instruments and transmit that data over the GOES satellite to National Environmental Satellite Data and Information Service (NOAA NESDIS), from where it can be retrieved. A Handar WWV radio receiver connects to the datalogger and serves to keep the station time correct to insure transmissions fall within allocated GOES transmission windows. The station is powered by a solar-charged battery within the Handar datalogger. Fig. 2 is a photo of an SRB station.

These particular radiometers were selected based on previous experience with the instruments, especially the pyrgeometers; see for example, Albrecht and Cox (1977). Although more recent designs have been introduced for the measurement of terrestrial radiation as in Foot (1986), it appears little is to be gained from the new design at least for ground based installations, and the ruggedness of the new design was unsubstantiated compared to the original Eppley design. Appendix A contains a full listing of the particular instruments deployed and their radiative and electrical characteristics.

The original plan was to utilize satellite transmission as the primary means of retrieving the data. A Memorandum of Agreement between the NOAA NESDIS and the Department of Atmospheric Science at Colorado State University was put in place for the use of two minute data transmission windows every three hours for each SRB location. Official permission to utilize the radio transmitters on site was obtained from the local governments after coordination with the Federal Communication Commission and the US Department of the Interior. Because some data transmission gaps were anticipated the Handar data units were configured with back up memory sufficient to record the data for a period of over one month and laptop computers were included in the complement of equipment at each location for the purpose of downloading the data on an as-needed basis. It was anticipated that moisture collection within the radiometers would be a likely cause of instrument degradation. In order to minimize the frequency at which the internal desiccant would require replenishment a secondary larger desiccant container was included on the platform. The backup reservoirs were filled with 0.5 liters of Drierite brand desiccant and connected by means of plastic tubing to valves inserted into the

7
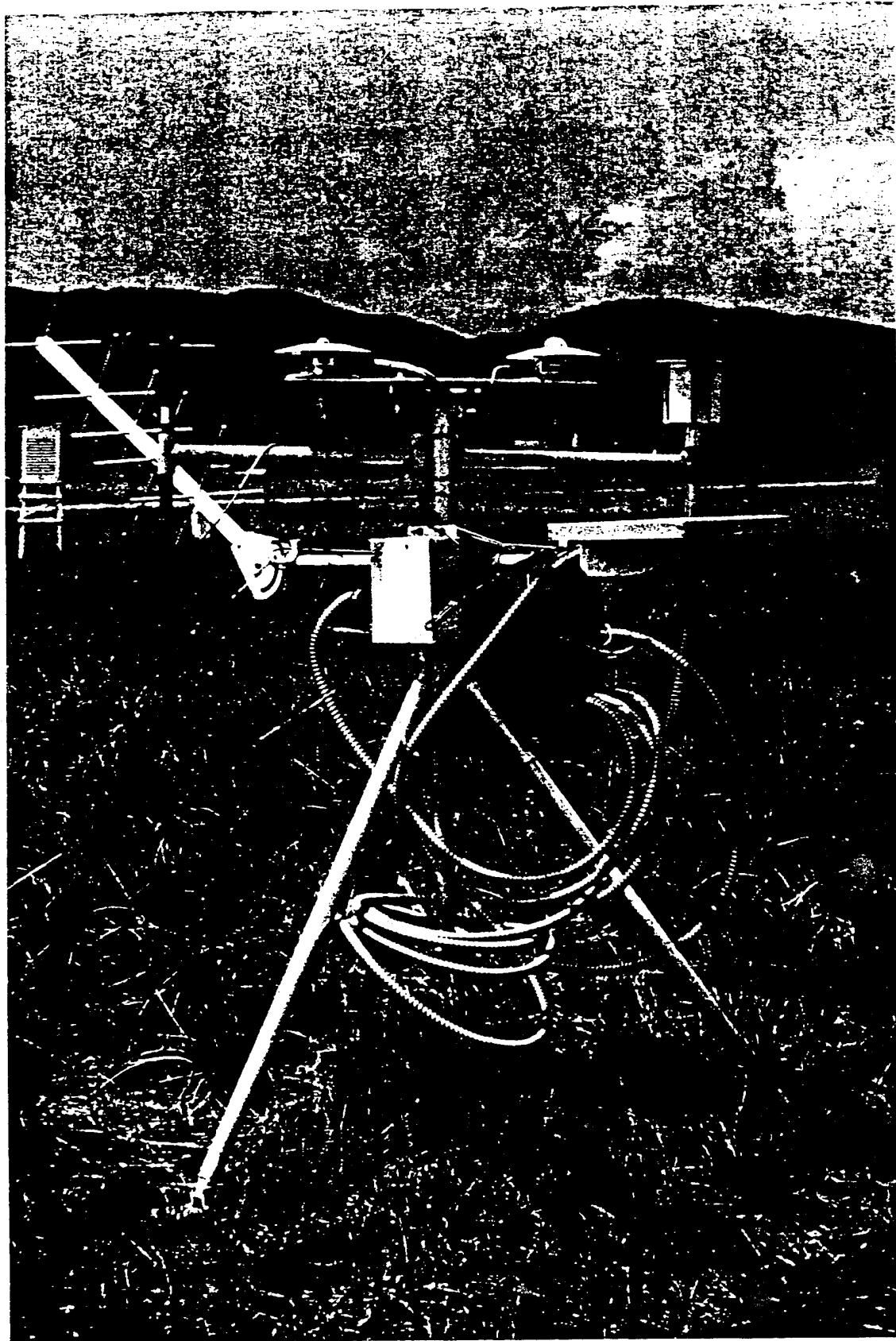
Figure 2. Photo of an SRB station during testing phase at Colorado State University.

bases of the radiometers. The effectiveness of the added system relied on small amounts of differential heating to provide a limited amount of circulation between the radiometers and the backup reservoir. The color of the internal indicating silicagel desiccant could be monitored through glass windows provided for this purpose. Apparently this system is performing well since changes of the internal desiccant are required approximately bimonthly which is much less frequently than previous tropical deployments have required.

Initially data were recorded instantaneously every three minutes and transmitted to the satellite every three hours. This rate of data collection was limited by the length of the two minute satellite transmission window (the data logger was not capable of storing information at a higher density than that used in the satellite transmission sequence). In October, 1992 during a maintenance trip a change in the collection frequency was necessitated by the installation of a UV radiometer. In order to collect the additional information the frequency was changed to one sample every five minutes. More detail on the data set is included in section 4 of this report.

2.2 Initial deployment phase

The tripods were designed and constructed at the Department of Atmospheric Science's Research Testing and Field Operations Facility and the stations configured during the winter of 1990-91. An operations and maintenance manual was written during this period and is available upon request. The radiometers were calibrated (see section 3.0) and the units field tested locally in May of 1991 and taken to the sites in June. The units were designed to be transportable such that each one could be packaged in three specially made boxes and taken as checked baggage on commercial airline flights.

The first station was installed at the Weather Station Office (WSO) of Majuro on June 10 1991. The station was placed in a large grass field on the WSO grounds approximately 60 m from the weather station office. The WSO is located on the outskirts of the small downtown region of Majuro. The radiometers were placed at an elevation of approximately 4 meters ASL and within approximately 200 m of a lagoon. A fence was constructed around the SRB in order to protect it from the curiosity of the locals. Several hours were spent training local weather station personnel on the required maintenance data downloading procedures. Fig. 3 is a photograph of the SRB in place prior to the construction of the fence.

The second station was installed at the NOAA/WPL wind profiler site in the hills outside of town on Pohnpei on June 18, 1991. This site, at an elevation estimated at 70 m, was chosen over the WSO grounds due to the large number of tall trees in town which would have influenced the hemispheric radiation measurements. The profiler site had the required power and security--it is surrounded by a chain-link fence. A four-foot platform was constructed within the fenced area to support the station and to raise the instruments above the level of interference from the building which houses the profiler

9
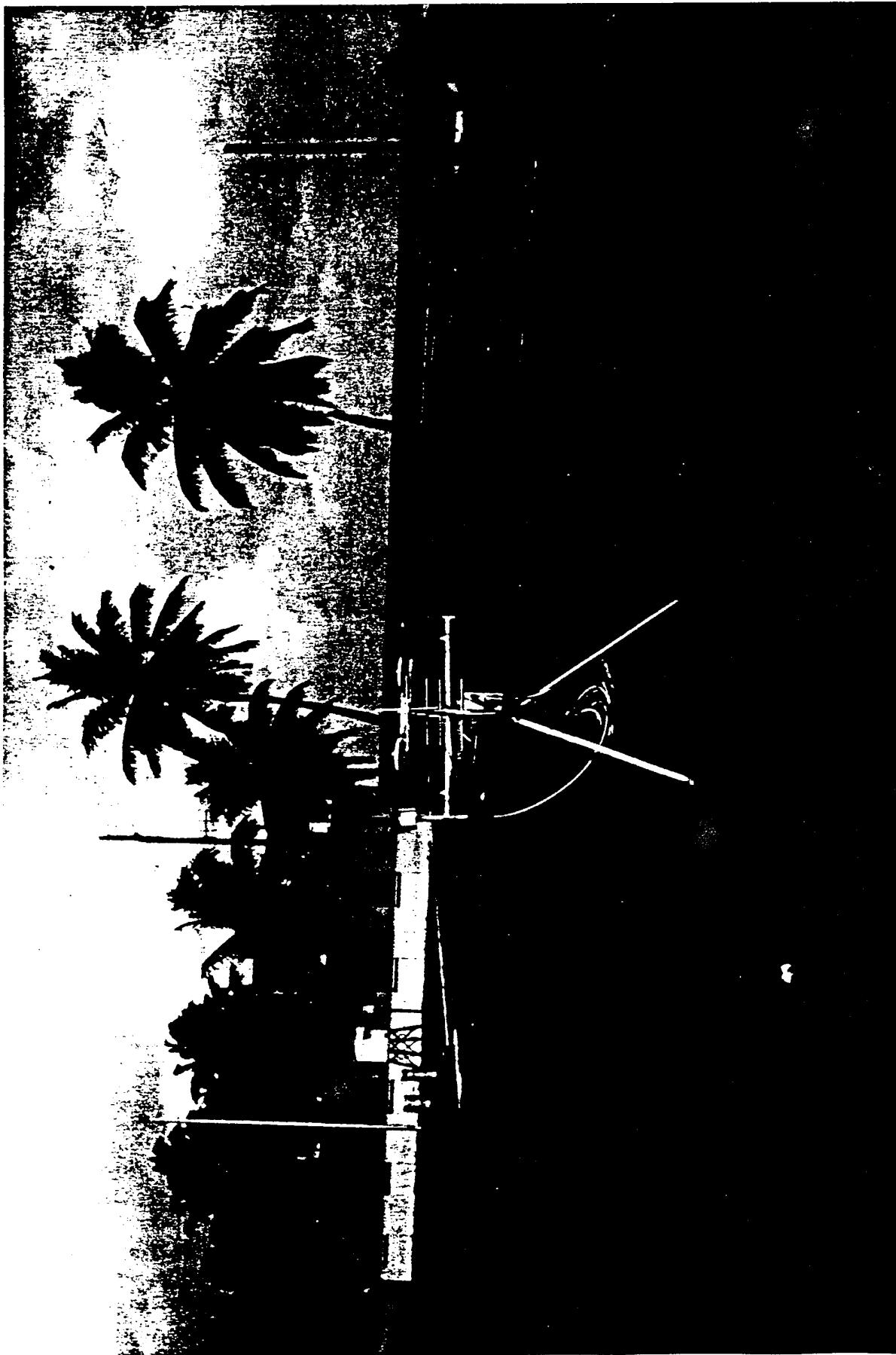
Figure 3. Photo of the SRB station at Majuro as the deployment was nearing completion.

electronics. Fig. 4 is a photograph of the installation at Pohnpei. The local personnel were trained on required maintenance and data downloading procedures.

The third station was installed on the island of Moen in the Chuuk (Truk) Lagoon. This station was also installed on the grounds of the Weather Station Office, located near the south end of the airport runway. The site, at an elevation of 2 m, is enclosed by a fence, and is sufficiently distanced from tall obstructions. No fence or platform was required. The transmission of the data from Chuuk was complicated by the presence of a 700 ft high hill in the line of sight to the satellite's position. This limited the amount of data transmitted from Chuuk to about one quarter of the total amount and required the bulk of the data to be downloaded from the data logger.
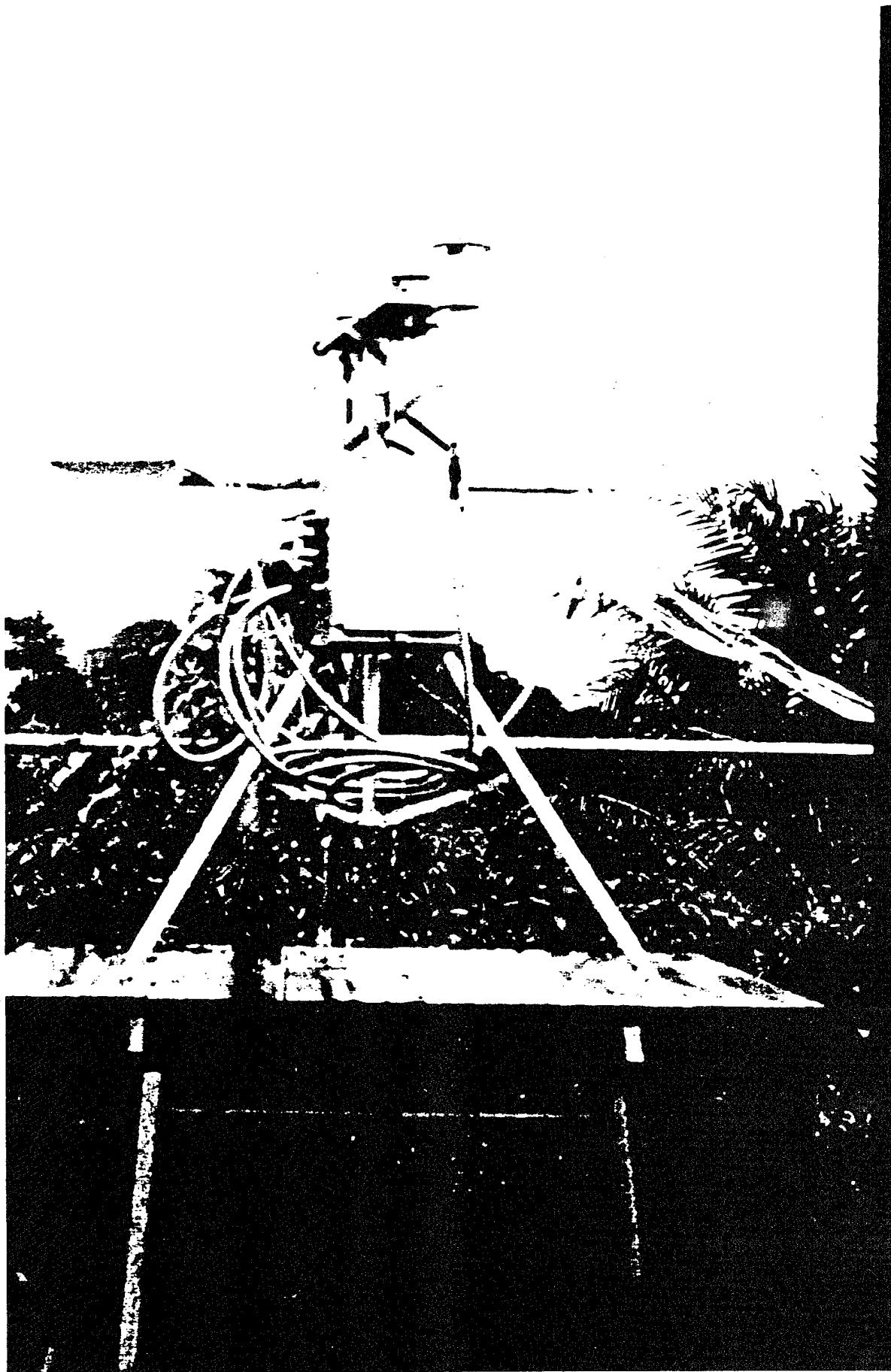
Figure 4. Photo of the SRB station at Pohnpei installed at the NOAA wind profiler site.

12

3.0 Calibration procedures and history

One of the most important yet difficult aspects of a remote deployment of this type is the assurance that the instruments are performing in a known manner. As mentioned above the radiometers were selected partly because they have a proven history of rugged and stable performance. However, the SRB systems include the data system and necessary cabling as well as the radiometers and the durability of the total system operating in a tropical environment had not been established. Thus, some mechanism of testing the system's performance in the field was required. The following sections describe the calibration procedures established to fulfill these requirements.

3.1 Initial calibration

The initial calibrations took place during early spring of 1990. The process included laboratory calibration of the pyrgeometers, intercalibration of pyranometers against standard instruments maintained by NOAA, calibration of data system amplifiers and intercomparison of the data from the stations in side-by-side local deployments.

The laboratory calibrations of the pyrgeometers followed the methodology presented in Albrecht and Cox (1977), whereby the incident longwave irradiance is calculated as one component in a physical model of the radiation budget of the instrument. The model takes into account the emission by the hemispherical filter dome and the thermopile sensor itself. This method of measurement requires that the temperature of the interior of the filter dome and the temperature of the brass case of the instrument, which is assumed to be at the same temperature as the thermopile, be transmitted in the data stream along with the thermopile output voltage. The calibration coefficients for the pyrgeometers are given in Appendix A.

The pyranometers were calibrated by a two stage process in which secondary standards were established by using new pyranometers in a side by side comparison with standard instruments maintained by NOAA, ERL in Boulder, Colorado. The secondary standards were subsequently used to calibrate the instruments deployed in the LSA.

Linear regression coefficients were derived from bench measurements of the amplifiers in the Handar 540A data systems. The amplifiers were found to be linear over the entire operating range to a precision beyond the requirements of the application.

Local field testing was performed in early May, 1991. The SRB stations were set up side-by-side at the Department of Atmospheric Science at Colorado State University in a configuration identical to that of their final deployment. Data were collected via the satellite system over several days and the calibrated outputs of the instruments compared. Overall the daily averages of the pyrgeometers were within 3% of the mean downwelling IR irradiance as measured by all three pyrgeometers. The intercomparison of solar irradiances indicated that the mean irradiances compared to within 2%. The

13

latter value is generally above what is desirable for intercomparison of daily mean solar irradiances; however, the tests were carried out under mostly cloudy conditions. The intercomparisons with the secondary standards were performed under a variety of cloud conditions with results more typical of what was expected; i.e. instantaneous rms deviations within a few percent of respective mean values were obtained.

3.2 Field calibration verification

Provision was made for spot check of the calibration values in the field. Wide mouth stainless-steel thermoses were coated with a high emissivity paint and thermistors of the same type as used in the ambient air sensor were affixed to the interior wall of the container using a high conductivity epoxy. The field procedure was thus kept as simple as possible: on site personnel merely had to place the thermos blackbody over the pyrgeometer, disconnect the ambient air temperature cable at the input to the Handar unit and replace the cable with that from the portable blackbody. The blackbody unit normally would be left in place over the pyrgeometer for a period of a few hours. The personnel were also instructed to place the cup of the thermos over the pyranometer. This procedure serves both as a signal in the data that the calibration was in progress and also indicated if any electrical or serious optical offset had been introduced. Fig. 5 is a plot of a spot check on the calibration performed in late April, 1992 for the pyrgeometer at Chuuk. Spot checks were requested from all three sites when it became obvious that the thermopile at Pohnpei had gradually drifted to negative values outside the normal measurement ranges. At that time it was also found that the pyrgeometer at Majuro disagreed by about 10% from the thermos calibration and the instrument at Chuuk agreed with the thermos blackbody to about 1% in the mean.

It was somewhat fortuitous that the weather station offices were well air conditioned. The blackbody thermoses when carried to the SRB are apparently at a sufficiently low temperature that some range in the spot check calibration data is derived as the blackbody adjusts to ambient conditions. It should be noted that the thermos blackbody devices were not designed to perform a full calibration in the field. The calibration coefficients were never modified as a result of the field checks. It is not known, for example, if the cool starting temperatures of the thermos blackbodies cause condensation within the blackbody or on the pyrgeometer dome. Rather, they were meant to provide indication of problems with the system. From these checks it was determined that the longwave data at Chuuk were acceptable, those at Majuro were questionable and the data from Pohnpei were not valid.

The problem detected with the pyrgeometer instrument at Pohnpei indicates the value of the field spot check. Initially it was speculated that the falling longwave irradiance signal was associated with the onset of an El Nino event in early 1992. Personnel at the WSOs in the region reported a drought in the region to the extent that drinking water was being brought in by ship. It was a natural conclusion that the change in the signal could be attributed to the drier atmospheric conditions and relatively clearer skies.

14
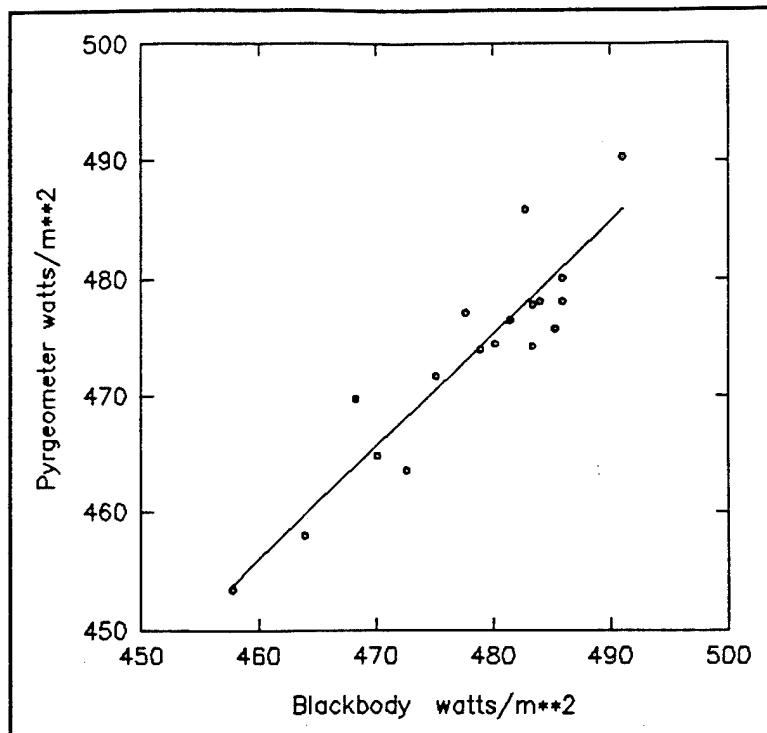
Figure 5. Comparison between the pyrgeometer at Chuuk and the thermos blackbody.

However, after a continued monitoring of these data, it was apparent that the thermopile voltage had begun a slow but continual decrease beginning in October 1991, from values in the range of -0.1 to -0.2 mV to the values of -0.5 Mv or less recorded in spring of 1992.

In October 1992, CSU personnel traveled to the sites to perform repair and refurbishing of the SRBs and to install UV radiometers. Standard instruments were taken to the field for side-by-side comparisons with the field radiometers along with spare radiometers. The radiometers which had been in the field were examined and side-by-side and thermos calibrations were performed. From the information gathered on this trip it became apparent that the problem with the pyrgeometer at Pohnpei was introduced by the data system.

Figs. 6 and 7 show the thermos blackbody calibrations of the pyrgeometers at Majuro and Pohnpei. Although there is scatter of the instantaneous readings the mean values measured by the pyrgeometers at Majuro and Pohnpei agreed with the theoretical emission from the thermos blackbodies to within 0.3% and 0.8% respectively.

15
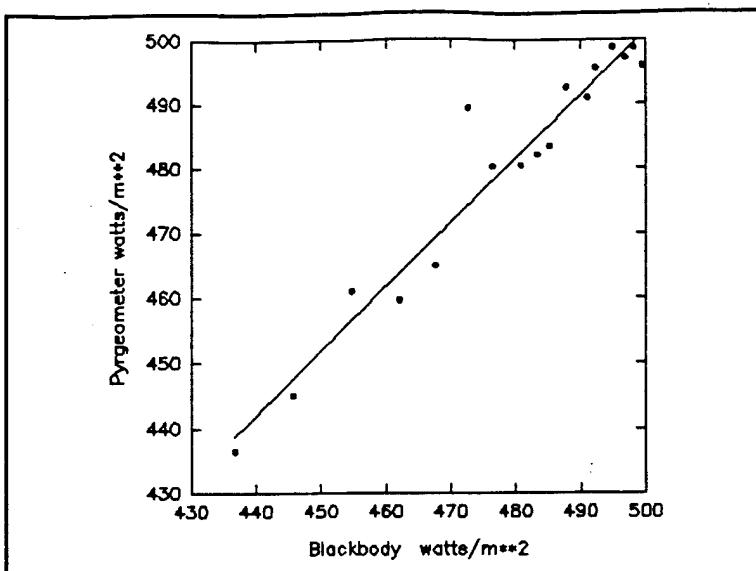
Figure 6. Comparison between the pyrgeometer at Majuro and the thermos blackbody October, 1992.
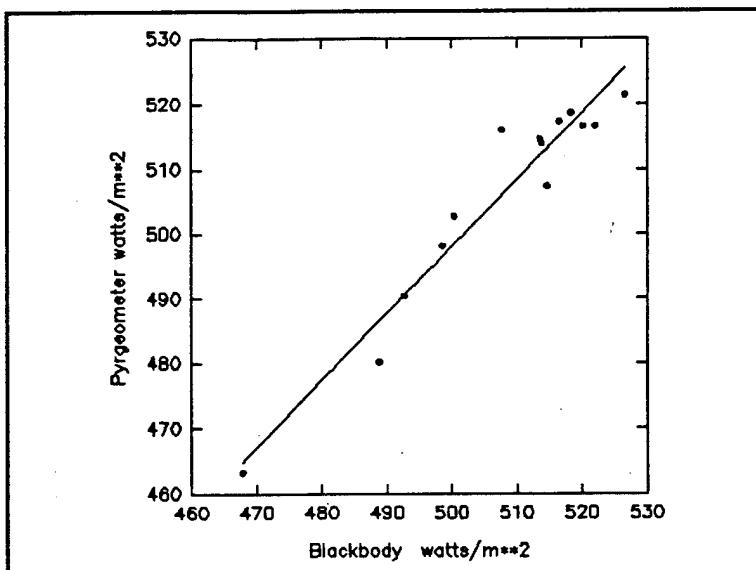
Figure 7. Comparison between the pyrgeometer at Pohnpei and the thermos blackbody during October, 1992.

These plots indicate excellent behavior of the pyrgeometers at Majuro and Pohnpei. The average irradiance values displayed in these plots are 507 and 506 watts m^{-2} respectively for the blackbody and pyrgeometer at Majuro and 485 and 478 watts m^{-2} respectively for the blackbody and pyrgeometer at Pohnpei. A thermos calibration was not performed at Chuuk due to time constraints. Instead one of the standard instruments which had been calibrated before the trip was exchanged for the original radiometer.

16

Side-by-side comparisons between recently calibrated instruments and the field radiometers were completed during the same site visit. Figs. 8 through 10 show the results of the comparisons.
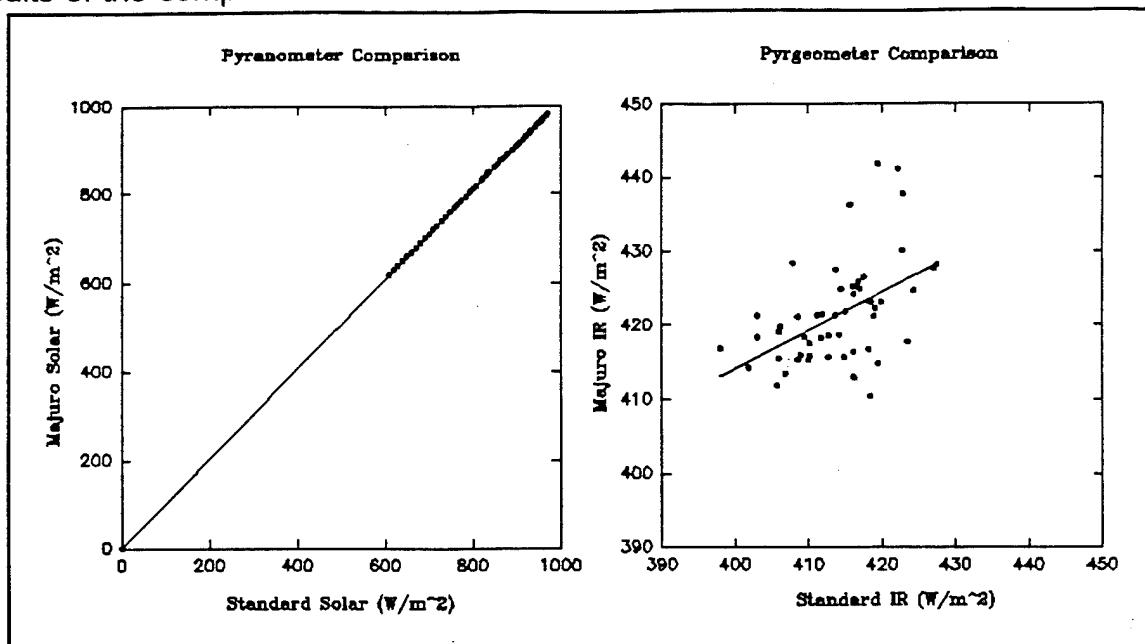
Figure 8. Results of the side-by-side comparison between the radiometers at Majuro and standard instruments in October, 1992
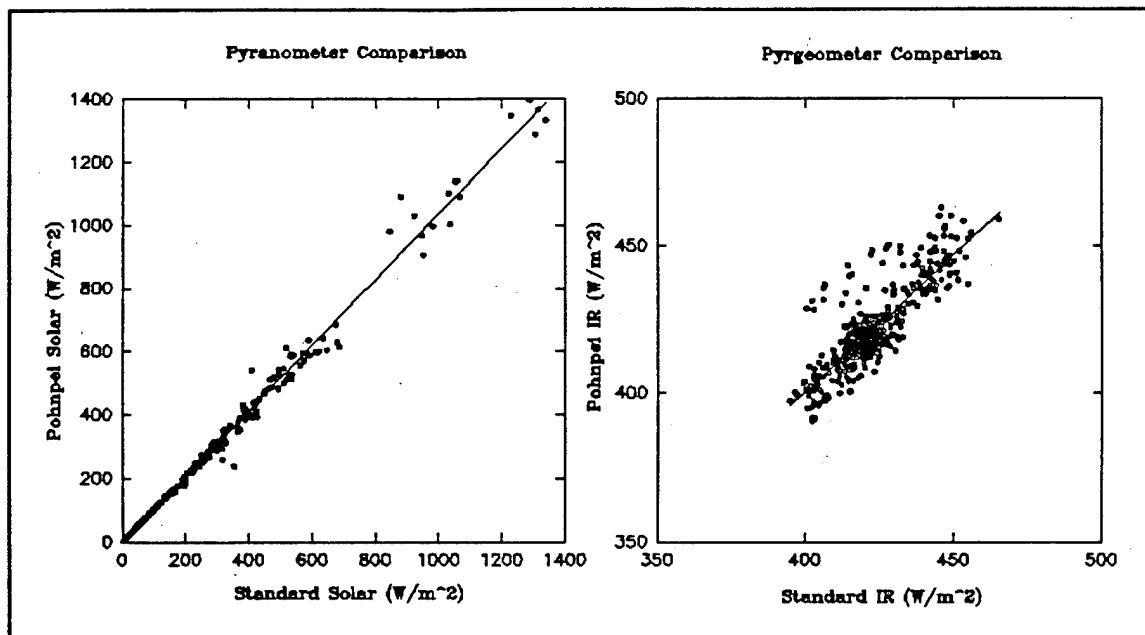
Figure 9. Results of the side-by-side comparison between the radiometers at Pohnpei and standard instruments in October, 1992

17
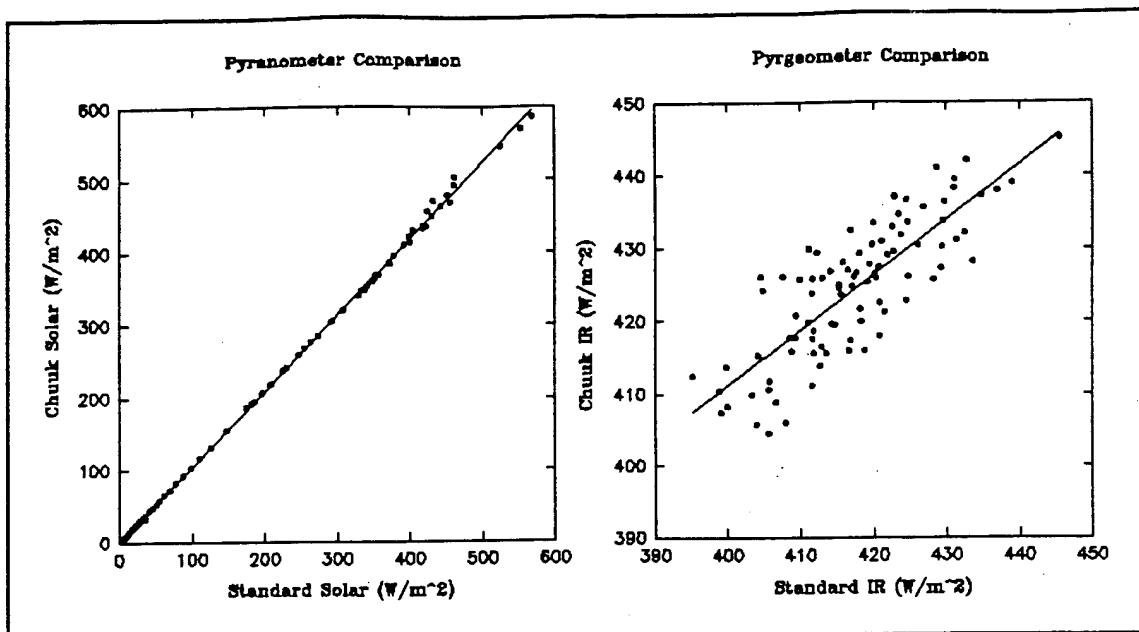
Figure 10. Results of the side-by-side comparison between the radiometers at Chuuk and standard instruments in October, 1992.

Tables 1 and 2 below show comparisons of the average, maximum and minimum values for the data in Figs 8,9 and 10.

Pyranometers						
	Standard	Majuro	Standard	Pohnpei	Standard	Chuuk
Mean	552	558	325	334	61.6	63.3
Max	971	981	1397	1339	568	586
Min	0.61	0.60	5.33	5.33	1.78	1.97

Table 1. Comparison of the mean, maximum and minimum values of the standard pyranometer and the pyranometers in the LSA from the side-by-side data.

18

Pyrgeometers						
	Standard	Majuro	Standard	Pohnpei	Standard	Chuuk
Mean	414	421	422	423	417	424
Max	427	442	463	465	446	445
Min	398	391	391	395	395	404

Table 2. Comparison of the mean, maximum and minimum values of the standard pyrgeometer and the pyrgeometers in the LSA from the side-by-side data.

From the plots of the thermos blackbodies it is clear that any serious malfunction of the pyrgeometer signal can be detected. Thus, we are confident that the use of thermos blackbodies by WSO personnel allows monitoring of the instrument performance of the pyrgeometers without the need of travel to the area.

The side-by-side comparisons were performed over a time period of from 4 to 8 hours. The means presented in tables 1 and 2 indicate that the data are of sufficient quality, when operating normally, to supply the community with at least daily estimates of the solar and IR irradiance values. Thus, if the incoming data stream is carefully inspected for hardware malfunction, a dataset useful for acquiring the daily mean solar and infrared downwelling hemispheric irradiances should be assimilated.

From the intercomparisons it is obvious that the IR data are relatively noisier than the corresponding solar data. Since in each location both the standard and on-site instruments were collocated, it is unlikely that the source of the variability lies in natural variation due to temporal changes in the low level cloudiness, even though it is noted that the instantaneous measurements for these data were separated by a period of four seconds. Fig. 11 below indicates that the noise in the intercomparison data is evident in two of the three terms comprising the total IR value.

The method used to derive the infrared irradiance is taken from Albrecht and Cox (1977). In terms of the calibration coefficients presented in the Appendix A the irradiance is derived as one component of the IR radiation budget of the instrument. The equation describing the assumed behavior of the instrument may be written as;

$$N = k_1 E + \sigma T_s^4 - k_2 \sigma (T_d^4 - T_s^4) .$$

where E is the thermopile voltage in millivolts, σ is the Stefan Boltzmann constant, k_1 and k_2 are the calibration coefficients T_s and T_d are the sink and dome Kelvin temperatures and N is the derived infrared irradiance in W / m^2. The irradiance N is depicted in the upper left portion of Fig. 11, the contribution of the thermopile (the first term on the right of Eq. 1) by the lower left part of Fig. 11, the emission by the thermopile (the second

19
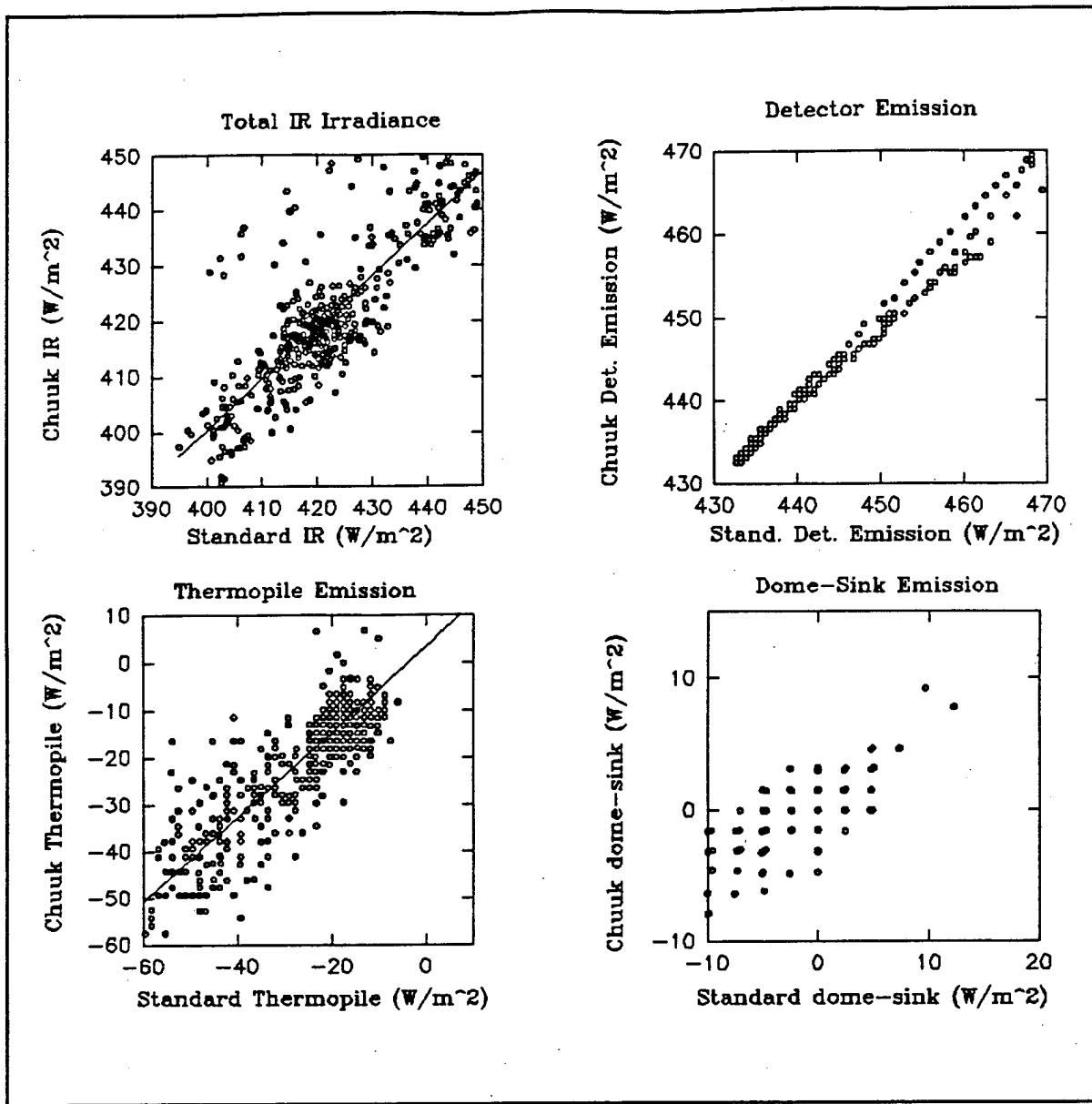
Figure 11. Intercomparison of the components of the IR irradiance from a standard pyrgeometer and the pyrgeometer at Chuuk

term on the right of Eq. 1) by the upper right part of Fig. 11 and the dome-sink emission (last term on the right of Eq. 1) by the lower right portion of Fig. 11. One may conclude that the noise in the signal (at least for this case) is comprised of a good deal of digitization noise, and also that it isn't only the low level (fraction of millivolts) thermopile output which is noisy but the dome temperature as well. Since the operating environments are thought to be relatively noise free in terms of radio frequency emission and the like, the source of the noise is assumed to be associated with the data system; however, to date it has not been feasible to conduct adequate testing of the systems to

minimize the noise level.

4.0 Description of the retrieved data

Data are retrieved from the island stations via the GOES DCP facility and from downloads from the Handar data logger onto computer diskette. The GOES data are retrieved three times per week and diskette downloads are performed once each month. The data retrieved from satellite are converted to ASCII and processed through a calibration program. The diskette data are processed separately. In either case the quantities of interest are the instantaneous, downwelling, hemispheric solar and infrared irradiance values in watts/m^2. The original uncalibrated instrument output voltages, which were sampled once every three minutes for the time period covered by this report, are archived at the Department of Atmospheric Science at Colorado State University so that the data could be reprocessed in the unlikely event that it would become necessary. Processed data are available to the community via an "anonymous ftp" account on a CSU work station. Files containing one month of processed data have been compressed and placed on the account. "README" files are also contained on the account to provide instructions and warnings about the usage of the data. For instructions on obtaining the data the reader may contact Mr. Christopher Cornwall at the Department of Atmospheric Science, Colorado State University, Fort Collins, CO 80523; Tel 303-491-8693.

For those wishing a more cursory inspection of the data, Appendix B contains plots of the diurnal variation of the downwelling solar transmittance and infrared "emittance" averaged over monthly periods. The plots of solar transmittance have been obtained by dividing the instantaneous solar irradiance by the corresponding extraterrestrial quantity and then averaging over the hour and finally plotting the monthly average of the hourly values. A value of 1369 W/m^2 was used for the solar constant. The infrared "emittance" values were obtained by dividing the instantaneous infrared irradiance by the blackbody Stefan-Boltzmann irradiance calculated using the measured ambient temperature. These values were averaged over the hourly periods and then over the month in a manner analogous to the solar data. Fig. 12 provides an example of this type of presentation of the data and a complete set of plots is found in Appendix B.

The reader is cautioned that at the time of preparation of these plots final quality control checks had not been applied to the data. The data should be examined after reading the next section that presents known problems in the dataset.

4.1 Discussion of data quality

There were two major episodes of loss of data quantity/quality. The first of these occurred early on in the IR dataset from Pohnpei. An inspection of the plots for Pohnpei for September of 1991 and subsequent months indicates a continually decreasing IR "emittance." At the onset of the decrease it was believed to be real and to be caused

21
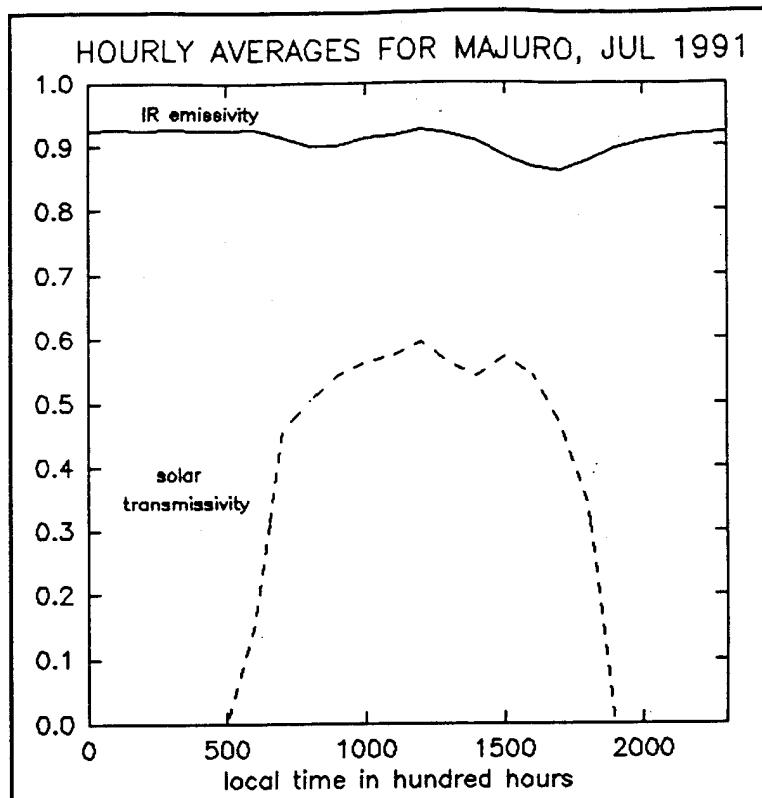
Figure 12. Hemispheric solar transmittance and infrared "emittance" (see text) from Majuro for July of 1991.

by a drier, clearer atmosphere associated with the El Nino event. This was a logical conclusion in view of telephone conversations with WSO personnel who indicated draught conditions had set upon the region to the extent that drinking water was being shipped in. Also, the signal affected was the thermophile output, which nominally ranges between -0.3 to + 0.2 millivolts. The degradation of this signal occurred at a very slow rate of about -0.1 millivolts per month. However, inspection of the plots reveals this was a continuing hardware induced problem and a reasonable guess as to its onset was sometime in October 1991. Thus all IR data after that should not be used. The problem was corrected during the site visit in October 1992.

The second major problem occurred in the solar data from Majuro. The problem was the result of water accumulation in the Handar data logger unit apparently after a change in personnel at the WSO. Apparently, the desiccant was not changed after the maintenance responsibility was transferred to new personnel. This problem manifested itself in the data after May, 1992. Although the IR data appear to be reasonable after that time some caution should be employed when using that data as well.

22

There were other problems with the data during the period covered by this report. Most of these "glitches" are trapped by the data processing software with the result that the data which are available on the "anonymous" ftp should be as error free as it can be without corroborating measurements. Regarding the large periods of loss of data it is noted that the remoteness of the installations made travel expensive and trips could only be made infrequently. The first maintenance trip was not undertaken until October, 1992. Also, the personnel at the sites had limited technical skills and were reluctant to attempt maintenance procedures. Finally, it is noted that the assistance of the WSO personnel was of a voluntary nature and at times their schedules did not allow immediate attention to the problems with the SRBs.

5.0 Acknowledgements

6.0 References

Albrecht, B., and S. K. Cox, 1977: Procedures for improving pyrgeometer performance. *J. Appl. Meteor.,* **16,** 188-197.

Foot, J.S. 1986: A new pyrgeometer. *J. Atmos. and Ocean. Tech.,***3,** 363-370.

Webster P. J., 1988: The role of hydrological processes in ocean-atmosphere interaction. In Proc. of the U.S. TOGA Western Pacific Air-sea Interaction Workshop, R. Lukas and P. Webster, eds., USTOGA 8, U. Corp. Atmos. Res., 71-100.

APPENDIX A

A1.0 Radiometers

This Appendix contains details of the electrical and radiative characteristics of the instrumentation deployed at the SRB sites.

A1.1 Pyrgeometer

A1.11 Instrument Description

The Eppley Precision Infrared Pyrgeometer measures irradiance in the 4-100μm spectral region of terrestrial radiation. It uses a blackened multi-junction thermopile to create a voltage which ideally is linearly related to the net gain in radiant power. The thermopile is coated with Parsons black lacquer and emits like a black body at a temperature T. A thermistor is used to measure the sink temperature of the thermopile.

This pyrgeometer achieves its aim by isolating the desired spectral region by means of an interference filter vacuum deposited on the inside of a silicon dome.

A1.12 Specifications

Sensitivity	-	5 μV/Watt/m^2
Impedance	-	700 ohms
Temperature Dependence	-	± 2% (-20° C to 40° C)
Linearity	-	± 1% (0 to 700 watts/m^2
Response Time	-	2 seconds
Cosine Response	-	< 5% from normalization (Insignificant for a diffuse source)

The orientation of the instrument has no effect on performance, but the accuracy of the instrument is very dependent on calibration which requires special care due to the dome-sink temperature differences.

24

A1.13 Data Reduction

Using the reduction equations from Albrecht and Cox, 1976, the incident radiance, L, upon the pyrgeometer is given by the following equation.

$$L = K_1 E + \sigma \epsilon_o T_s^4 - K_2 \, \sigma(T_d^4 - T_s^4)$$

T_s	-	sink temperature
T_d	-	dome temperature
L	-	incident radiation
E	-	voltage

The constants K_1 and K_2 for the stations are given below.

June '91 to October '92

Majuro:	$K_1 = -221.4$	$K_2 = 0.020$
Pohnpei:	$K_1 = -213.4$	$K_2 = 0.0042$
Chuuk:	$K_1 = -228.8$	$K_2 = 0.064$

October '92 to present

Majuro:	$K_1 = -243.36$	$K_2 = 3.40$
Pohnpei:	$K_1 = -213.4$	$K_2 = 0.0042$
Chuuk:	$K_1 = -241.78$	$K_2 = 3.96$

December '92 to present

Darwin:	$K_1 = -233.1$	$K_2 = 0.70$
Kavieng:	$K_1 = -264.6$	$K_2 = -1.15$

A1.2 Pyranometer

A1.21 Instrument Description

The Eppley Precision Spectral Pyranometer (PSP) measures shortwave radiation including the direct component of sunlight, the diffuse component, and reflection from natural surfaces.

It uses a multi-junction thermopile blackened with Parsons black lacquer and temperature compensated to give a response independent of ambient temperature.

The pyranometers used have a pair of concentric hemispheres of precision ground and polished Schott optical glass. Both hemispheres are made of WG7 clear glass transparent from .28 to 2.8 μm.

The accuracy of the PSP is typically 1%. It should be noted, calibrations could have a diurnal and annual cycle and may change with temperature.

A1.22 Specifications

Sensitivity	~	9 μV/watt/m²
Impedance	~	650 ohms
Temperature Dependence	~	± 1% over ambient temperature (20°C to 40°C)
Linearity	~	± .5% (0 to 2800 watt/m²)
Response Time	~	1 second
Cosine Response	~	± 1 % from normalization (0 to 70° zenith)
		± 3 % from normalization (70° to 80° zenith)

A1.23 Data Reduction

The instruments used in this experiment were compared with secondary standards to establish calibration coefficients relating the voltage output of the instruments to the irradiance. The following calibration coefficients were obtained and compared with pyranometer calibrations from NOAA CMDL:

Slope

$H(w/m^2) = aV + b \qquad a(w\ m^{-2}\ mv^{-1}) \qquad$ b is negligible

where V is the measured voltage output expressed in mV.

June '91 to October '92

Majuro: 117.924
Pohnpei: 103.306
Chuuk: 99.128

October '92 to present

Majuro:	118.755
Pohnpei:	100.010
Chuuk:	115.902

December '92 to present

Darwin:	100.705
Kavieng:	113.973

A2.0 Supporting Instrumentation

A2.1 Wind Speed Sensor

A2.11 Instrument Description

The Met-One 014A Wind Speed Sensor is a 3-cup anemometer which uses a magnet-activated reed switch to create a frequency output signal proportional to wind speed.

A2.12 Specifications

Threshold	-	0.45 m/s
Calibrated Range	-	0 - 45 m/s
Accuracy	-	1.5% or .11 m/s
Temperature Range	-	-50 to +70°C
Distance Constant	-	< 4.6 meters
Output Signal	-	Contact Closure, Reed Switch

A2.2 Air Temperature Sensor

A2.21 Instrument Description

On the Handar data stations (Majuro, Pohnpei and Chuuk), air temperature is measured using a Handar 432A Temperature Sensor. This is essentially a precision thermistor device, surrounded by a model 442B Solar Radiation Shield. The resistance of the thermistor is measured in a voltage-divider circuit, and the result is linearized by a table lookup routine in the datalogger.

The Campbell stations (Darwin, Kavieng) use a Campbell model 107 Temperature Probe, mounted in a model 41301 6-plate Gill Radiation Shield. The 107 also contains a precision thermistor, which is measured using a voltage-divider circuit. The result is converted to a temperature using a polynomial curve fit within the datalogger.

A2.22 Specifications

Handar 432A:

Type	-	Single Thermistor
Conversion Table Range	-	-50°C to +50°C
Accuracy	-	±0.2°C, -20° to +80°C
Input power	-	10-15VDC; 2.5mA (nom) @12.5V

Campbell 107:

Type	-	Single Thermistor
Linearization Error	-	<0.1°C, -33 to 48°C
Overall Accuracy	-	±0.2°C, -33 to 48°C

28

APPENDIX B

This appendix presents a graphical summary of the data collected at the three SRB sites from June, 1991 through September, 1992. The major data discrepancies have been retained in the plots so the reader may identify these periods. The solar data are presented in terms of a solar transmittance, which represents the fraction of the extraterrestrial solar irradiance on a horizontal surface that was transmitted through the atmosphere and measured at the surface by the pyranometer. The infrared irradiance was converted to an infrared "emittance", calculated as the fraction of the Stefan-Boltzmann irradiance that would be emitted by a blackbody radiating at the SRB measured surface temperature.

HOURLY AVERAGES FOR MAJURO, JUN 91

HOURLY AVERAGES FOR MAJURO, JUL 91

HOURLY AVERAGES FOR MAJURO, AUG 91

HOURLY AVERAGES FOR MAJURO, SEP 91
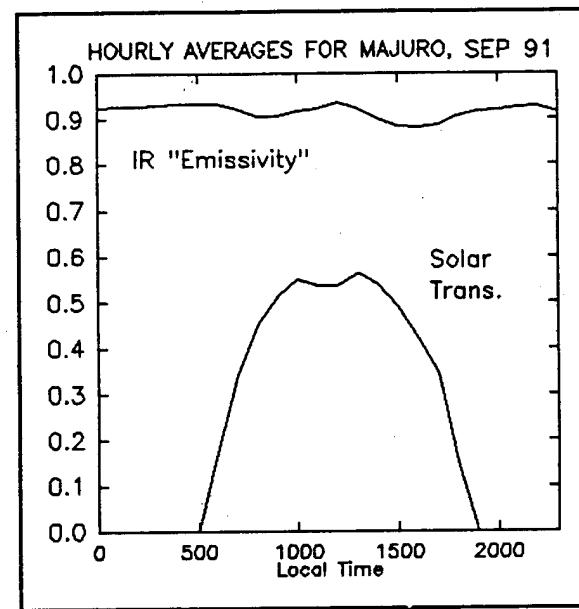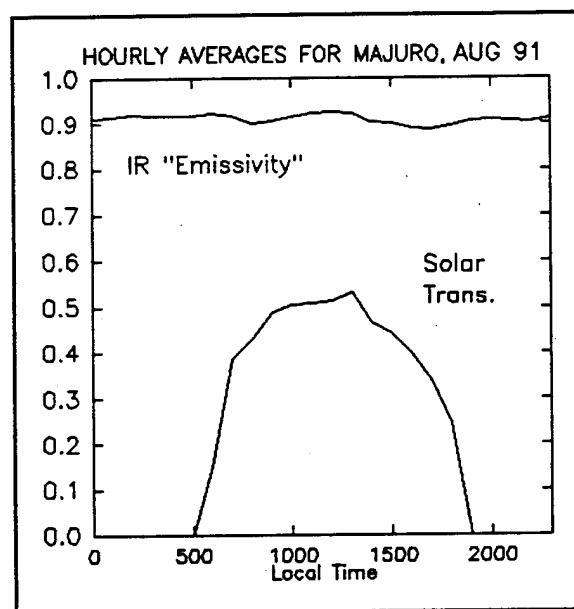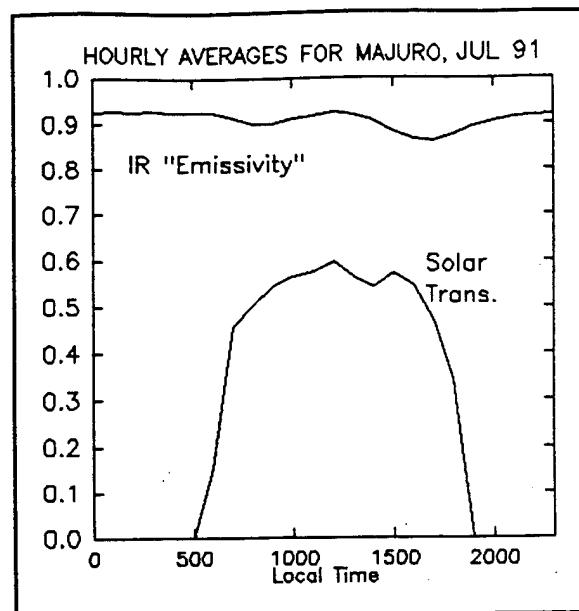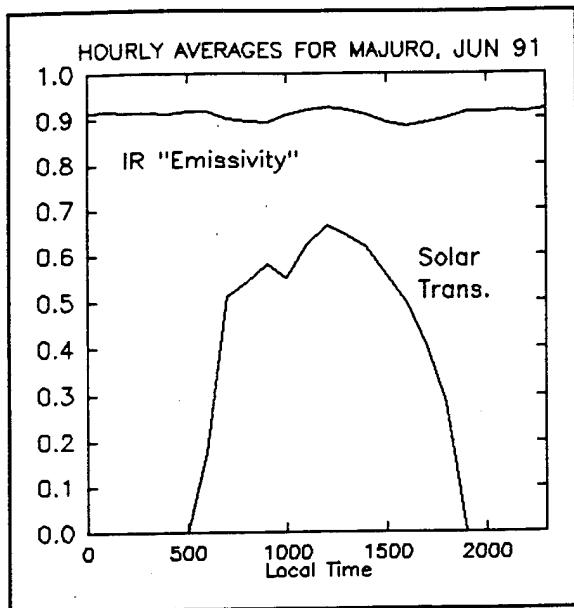
Figures B1 through B4 show the solar transmittances and infrared "emittances" measured at Majuro during the period June - September, 1991.

HOURLY AVERAGES FOR MAJURO, OCT 91

HOURLY AVERAGES FOR MAJURO, NOV 91

HOURLY AVERAGES FOR MAJURO, DEC 91

HOURLY AVERAGES FOR MAJURO, JAN 92
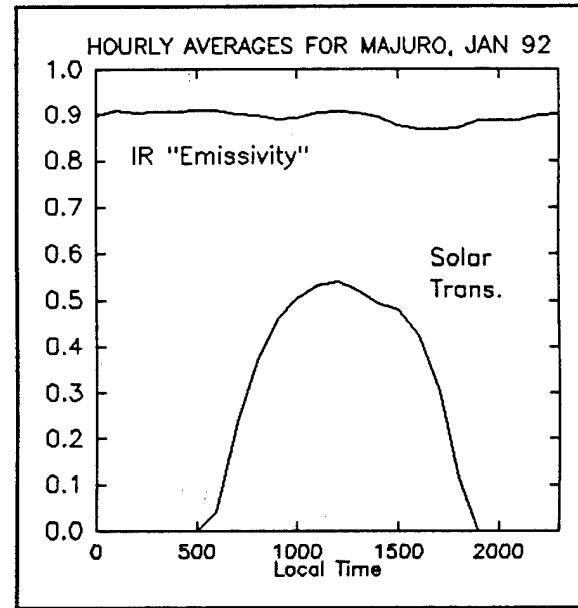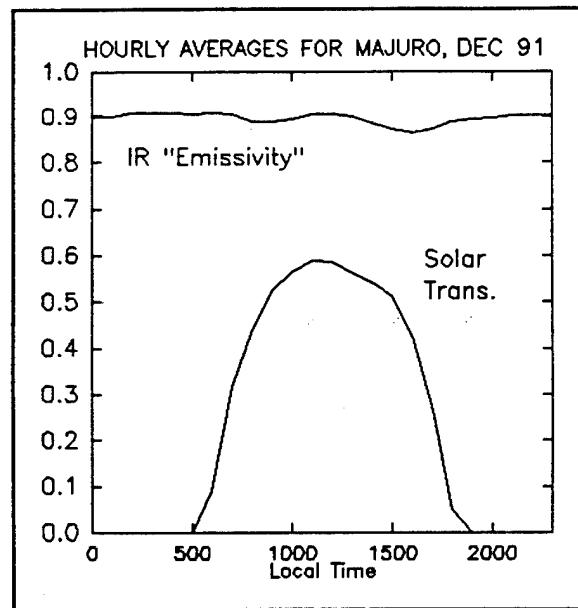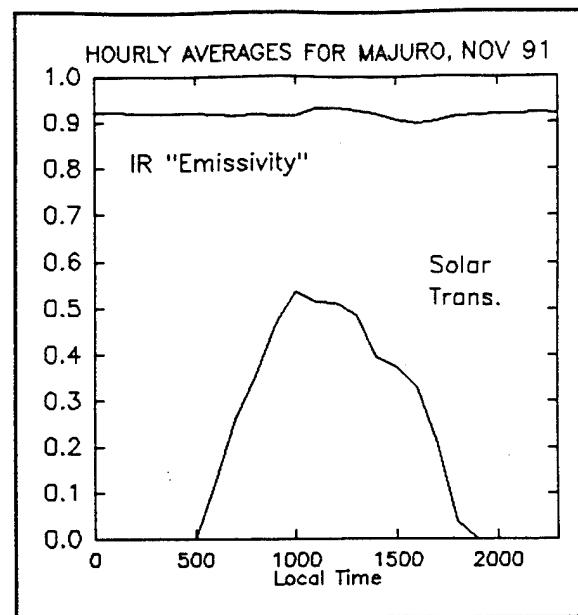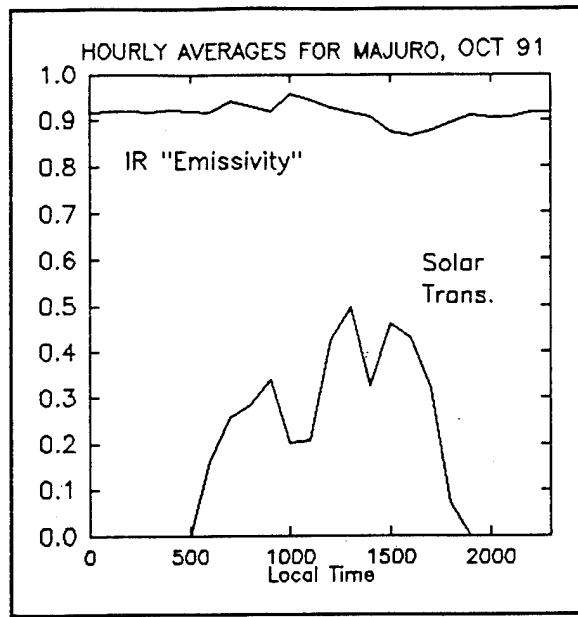
Figures B5 through B8 show the solar transmittances and infrared "emittances" measured at Majuro during the period October, 1991 - January, 1992.

HOURLY AVERAGES FOR MAJURO, FEB 92

IR "Emissivity"

Solar Trans.

Local Time

HOURLY AVERAGES FOR MAJURO, MAR 92

IR "Emissivity"

Solar Trans.

Local Time

HOURLY AVERAGES FOR MAJURO, APR 92

IR "Emissivity"

Solar Trans.

Local Time

HOURLY AVERAGES FOR MAJURO, MAY 92

IR "Emissivity"

Solar Trans.

Local Time
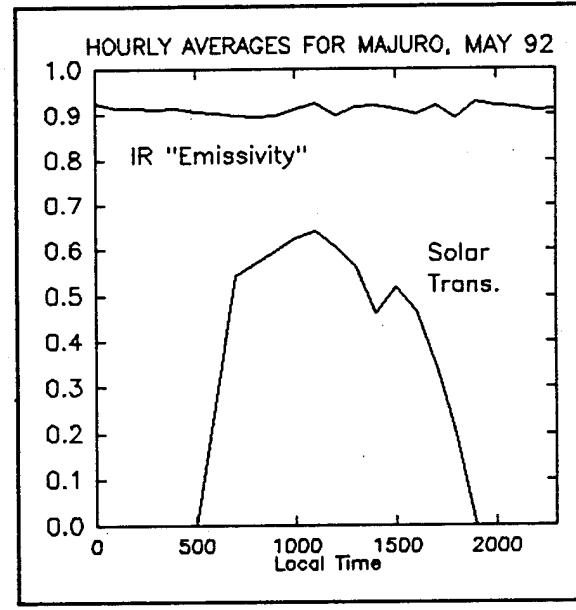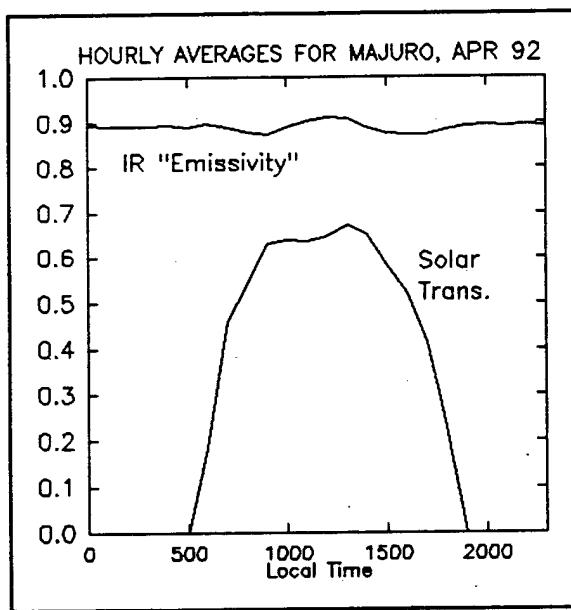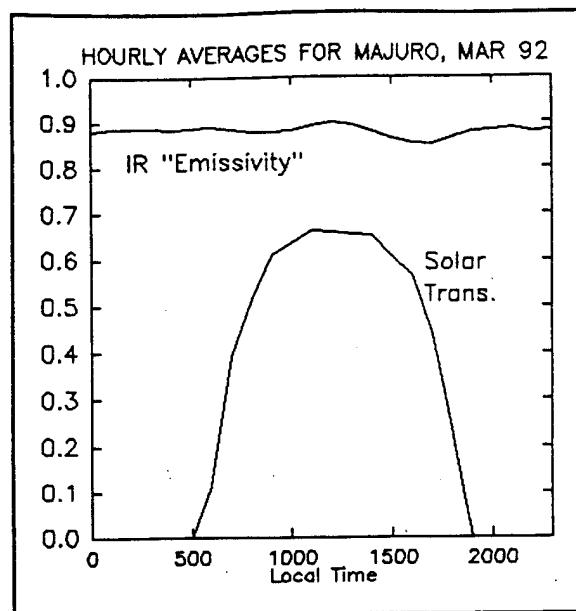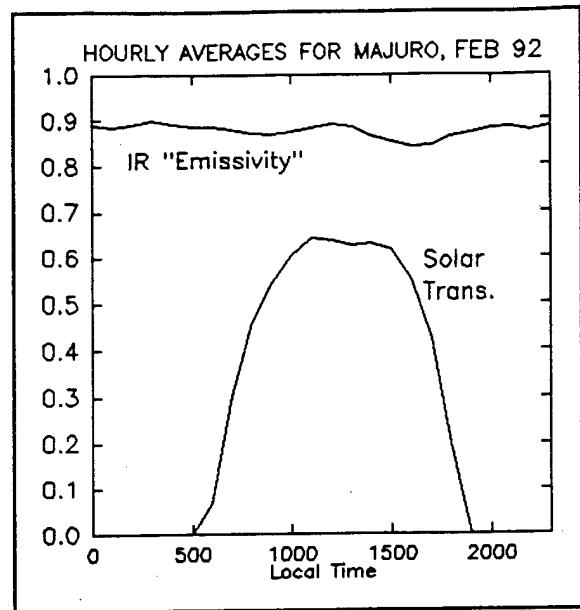
Figures B9 through B12 show the solar transmittances and infrared "emittances" measured at Majuro during the period February - May, 1992.

HOURLY AVERAGES FOR MAJURO, JUN 92

HOURLY AVERAGES FOR MAJURO, JUL 92

HOURLY AVERAGES FOR MAJURO, AUG 92

HOURLY AVERAGES FOR MAJURO, SEP 92
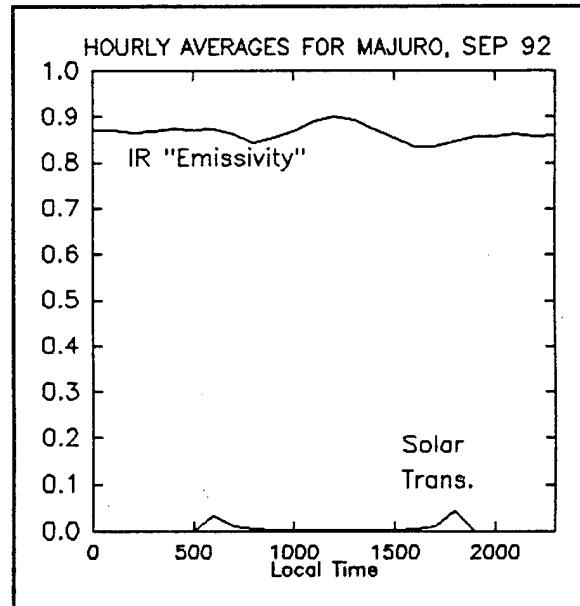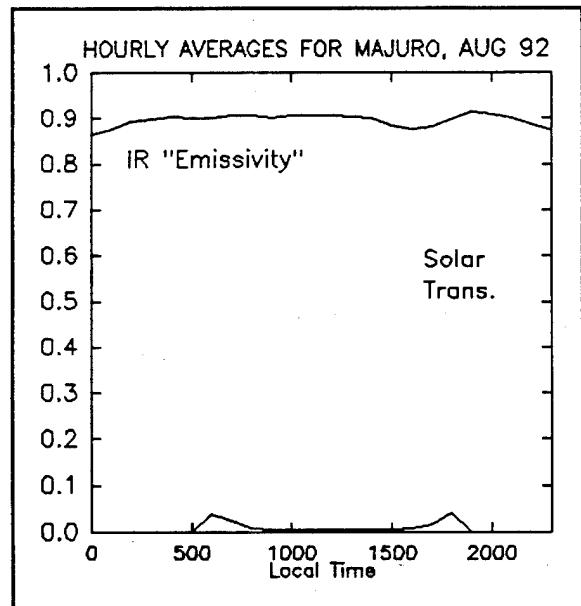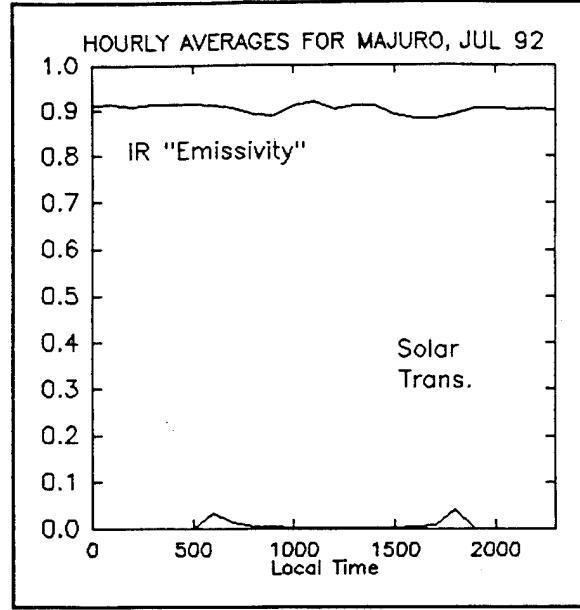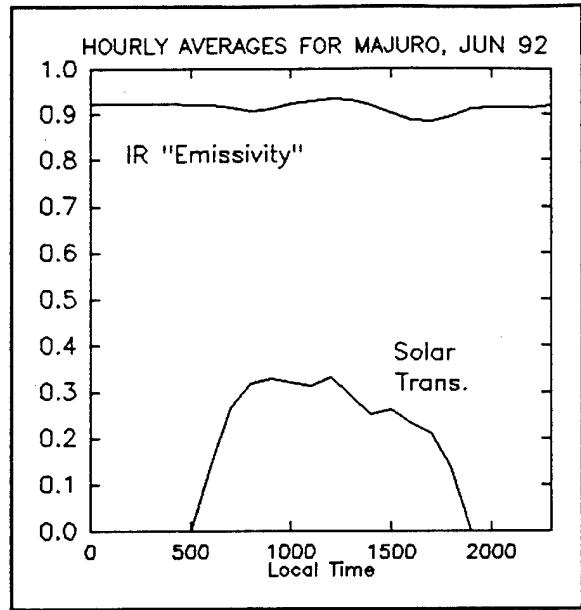
Figures B13 through B16 show the solar transmittances and infrared "emittances" measured at Majuro during the period June - September, 1992.

HOURLY AVERAGES FOR POHNPEI JUN 91

IR "Emissivity"

Solar Trans.

HOURLY AVERAGES FOR POHNPEI, JUL 91

IR "Emissivity"

Solar Trans.

HOURLY AVERAGES FOR POHNPEI, AUG 91

IR "Emissivity"

Solar Trans.

HOURLY AVERAGES FOR POHNPEI, SEP 91

IR "Emissivity"
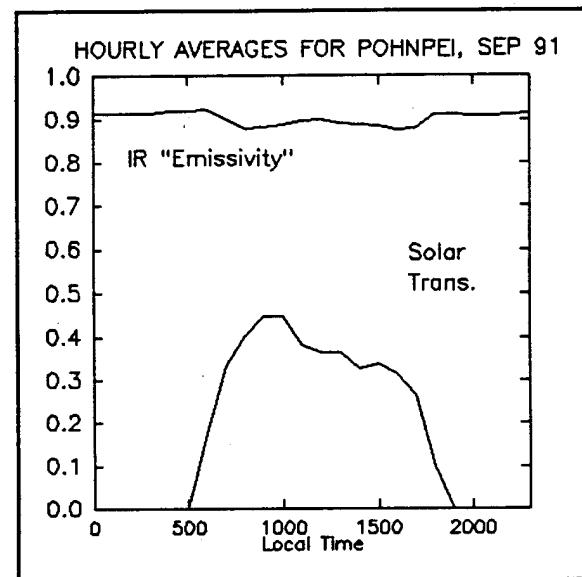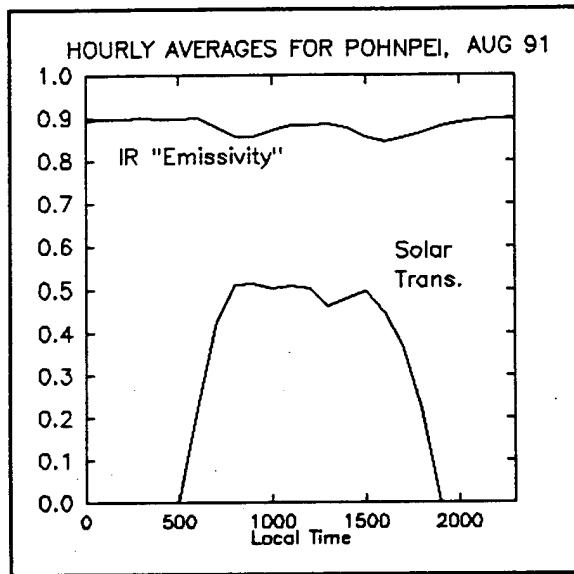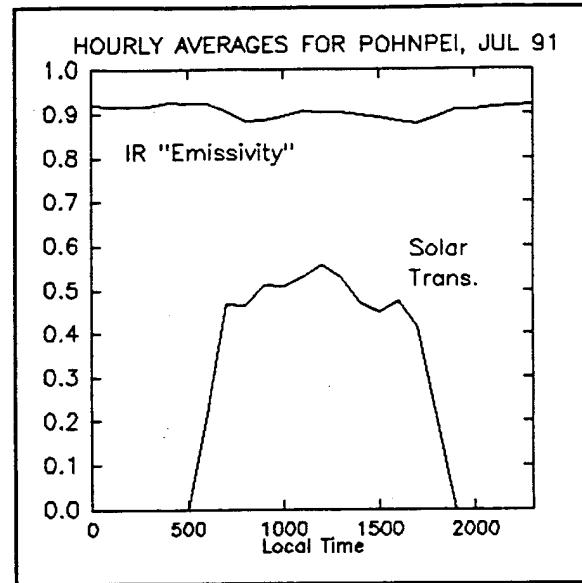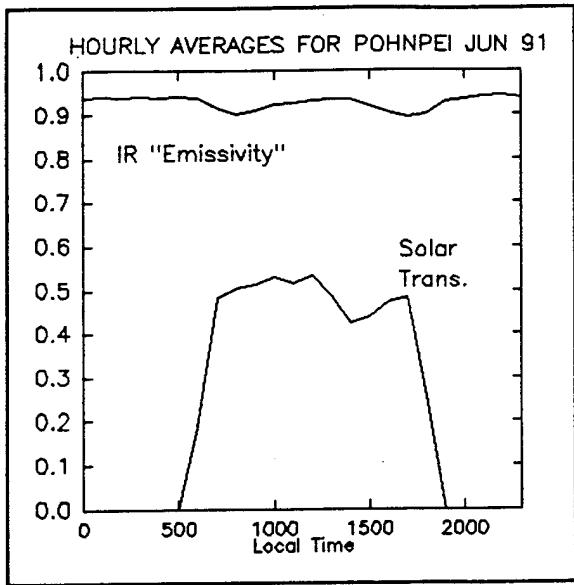
Solar Trans.

Figures B17 through B20 show the solar transmittances and infrared "emittances" measured at Pohnpei during the period June - September, 1991.

34

HOURLY AVERAGES FOR POHNPEI, OCT 91

HOURLY AVERAGES FOR POHNPEI, NOV 91

HOURLY AVERAGES FOR POHNPEI, DEC 91

HOURLY AVERAGES FOR POHNPEI, JAN 92
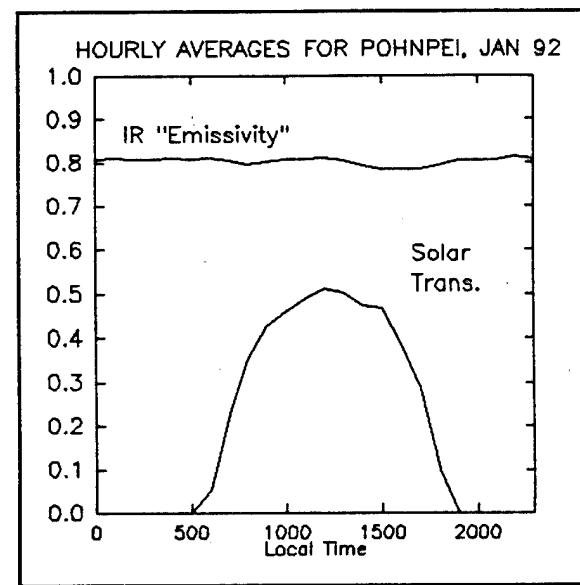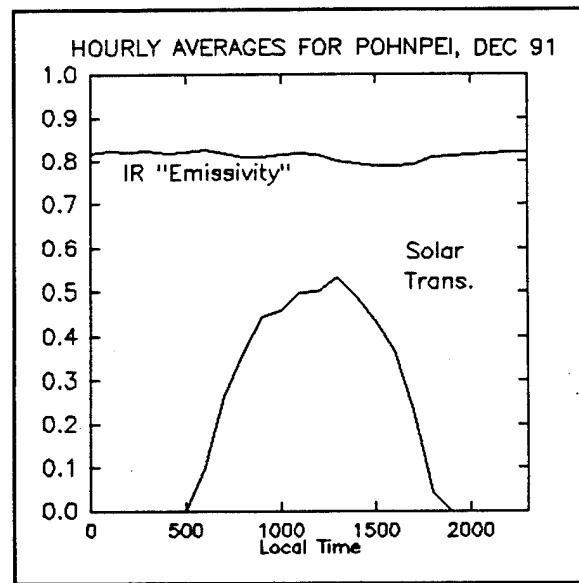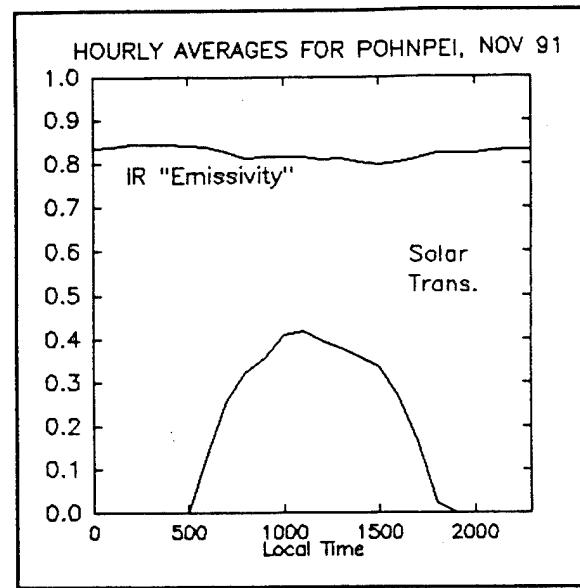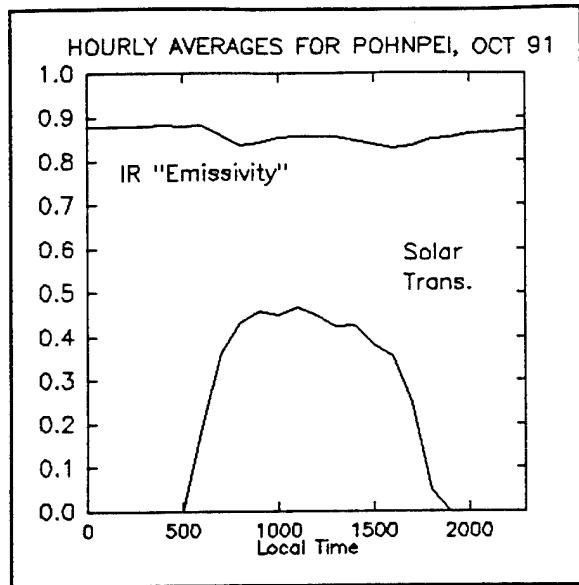
Figures B21 through B24 show the solar transmittances and infrared "emittances" measured at Pohnpei during the period October, 1991 - January, 1992.

35

HOURLY AVERAGES FOR POHNPEI, FEB 92

IR "Emissivity"

Solar Trans.

Local Time

HOURLY AVERAGES FOR POHNPEI, MAR 92

IR "Emissivity"

Solar Trans.

Local Time

HOURLY AVERAGES FOR POHNPEI, APR 92

IR "Emissivity"

Solar Trans.

Local Time

HOURLY AVERAGES FOR POHNPEI, MAY 92

IR "Emissivity"

Solar Trans.

Local Time
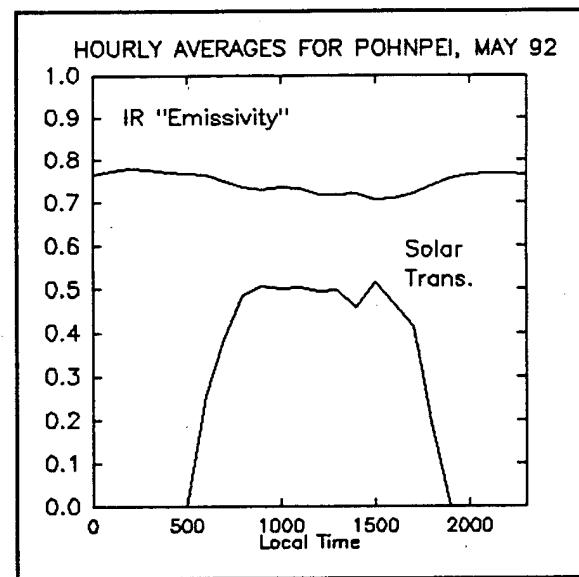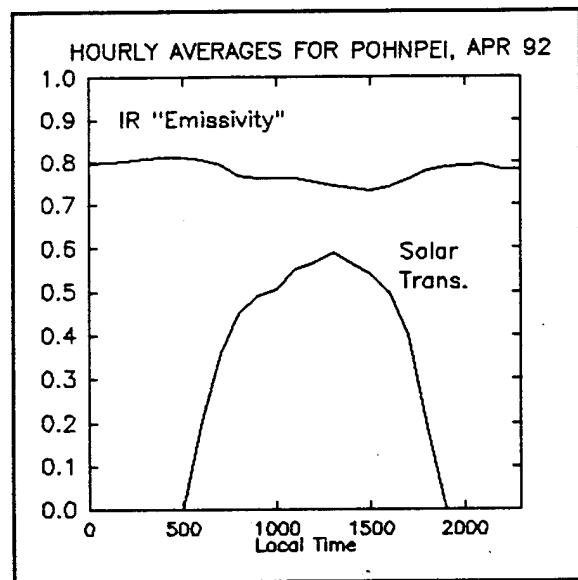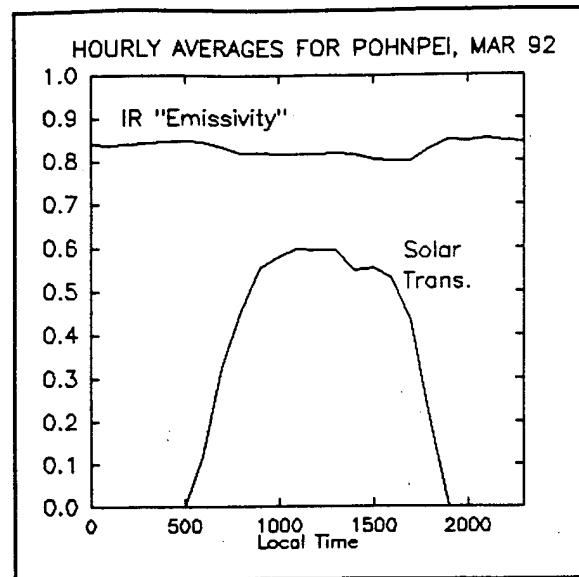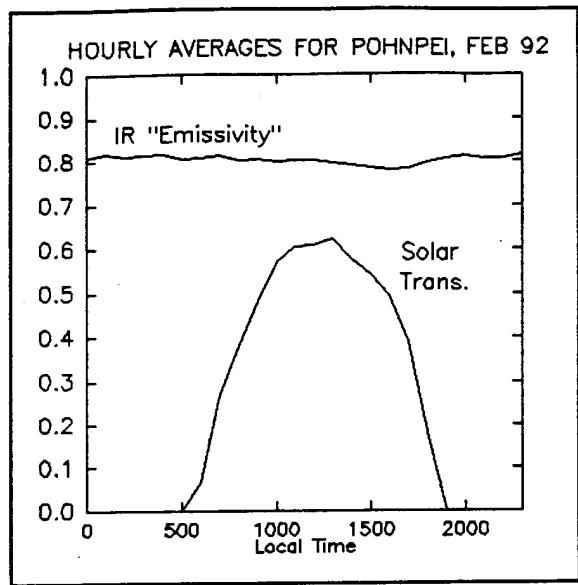
Figures B25 through B28 show the solar transmittances and infrared "emittances" measured at Pohnpei during the period February - May, 1992.

HOURLY AVERAGES FOR POHNPEI, JUN 92

IR "Emissivity"

Solar
Trans.

Local Time

HOURLY AVERAGES FOR POHNPEI, JUL 92

IR "Emissivity"

Solar
Trans.

Local Time

HOURLY AVERAGES FOR POHNPEI, AUG 92

IR "Emissivity"

Solar
Trans.

Local Time

HOURLY AVERAGES FOR POHNPEI, SEP 92

IR "Emissivity"

Solar
Trans.

Local Time
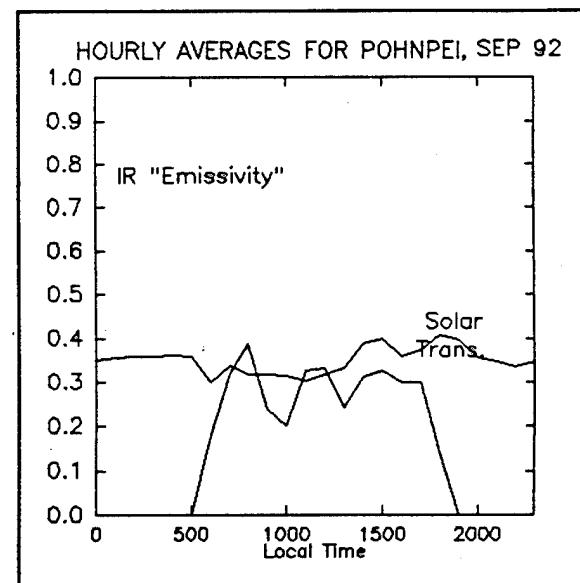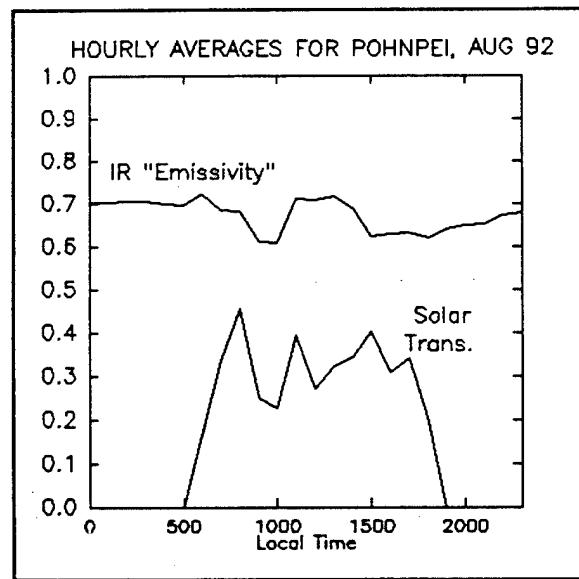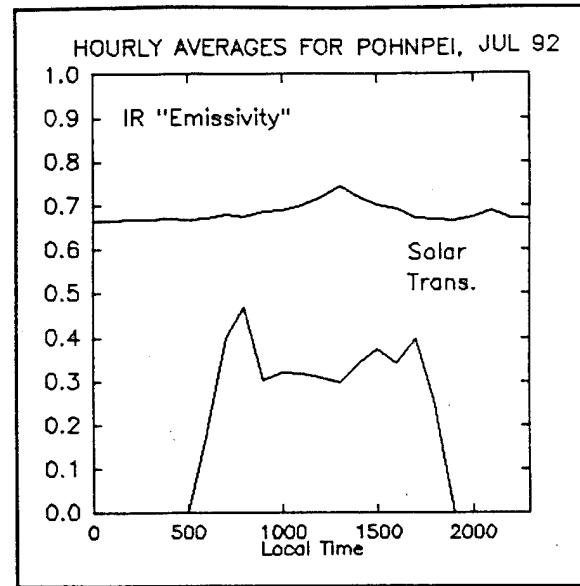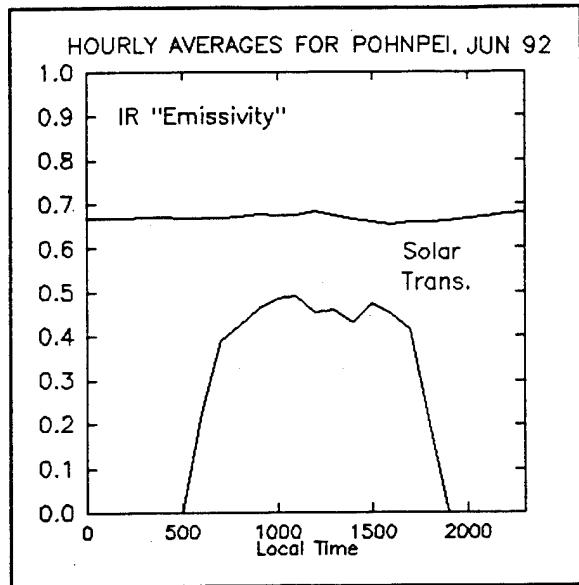
Figures B29 through B32 show the solar transmittances and infrared "emittances" measured at Pohnpei during the period June - September, 1992.
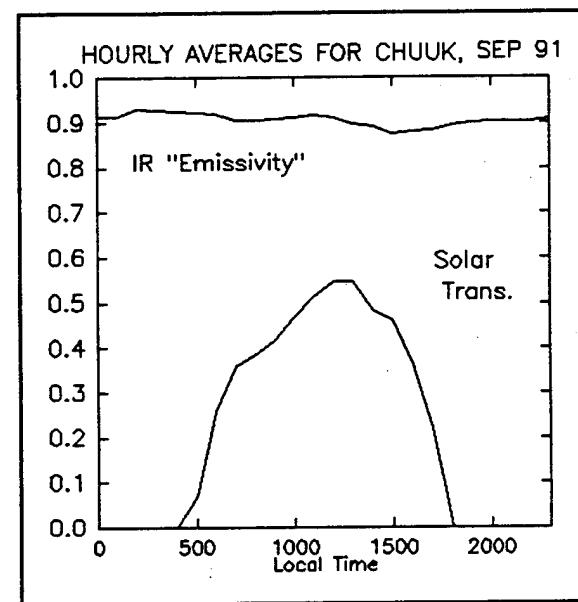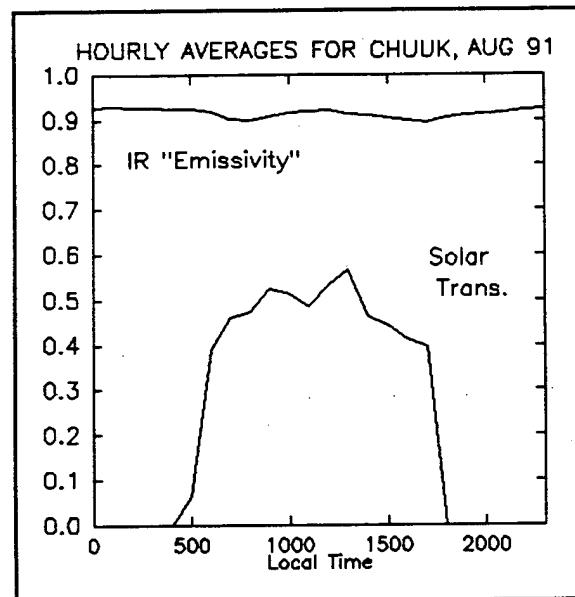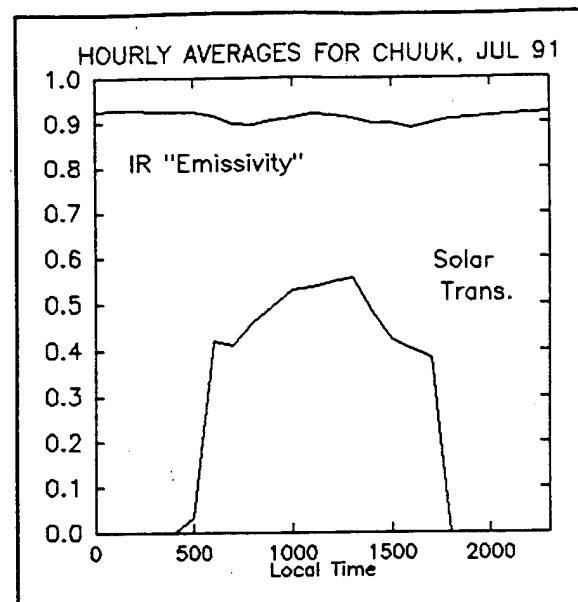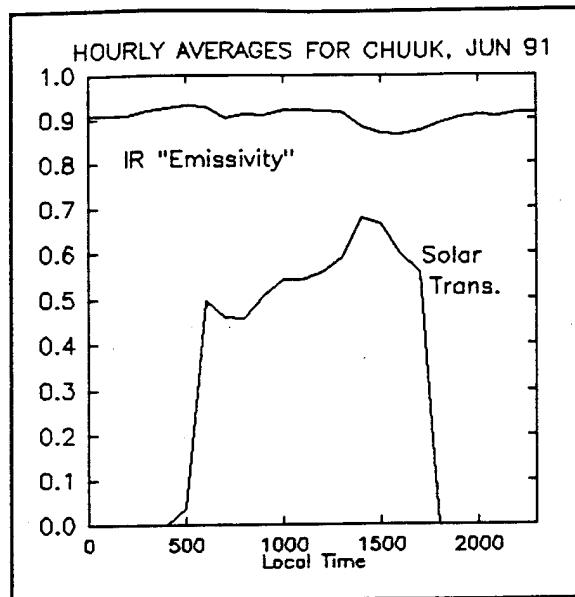
Figures B33 through B36 show the solar transmittances and infrared "emittances" measured at Chuuk during the period June - September, 1991.

HOURLY AVERAGES FOR CHUUK, OCT 91

IR "Emissivity"

Solar Trans.

HOURLY AVERAGES FOR CHUUK, NOV 91

IR "Emissivity"

Solar Trans.

HOURLY AVERAGES FOR CHUUK, DEC 91

IR "Emissivity"

Solar Trans.

HOURLY AVERAGES FOR CHUUK, JAN 92

IR "Emissivity"
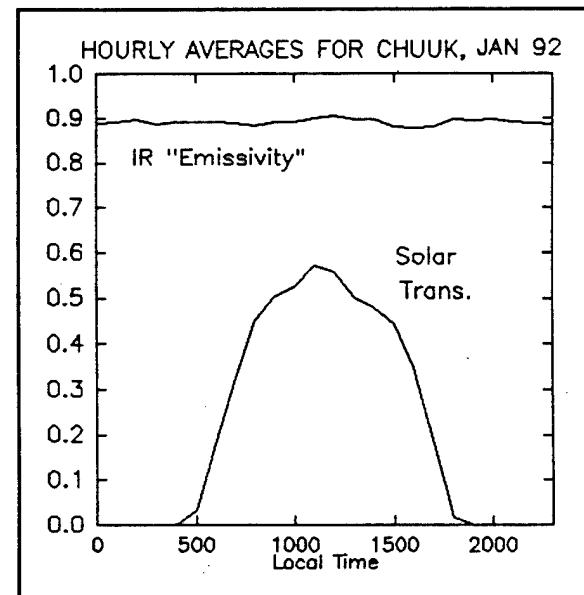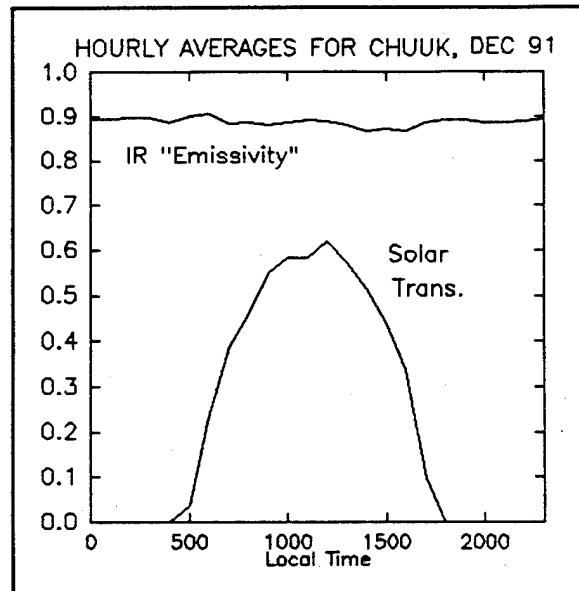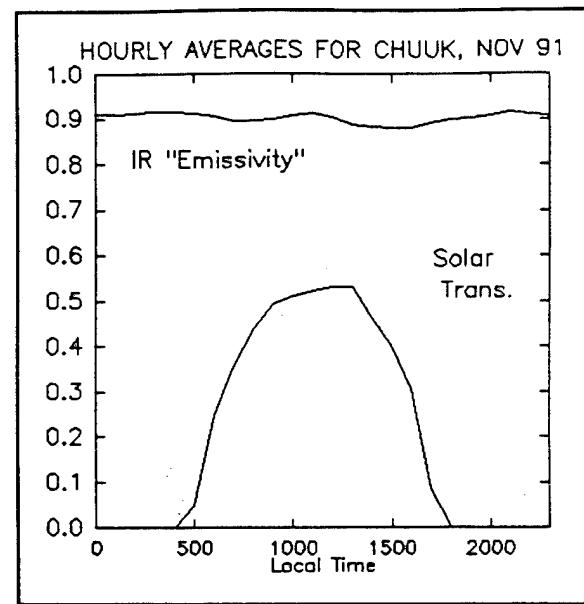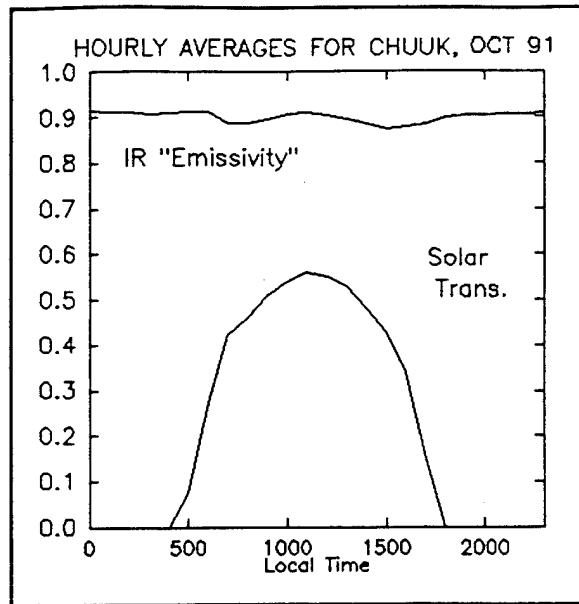
Solar Trans.

Figures B37 through B40 show the solar transmittances and infrared "emittances" measured at Chuuk during the period October, 1991 - January, 1992.
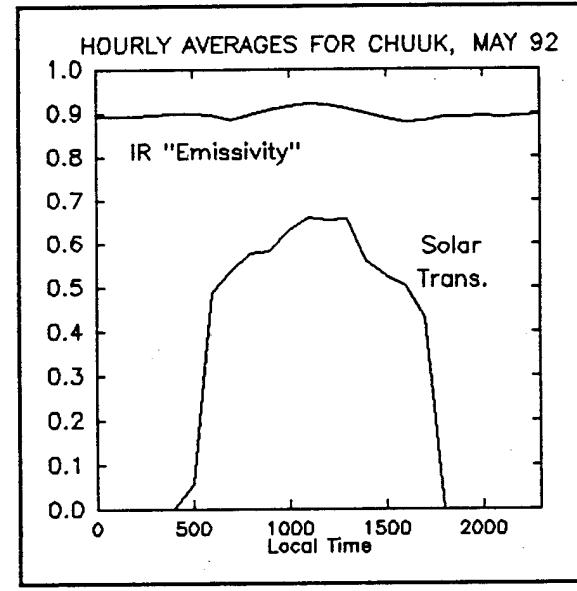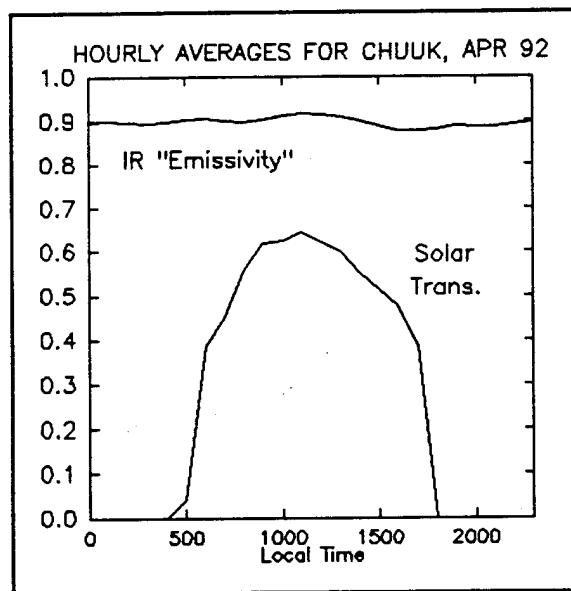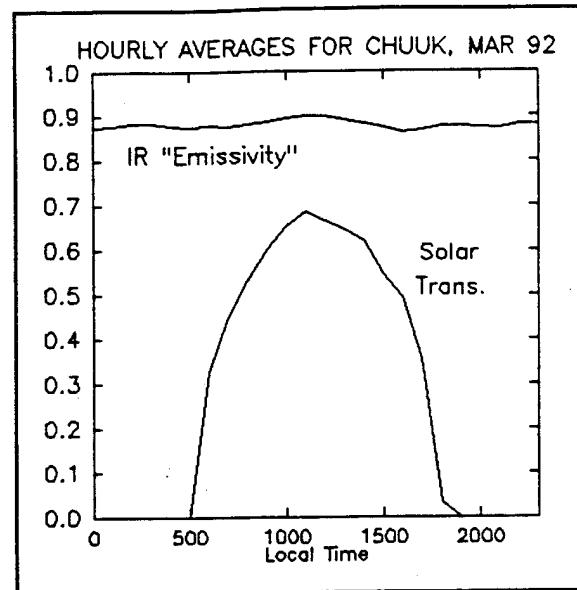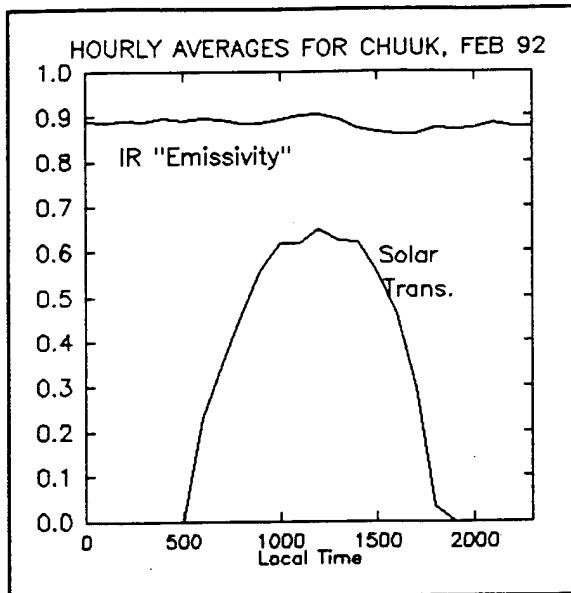
Figures B41 through B44 show the solar transmittances and infrared "emittances" measured at Chuuk during the period February - May, 1992.
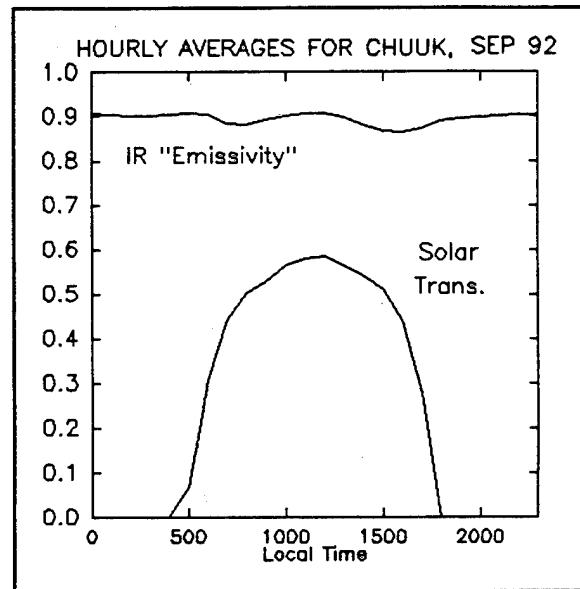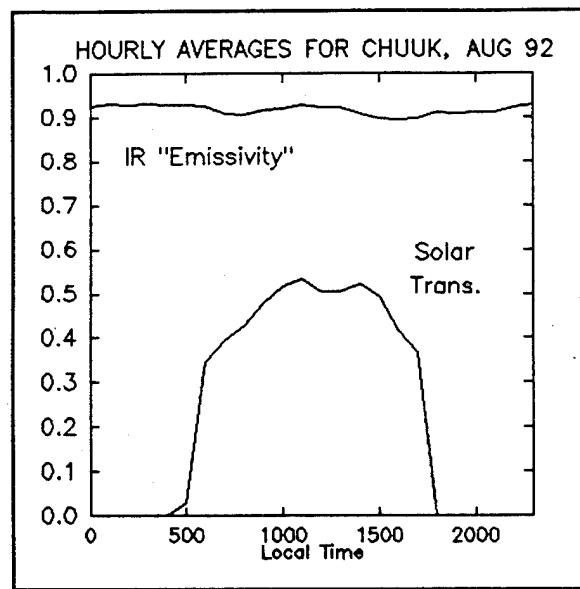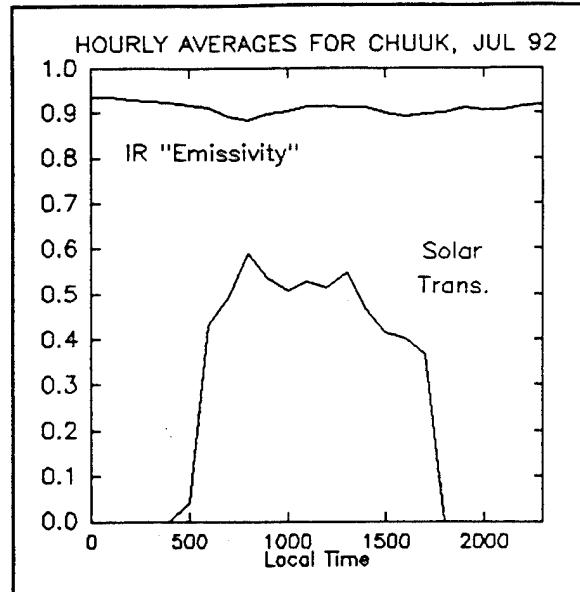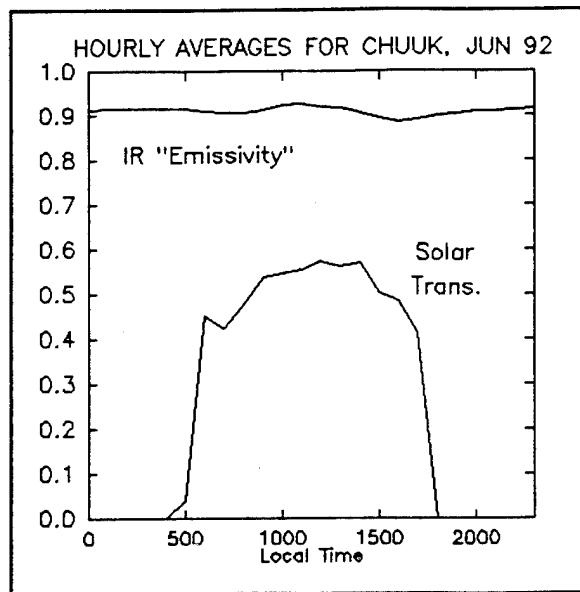
Figures B45 through B48 show the solar transmittances and infrared "emittances" measured at Chuuk during the period June - September, 1992.

41

APPENDIX C

Maintenance Manual for the TOGA COARE
Surface Radiation Station

by

John M. Davis

and

Chris Cornwall

Department of Atmospheric Science
Colorado State University
Fort Collins, CO 80523
Phone
303-491-8693
or
303-491-8583

November 1992

Table of Contents

1.0 Introduction

The surface radiation budget station which has been deployed at your site is one component of the Tropical Oceans Global Atmosphere (TOGA) Coupled Oceanic Atmospheric Research Experiment (COARE). The purpose of the project, which is funded by NOAA, is to carefully measure the amount of solar and infrared radiation reaching the earth's surface in a region which has been identified as probably the most convectively active of any on the planet. Estimates of the surface heat budget in this part of the world are somewhat questionable, and measurement of the radiative exchange is one part of a more accurate assessment of this budget.

This station has been designed to provide accurate data and operate in a reliable fashion with minimal maintenance. Some minor daily attention will be required to insure the quality of the data, and routine (bimonthly) calibration checks will be needed as well. Just as with any electronic system, totally trouble free service can not be guaranteed; thus, this manual is being provided as a simple guide to the basic components of the system. Its purpose is to familiarize the reader with the system to the extent that simple maintenance might be possible by National Weather Service personnel if the situation warrants and only according to direction from the Department of Atmospheric Science at Colorado State University.

This manual is organized on a priority basis; i.e., the most needed information is discussed first and information least likely to be needed is included later. We hope this manual will be easy to follow and that personnel at the sites will refer to it and follow its guidance in order to assure the success of the project.

2.0 Basic description of the station

The data of interest provided by the station are the solar hemispheric downwelling radiation, the ultraviolet hemispheric downwelling radiation, and the infrared hemispheric downwelling radiation from the atmosphere. The first measurement is provided by an Eppley pyranometer (clear dome instrument), the second by an Eppley UV Radiometer, and the last measurement is provided by an Eppley pyrgeometer (silver dome instrument). These instruments are mounted on a horizontal plate at the top of the tripod system. Fig. 1 shows the location of the pyranometer and pyrgeometer on the system. The UV radiometers are not shown in Fig. 1, but are located between the pyranometer and the pyrgeometer. All other instrumentation deployed on the system is designed to aid in interpretation of the primary data streams. The other instrumentation included with the system includes: an anemometer, an ambient air temperature sensor, a Handar model 540 data collection system which includes a GOES satellite transmitting station and a Handar WWV receiver which merely assures proper operation of the internal clock of the data collection system. The small antenna is part of the GOES transmitting station and the copper length of wire is a receiving antenna for the WWV (clock) receiver. The entire system is mounted on a sturdy tripod support. A Toshiba 1000 SE laptop computer has also been supplied which serves as a communication device to the 540 data collection system. Its purpose is to allow simple reprogramming of the station, should that become necessary, and to provide a means of data retrieval if transmittal of the data via the GOES satellite fails. Each of these devices will be discussed in the following paragraphs.
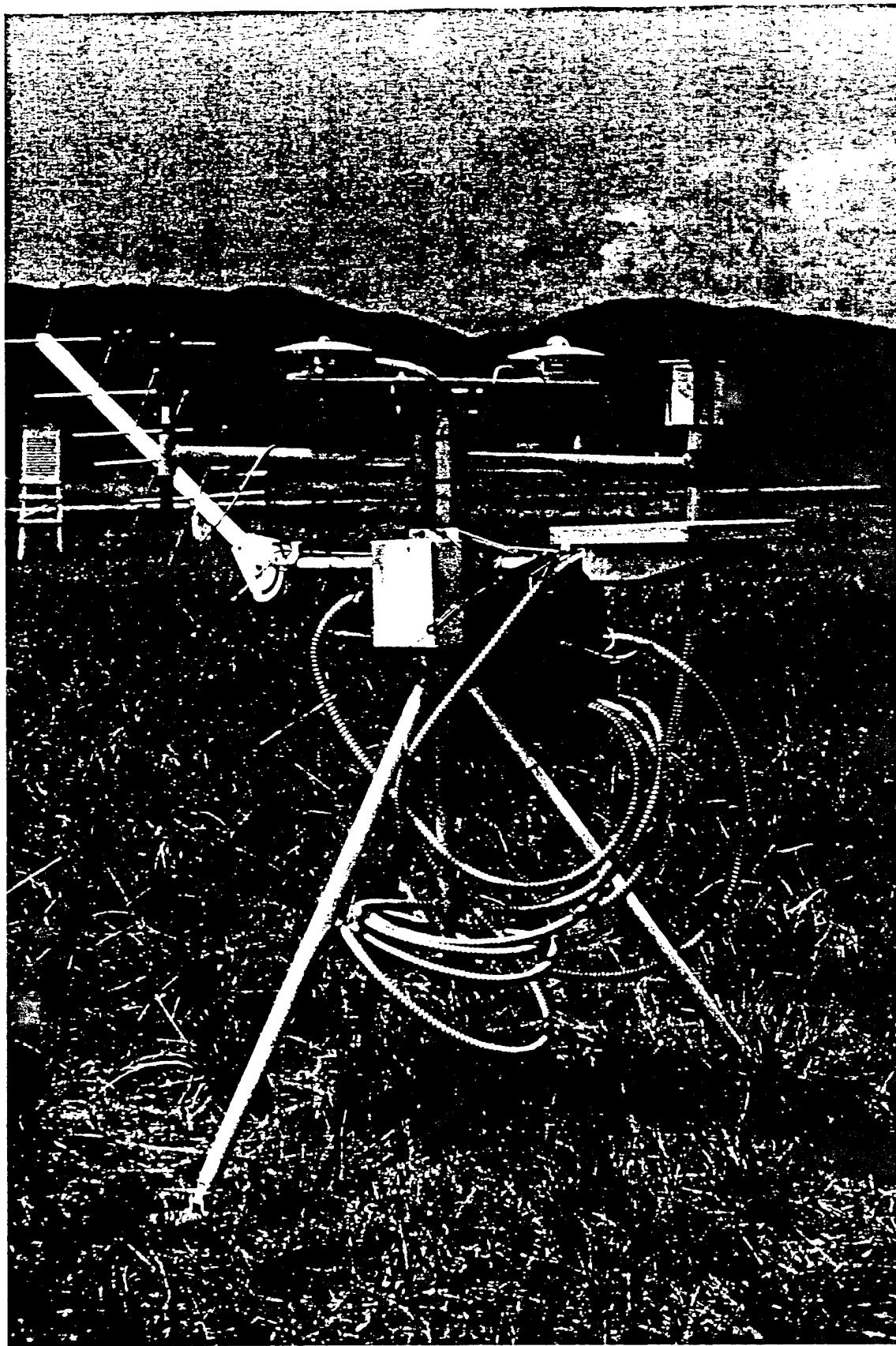
Figure 1. Photo of an SRB station during testing phase at Colorado State University.

2.1 Eppley radiometers.

The Eppley pyranometer measures the amount of hemispheric solar radiation, which includes the visible portion of the solar spectrum. The Eppley pyrgeometer measures the amount of hemispheric downwelling infrared radiation in the 2.8 - 40.0 micrometer region of the spectrum. The Eppley UV radiometer measures the amount of downwelling ultraviolet radiation. These instruments are rugged and will provide reliable data provided a simple maintenance routine is followed. Below all three instruments will be referred to as radiometers.

There are three basic maintenance procedures which need to be carried out in order to assure good data. First, on a daily basis, the filter domes (clear or silver) of the instruments must be cleaned. This can be accomplished by wiping the dome with a clean lint free cloth. A supply of lint free pads has been included with the station. The dome must be wiped daily. The best time to do this is after a precipitation event, since a wet dome also invalidates the data.

Second, approximately once a week, the level of the instruments should be checked. Each radiometer is equipped with a small bubble level mounted on the base plate of the instrument. The bubble must be within the small circle in the center of the level. The level may be adjusted by means of three black-knobbed bolts on each radiometer. Normally this will be necessary only after a severe wind storm, but a small adjustment may be necessary after time due to slight settling of the tripod system.

Third, the condition of the desiccant must be monitored. Each radiometer is equipped with a small desiccant container which mounts into the cylindrical side of the instruments. The desiccant within the containers may be inspected by viewing it through the clear glass windows. The desiccant should appear bluish in color. If it is pink or white it should be replaced. A container of silica gel crystals and extra empty desiccant containers are supplied for this purpose. If it becomes necessary to replace the internal desiccant, the extra container should be filled with silica gel indoors then carried to the station. Each extra container has an "O" ring seal around the inside of he knurled knob housing. This "O" ring should be coated with a small amount of the moisture displacement (Dow-Corning sealant/lubricant) compound which is supplied in a small tube. Remove the "O" ring using a small screwdriver included with the tool kit and coat the "O" ring with the lubricant then replace it on the container. Fill the container as much as possible with fresh silica gel desiccant and replace the lid to the silica gel bottle. While protecting the container as much as possible carry it to the station. Unscrew the depleted desiccant container from the radiometer making sure to remove the "O" ring with it and replace immediately with the refilled container and newly coated "O" ring. It is important that the amount of time the instrument is exposed without a desiccant container installed be kept to a minimum since exposure to moist tropical air will cause a more rapid depletion of the new desiccant once it is installed. After replacing the desiccant, the level of the instruments must be checked. Discard the contents of the container and store until another replacement of desiccant is required.

The useable lifetime of the desiccant is uncertain in the tropical environment. In an attempt to prolong the life of the desiccant within the radiometers, an external container, mounted on the radiometer base plate has been installed. The appearance of the drierite desiccant which it contains is light blue when active and pinkish when depleted. This container connects to the two radiometers via flexible plastic tubing and through two brass valves. The purpose of the larger supply of desiccant is to provide extra moisture removal from the radiometers. It is hoped that maintaining the larger desiccant supply will reduce or even eliminate the need to replace the silica gel within the instruments. A supply of drierite desiccant is also provided in a large jar. To replace the depleted drierite, first the supply of air into the radiometers through the tubing must be eliminated. Close both valves by turning the knobs in a clockwise direction. It is important to close the valves

before removing the tubing. The tubing may then be slipped off of the desiccant container and it can be unmounted from the radiometer plate by loosening the metal hose clamp. It also must be taken indoors to be refilled. The desiccant is replaced by removing the metal cap and spring and filter pad assembly, replacing the drierite and replacing the filter pad, spring and lid. The container can then be returned to the station and remounted in the metal hose clamps. The plastic tubing must be firmly reattached and only then should the brass valves be reopened. After replacing the external desiccant, the level of both radiometers should be checked.

2.2 The Handar 540-A data collection system.

The Handar 540-A data collection system is housed in the large stainless steel box which is supported on the mid portion of the tripod. The data system functions as a collection unit and also contains a GOES satellite transmitter which is the primary means of data recovery. It is not anticipated that NWS personnel will need to be concerned about the technical details of the system; however, in some cases, reprogramming the system, resetting the clock or retrieving the data from the system may become necessary. If any of these circumstances arise CSU will contact the representative at your location. These procedures are covered in a later section since they all involve use of the laptop computer system. The system was selected based on an outstanding record of reliability. Thus, hopefully, National Weather Service personnel should have few occasions to interact with data system. The only maintenance we originally requested was a visual inspection of the system's exterior, in particular the connector panel should be checked periodically for corrosion around the cable connectors. If it appears that corrosion is becoming a problem, the connectors should be cleaned as thoroughly as possible and recoated using the tube of moisture displacement compound included with the station. We ask that NWS personnel contact the Department of Atmospheric Science at Colorado State University regarding the problem; (phone numbers and an address may be found on the cover page of this document) if corrosion appears to be a serious problem.

Since deploying the stations, we have learned that the Handar boxes need more attention than was originally expected. This includes checking the internal desiccant bags within the stainless steel box every month, and replacing those bags if necessary. Also, each time the box is opened, a fresh layer of sealant/lubricant should be applied to the seal of the door. With this small amount of extra attention, we should be able to avoid further data problems due to water collecting inside the Handar data collection box.

The procedure for checking the state of the desiccant in the data system box is outlined below. There is a humidity indicator mounted atop the battery compartment inside the data system box which indicates whether the desiccant is still effective. The door to the data system may be opened by loosening (but not removing) the four bolts which hold the metal latches against the door. After the bolts are sufficiently loosened the latches can be moved away from the data system freeing the door to open. A quick glance of the humidity indicator will reveal if the desiccant needs to be recharged. This is indicated if the color of the circle is lighter than that of the rectangular swatch on its left. If the desiccant does need replacement, it is located behind the foam pad next to the right wall of the data system, or possibly on the bottom of the data system box, in three separate packages. Extra desiccant packages have been provided and we have attempted to package them so they will retain there drying ability. Before changing the desiccant packages a thin coating of the moisture displacement compound should be applied to the rubber gasket which seals the door against the data system box. Once this is done the three desiccant bags may be replaced and the door quickly closed, the clamps moved back in place and the four bolts tightened. Although we have attempted to package the replacement desiccant to maintain its drying capacity, it is unlikely that this condition will be maintained for an extended period of time. Instructions for recharging the desiccants may be found on the individual packages (basically they must be heated in an oven at 250 F for at least 12 hours). If this is not possible at your location, exchange desiccant packages will be shipped to your site on a periodic basis depending on the experience gained in the field. We are suggesting the condition of the desiccant be checked on a monthly basis.

6

2.3 The WWVH Radio Receiver

The WWVH radio receiver is housed in the small white box located behind the Handar data unit and includes the copper wire antenna which makes the form of a "V" sloping up from the ground. The purpose of the receiver is to ensure correct timing of the clock in the Handar unit. Basically, the unit monitors the 5, 10 and 15 kHz frequencies once daily at a preset time and attempts to acquire the WWVH timing signal. If it is acquired, the Handar 540A's internal clock is reset. Once deployed, if power is not interrupted, the unit should function in a completely automatic mode. If power to the data system is interrupted it will be necessary to reset the Handar 540a clock. Special software is provided to perform this task and this procedure is described in a subsequent section. The primary maintenance procedure is to maintain the desiccant in the receiver unit. The condition of the desiccant is indicated on a card located within the receiver unit. Two bolts hold latches which secure the lid of the receiver. To open the lid the bolts must be loosened (but not removed) and the latches lifted off of the rim of the lid. Open the lid and inspect the desiccant indicating card. If the color of the circular indicator is as dark or darker than that of the rectangular swatch, the desiccant is still active. If not the two plastic wire ties which hold the desiccant to the lid must be cut with wire cutters and the desiccant removed from the pouch. Additional desiccant packets have been included with the station. These are identical to those for the 540A data system. The new packet should be rolled and inserted in the cloth pouch which can then be reattached to the lid using additional plastic wire ties. The lid must then be resecured by repositioning and tightening the two metal clamps. It is not known how often this procedure should be carried out in the tropical environment. We are initially suggesting a monthly inspection of the condition of the desiccant and future experience will dictate the frequency of the process.

2.4 Support tripod and cabling

The support tripod is made of sturdy aluminum. We anticipate this support will provide years of service; however, it should be inspected periodically to ensure that all hardware is still secure. This can be accomplished routinely on visits to the station to wipe the domes of the radiometers. If any of the nuts work loose they should be tightened with the tools supplied with the station. Also, the WWVH receiver's antenna should be free of any vegetation in order to assure optimum performance in updating the Handar 540A's internal clock.

3.0 The Toshiba 1000SE laptop computer

A Toshiba laptop computer has been supplied as an integral part of the system. The computer has various functions which include: programming upload and download to the Handar 540A data system, resetting the WWVH time of the data system's internal clock and data retrieval from the 540A data system. Each of these procedures will be described, but first it is necessary to become somewhat familiar with the computer and its software.

3.1 Features of the Toshiba 1000SE laptop computer.

The Toshiba 1000SE laptop computer is an MS DOS based battery operated portable. It is supplied with 1Mbyte of RAM, a 1.44Mbyte 3.5 inch floppy drive and sufficient ROM to store the operating system and certain utility programs. The upper 560 Kbytes of RAM are used as a RAM disk and the contents of this non removable disk are maintained by the battery system. The contents of the RAM disk will be lost if the backup battery (see below) becomes discharged. The configuration of the computer (including the allocation of the upper 360Kbytes for the RAM disk) and the Handar software are stored on the RAM disk. Thus if the main and backup battery become discharged the RAM disk must be repartitioned and the Handar operating software reinstalled. The RAM disk is designated as disk D:. The DOS (disk operating system) is stored in read only memory (ROM), which is designated as drive C:, and will not be lost if the batteries become

discharged. However, it is not possible to write information to the C: disk. The floppy is used to transfer program and data information to and from the computer. The keyboard of the computer is protected by a clear plastic cover and various keys on the keyboard have been marked for special function control when used with the programming software. These special decals on the keys must be ignored except when using the programming software. When delivered the laptop was initialized in such a way that the support software for the Handar 540A data system is loaded and ready to execute after power up. However, depending on the state of the battery power supply, it may be necessary to reinitialize the computer, reset the real time clock and reload the software which supports the data system. To avoid these procedures we recommend that the computer be stored with the AC power supply connected and continually supplying power to the computer. The AC adaptor plugs into the computer via a jack on the left side of the computer, toward the back.

There are three batteries within the laptop computer. First, the main removable battery pack, which has a shelf life of about 7 days if the computer is not in use or about 2 hours if the computer is on. Second, a backup battery which is recharged from the main removable battery. This battery maintains the memory in the computer (including the RAM disk) for a short time even if the main battery is discharged, but it is not possible to operate the computer from the backup battery alone. Finally, there is a small battery which maintains the real time clock, but it to will become discharged in a short time if the main battery is totally depleted. With this information in mind we now proceed to describe the possible power-up conditions.

3.2 Power up conditions for the Toshiba 1000SE

As mentioned above, the Handar software is stored on the RAM disk and will be maintained in memory as long as the backup battery is still charged. The power switch to the laptop is located on the midway back on the left side of the computer. No disk will be needed to boot the computer since the DOS is stored in non-volatile ROM. To turn the unit on depress the switch and hold in for about 2 seconds then release. The unit is turned off in a similar manner. After a memory check the unit should display the message:

HANDAR 545C PROGRAMMING/DATA COLLECTION SET

D:\>

If this is the case, the Handar software is in memory and it is possible to use the unit for the desired task, program upload, modification or data download. These topics are addressed below. This section is concerned only with proper power up and initialization of the laptop. Even though the computer powers up as just described, the main battery may nevertheless be nearly discharged. This condition is indicated by a blinking red light(only if the AC adaptor is not plugged in). The AC charger should be plugged in and the unit may be operated in this mode. If it is desired to take the unit to the field it should be turned off and charged for about 4 hours before doing so.

If the batteries have been discharged, the unit may not respond at all, in which case it is necessary to charge the unit with the adaptor for at least ten minutes before proceeding. At this point, the unit may have a normal start up described above if the main battery was very low. However, if the backup battery has completely discharged all memory will have been lost. After a 10 minute charging period, the unit should boot upon power up and the system will display the message.

WARNING: DATA IN HARD RAM WAS LOST
YOU MUST FORMAT HARD DISK BEFORE USE
PRESS ANY KEY TO CONTINUE.
WAIT.

Press the [ENTER] key or any other character key, and the unit will boot as above, with a different message

at the end.

MEMORY TEST nnn KB
Toshiba Personal Computer MS-DOS Version 3.30S
Bad or missing /CONFIG.SYS
It is now (day of week) (month) (day of month), (year)
C:>

With the adaptor plugged in it is possible to proceed with initialization of the system and this must be done before the unit can interact with the Handar 540A data system.

To proceed, place the TOGA System disk into the floppy drive located at the right rear of the unit and enter the following:

a:
press <Enter>, then type

setcnfg
and press <Enter>

You will be presented with a list of instructions on how to reconfigure the system. You may page through these instructions (they are a bit confusing) by pressing the enter key twice. A table will appear listing the various setup options which may be changed. This table is shown below with the parameters set to their proper values.

```
┌──────────────────────────────┬─────────────────┬──────────────────────┐
│                              ║ SYSTEM   SETUP  ║                      │
├──────────────────────────────┴─────────────────┴──────────────────────┤
│ Set The RAM Config.sys File                  =  No                    │
│ Config.sys File                              =  RAM                   │
│ Boot Priority                                =  Normal                │
│                                                                       │
│ Hard Ram Size                                =   384KB                │
│ Built-in Expanded Memory Port Address        =  258H                  │
│ Option Expanded Memory Port Address          =  208H                  │
│ Resume Mode                                  =  Boot                  │
│ External FDD/PRT                             =  Printer               │
│ Display Mode                                 =  Normal                │
│ Display Auto Off                             =  03 Min.               │
│ Primary Display Type                         =  Color[80*25]          │
│ Built-in TS-232C Port Assign.                =  COM1                  │
│ Built-in Modem                               =  Disable               │
│ Built-in Modem Power                         =  OFF                   │
│ Battery Alarm                                =  Enable                │
│ System Speaker                               =  Enable                │
│ Parallel Printer Port                        =  Output Port           │
├──────────────────────────────┬─────────────────┬──────────────────────┤
│                              ║ Instruction     ║                      │
├──────────────────────────────┴─────────────────┴──────────────────────┤
│ ←& → KEYS-Select Values. ↓ & ↑ KEYS-Move Options. F5-Sets             │
│                            Defaults                                   │
│     EXIT: Enter - Accepts Changes. Esc - Disregards Changes.          │
└───────────────────────────────────────────────────────────────────────┘
```

9

The values in the table may be changed by using the left and right arrow keys, which toggle through the allowable choices. Most of the entries will be correct, but carefully check that each corresponds to the setting in the table, especially check the first entry to see that it is set to "No" and the second entry and be sure it is set to RAM not ROM. Once the values in the table are correct press

<Enter>

You will be prompted with the question at the bottom of the screen

Are you sure? [Yes / No]

Yes will be highlighted in reverse video.

Press <Enter> and you will be presented with some more instructions. Press any key to continue. You will be asked if you wish to continue. Press <Enter> again and you will be given still another WARNING that all data on the D: disk will be lost and prompted with:

Proceed with Format (Y/N)?

Press <Y>

then press

<ENTER>

and the system will proceed to reformat the D: disk, which is the RAM disk and will install the hardware necessary to interact with the data system. Although you will be prompted to remove the disk and reboot the computer, before doing so you must copy the config.sys file from disk a: to disk d:. Since you are now on disk d: merely enter

copy a:config.sys
<Enter>

After copy the computer displays

    1 File(s) copied

Now you can remove the floppy disk from the computer. You should do so by pressing the small button just below the disk drive slot. Then you may reboot the system by pressing Ctrl, Alt and Del all at the same time, or alternately by simply turning the computer off and then back on. The computer should now respond with the proper prompt

(Day Date Time) HANDAR 545C PROGRAMMING/DATA COLLECTION SET
D:\>

If the day, date and time are correct it is OK to proceed. The day, date and time must be set to within three seconds of the correct GMT. If they are in error they may be corrected as follows:

Type the command "date" and the computer will prompt with

Current date is (Day, Date)
Enter new GMT date(mm-dd-yy)

Enter the new number of the (GMT) month-day-year each in a two digit format duplicating the format on the screen and press

<Enter>

The day and date should now be correct but you must still correct the time. Type "time" from the keyboard and the computer will respond with

Current time is: hh:mm:ss.ss
Enter new time:

Enter the new time (GMT) according to the format above using 00 for the last two digits and press

<Enter>

The system should respond with the proper time and Handar prompt. The computer is now ready to perform program upload or download, data retrieval or to be stored away until later needed. However, it is recommended that the computer be stored with the charger installed, otherwise the above reinitialization procedure will need to be repeated if the batteries become discharged.

3.3 Loading a program from the Toshiba 1000SE computer into the Handar 540A data collection platform

If for any reason the power to the Handar 540A data collection platform is interrupted, it will be necessary to reload the operating program into the data collection unit. This could happen if the battery within the unit becomes completely discharged. Also, static electricity could cause the program to be lost. In either case it will be necessary to reload the program into the data unit. In order to load a program from the computer into the data system the Handar software must be installed on the RAM disk (disk D:). This will be the case if upon powerup the computer displays the Handar prompt as discussed above. If this is not the case, it will be necessary to reinitialize the system as described in section 3.2. After the computer is properly initialized the data system operating program may be installed. This program is stored in two places on the computer system. First, it is stored in the RAM disk (disk D:) under the file name TOGARAD.PRG. If the batteries in the computer have never become discharged this file should remain on disk D:. If it was necessary to reinitialize the computer the program will have been lost from the RAM disk. In that case, after recharging and reinitialization, the program can be copied from a diskette into the RAM disk as follows: It is recommended that the file copy procedure described below be performed indoors.

After the computer is turned on and the (Day Date Time) Handar 545C PROGRAMMING/DATA COLLECTION SET message is displayed, insert the disk marked PROGRAM into the disk drive near the back on the right hand side of the computer. Then type:

d:

press <Enter>

The computer will now be addressing the d: disk and will display

11

D:\>

then type

copy a:\togarad.prg

and press <Enter>

The computer will respond with

1 File(s) copied
D:\>

The program will be copied from the disk drive into the RAM disk. It is also important to be sure the time and date in the computer's internal clock are correct. The day, date and time must be correct to within three seconds of the correct GMT. If the day, date, time block is in error follow the procedure outlined above for resetting them. Remove the diskette from the drive by pressing the button below the disk drive and store the disk in its box. The computer may then be carried into the field to load the program into the data system.

The computer must be connected to the data system using the cable marked "RS232". The cable is connected to the computer by lowering the small latched door located on the left hand side of the back of the unit as viewed from the rear. Plug the cable into the smaller of the two connectors. The computer must be OFF when the RS-232 cable is connected to the HANDAR data unit. The cable plugs into the data system's port which is marked "PROGRAM I/O". It will first be necessary to disconnect the cable already connected to this port. Temporarily hang the disconnected cable on the tripod system so it does not become soiled or wet on the ground. After connecting the "RS232" cable turn the computer on by depressing the switch about midway back on the left side of the unit for a couple of seconds and then release it. The unit should respond with the prompt:

Day Date Time HANDAR 545C PROGRAMMING/DATA COLLECTION SET
D:\>

Before actually entering the HANDAR software program, it is worthwhile to note that the responses to the prompts must be made exactly as shown. In addition, many of the keyboard entries will take on new functions that are indicated by the decals which have been affixed to the keys. This is particularly noticeable if you type an entry incorrectly and try to correct it by using the backspace or delete keys. Using these keys will usually generate an error message. The proper way to reenter data is to use the "CLEAR" function which is activated by pressing the "X" key. However, if you inadvertently press the delete or backspace in an attempt to make a correction, you can usually return to the same instruction by pressing the ENTER key after the error message. If you find yourself at a point in the program other than where you should be, you can use the SCROLL UP function (the "U" key) or the SCROLL DOWN function (the "V" key) to move through the prompts to the proper position.

Type

545c

and press

<Enter>

The unit will display a menu page, with a Welcome Banner followed by:

P   HANDAR 540A DCP - REV 4.Q
SYSTEM PROG REQUIRED - PRESS ID

Press the key marked "ID" which is the letter I on the keyboard
The computer will respond

P   ID   00000000

For Chuuk type   2110327C

and press

<Enter>

The computer will respond with

P   ID   2110327C

Then press the F1 function key on the top row of the keyboard

<F1>

The unit responds with

LOAD PS PROG → DCP: PRESS ENTER

Press <Enter> and you will be prompted for a file name
Type the file name as

D:\TOGARAD.PRG

and press

<Enter>

The computer will display

P LOADING PROGRAM ***

and a flashing message will be displayed in the lower portion of the menu screen indicating the program
filename which is being loaded. After the program load is complete the unit will display

P   DONE_

At this point the program is loaded.

Now all that is necessary is to place the data system in the "RUN" mode. Simply press "RUN" which is the
<Y> key and the unit will display

R RUN/MONITOR MODE

At this point the unit is fully programmed and the session may be exited by entering the F10 key on the upper row of the keyboard

<F10>

The unit will return to the HANDAR prompt and then display

D:\>

At this point the computer may be turned off by depressing the on/off switch on the left side of the unit for a few seconds. Then, disconnect the "RS232" cable and reconnect the WWV radio cable which was originally connected to the PROGRAM/IO port. Store the computer and cable (the computer should be connected to the charger).

3.4 Downloading data from the HANDAR 540A

The primary means of data transfer from the data collection site to Colorado State University (where it will be processed) is the GOES satellite Data Collection Platform. In the event that technical problems arise using this service it will be necessary to download the data onto floppy disks using the Toshiba T-1000 SE laptop computer. Even if the power to the Handar 540 data station is interrupted the data stored in the 540's RAM will be preserved by means of lithium battery backup. The Handar 540 has been equipped with 256 Kbyte of RAM for this purpose and will easily store up to 3 weeks worth of data based on the current sampling rate. Thus, even if satellite communications are interrupted for that period of time, a continuous data record is still possible.

In order to perform this function the computer must contain in its memory the Handar communications software. This software is normally found on the RAM disk, disk D:. The software will be found of the D: disk if the computer has a normal power up or if reinitialization of the unit has been performed as described in section 3.2. In either case the computer will be ready to perform data download only if the following prompt appears on the screen:

HANDAR 545C PROGRAMMING/DATA COLLECTION SET

D:\>

If this is the case the computer may be carried to the station with the RS232 cable. The cable attaches to the computer via a port located behind the small plastic door on the left hand side of the back of the computer as viewed from the rear. The RS232 cable connects to the HANDAR 540 data collection station via the "PROGRAM I/O" port. This port also accepts the WWV radio receiver information. Disconnect the cable currently connected to the "PROGRAM I/O" port and hang the cable so it does not become soiled or wet. Connect the RS-232 cable to the port and turn on the computer.

At the D:\> prompt type:

DPP

then press <Enter>

The software will present a menu of functions and prompt for your choice with:

ENTER SELECTION

14

Type

<F1>

The computer will log onto the 540 data collection platform and a RUN-mode log-on message will appear as:

R   HANDAR 540A-1 DCP - REV - 4.Q

Insert a floppy disk into the drive on the back right hand side of the computer. (Note all floppy disks supplied with the computer have already been formatted.)

Type:

- (the "minus" key)

Then press <Enter>

The following messages will appear on the screen

R   SAVING DATA ***
Enter data file name: 2110327C.BDT

The file name presented is a default file name which must be changed. This is necessary because merely using the filename above will cause the data to be written to the D: disk under the default file name and there is not enough space on the D: disk to contain this information.

Instead type:

A:2110327C.BDT

<Enter>

Several messages will begin to appear on the screen giving information on the progress of the data transfer. When the process is finished the following message will appear:

Transfer Complete - press any key to return to main menu

Pressing any key will cause the main menu to be presented. In order to exit the program enter <F10> at the prompt. Remove the floppy and write the date of the download process on the label. Turn the computer off. Disconnect the RS-232 cable and reconnect the WWV radio cable to the PROGRAM/IO port. Store the computer with the AC adaptor plugged in. The floppy should be mailed as soon as possible using one of the preaddressed padded envelopes provided with the station equipment.

3.5 Radiometer Calibration

In order to assure the quality of the dataset it will be necessary to perform calibration checks on approximately a bimonthly schedule. This procedure is simple and will take only a few man-minutes to perform. Included with the station is a stainless steel thermos which has been coated with a special emissive paint on the inner surface. A thermistor has been attached to the inner surface to measure the temperature of the interior surface of the thermos. The thermos cap will serve to block the incoming solar radiation in order to perform

an optical zero check on the pyranometer.

You will be contacted by personnel from the Dept. of Atmospheric Science as to the requested timing of each calibration. In order to perform the calibration place the thermos opening over the silver dome of the pyrgeometer. Center the rim of the thermos using the three small screws that secure the white radiation shield as a guide for centering. Disconnect the cable connected to the AIR TEMPERATURE/RELHUMIDITY port on the Handar 540 data collection system being careful not to let the connector become soiled or wet. Connect the cable from the thermos to this port. Place the thermos cup over the pyranometer's clear dome centering it as much as possible; see Fig 2. The thermos and cup should be left in place for a period of approximately 1 hour. At the end of that time remove both the thermos and the cup, disconnect the thermos cable from the data system and reconnect the air temperature sensor cable to the port. Store the thermos calibration unit with the station equipment for later use. The calibration data will be sent as part of the normal data stream. No other action is necessary on your part.

APPENDIX B

Data Processing Procedures

PROCEDURES FOR ARCHIVING AND REDUCING
TOGA-COARE RADIOMETRIC DATA

C O N T E N T S

PROCEDURES FOR ARCHIVING AND REDUCING
TOGA-COARE RADIOMETRIC DATA

A. Overview

1. Raw data are on 3-1/2" IBM-PC compatible diskettes and pseudo-binary files which are downloaded from NESDIS by the PC via telephone modem. All archiving and review of raw data occurs on the PC. All data reduction (calibration) occurs on the PC. The final product, monthly archives containing daily files of calibrated radiometric measurements, end up on a SUN workstation (*trueno*) which is connected to the Internet. This document describes the procedures for archiving and reducing the data and keeping track of the status of data processing which is in progress. There are also flow charts depicting the data processing sequence which is described here. It is suggested that you refer to them to get a better understanding of the overall process.

The data and programs occupy a few subdirectories on the PC:

c:\users\toga	programs
c:\users\toga\archive	archive information
c:\users\toga\doc	documentation
c:\users\toga\raw	raw data
c:\users\toga\reduced	reduced (calibrated) data

Since most of the data reduction occurs on the PC, there are several batch command files which will simplify and speed up this processing. Furthermore, most of the processing can be done on the PC's ram disk (D:) which is faster than the hard disk. All contents of the ram disk are lost whenever you power off or reboot, so the results of data processing must be saved to the hard disk.

Throughout the processing, you will see file names like "ma920521.xxx". The convention is to name files after the station and the date represented by the data, for example, "ma920521.xxx" = Majuro 1992 May 21. The station identifiers are
    MA = Majuro, DA = Darwin, PN = Pohnpei, KA = Kavieng,
    TK = Chuuk
The file extension "xxx" represents the type of data:
    "dsk" = diskette source, "sat" = satellite source,
    "dat" = final reduced and calibrated data.

B. Data Archives

Archives exist for both raw and reduced data.

1. The Raw Data archive consists of:
   a) 3-1/2" diskettes (the original data)
   b) 5-1/4" disks containing zoo archives of the original data
      files
   c) copies of these zoo archives on the PC in directory
      c:\users\toga\raw

2. Archives of the reduced data files (ssYYmmDD.dat) are in three
   locations:
   a) zoo files on the PC in c:\users\toga\reduced
   b) 5-1/4" disks containing these zoo files
   c) SSYYdd.tar.Z files on *trueno* in /users/data/ftp/toga

3. Indexes of data
   b) on the PC, DISKETTS.WQ! lists the raw diskettes and raw files
   a) on *trueno*, 00INDEX lists the complete collection of *.tar.Z
      files

C. Data Ingest

1. Summary

There are 4 different types of data sources: two kinds of data loggers (Handar & Campbell) plus satellite download. There are three different initial procedures. All data ingest is done on the PC.

2. Satellite data

The names of satellite data files are based on the day and time they are downloaded from NESDIS. For example, "12141400.do" identifies a download made on December 12 at 14:00. These files hold about 3 days data from Chuuk, Majuro and Pohnpei, and they are typically 15 to 30kb in size.

a) Download via modem using Procomm
   (detailed instructions on separate sheet)

b) Save the new *.do files to 5-1/4" floppy disk
   The floppy disks are numbered do1, do2, ...
   ```
   copy *.do a:\
   ```

c) When this floppy disk is full, put its *.do files in a zoo archive:
   ```
   cd \users\toga\raw
   zoo a do## a:\*.do
   ```

   and copy this zoo archive to a 5-1/4" archive disk
   ```
   copy /v do##.zoo a:\
   ```

d) Run TRANS9.EXE to unpack the *.do data. It creates one file for each day, with output file names ssYYmmDD.sat

   Note - this step can be efficiently done with larger sets of *.do files by using SATO.BAT on the ram disk (D:). SATO.BAT will also concatenate and sort the data and will perform the calibration step (described later).

   An easy way to get started is to use TO_D.BAT which moves programs, etc., to the ram disk. Then copy the new *.do files to D:, change to D: as your default directory, and run SATO.BAT. Once you start processing a batch of data with SATO.BAT, it's important that you finish reducing the *.sat files (to produce *.dat files as described later in these instructions), and then delete *.sat. Otherwise, the next time you use SATO.BAT, these old *.sat files will be appended along with the newer data, and you will get gigantic files with multiple identical entries.

3. Diskettes mailed to CSU - inspect and log in the diskette

a) Is the diskette's visual appearance okay?
   What's written on the label? (Pohnpei, date, ...)

page 3

Before putting the diskette in the disk drive, make sure it is read-only protected.

b) Tell Chris Cornwall if there is a problem, like no data or unreadable diskette, etc.

c) Raw data diskettes have little sequence numbers penciled on the labels. For a newly arrived diskette, write the next sequence number on the diskette's label and enter descriptions of the diskette's files in the data catalog (Quattro spreadsheet c:\users\toga\archive\DISKETTS.WQ!)

d) Create a new zoo archive for the data file[s]. Put the zoo archive in c:\users\toga\raw and also copy it to the current 5-1/4" floppy disk archive.

4. Stations with Handar data loggers (Majuro, Pohnpei and Chuuk)

a) Copy the raw binary data file (usually "data.bdt") to a workspace on the PC, such as the ram disk (D:).

b) Use program DPP.EXE to unpack the binary data. DPP is provided by the Handar company and is a menu-driven program. Select 7, 2, and input the name of the raw data file.

c) DPP.EXE tells you the start and end day/times of the data. Write these down so you can put them in the data catalog later.

d) Specify the output file name ssYYmmDD.dsk, where YYmmDD is the first day of data. DPP.EXE will then unpack the data.

e) When DPP.EXE is finished, you can exit by selecting 10, 10.

f) Delete the binary data file from your working directory.

5. Stations with Campbell data loggers (Darwin and Kavieng)

a) Copy the raw data file to a workspace on the PC, such as the ram disk (D:).

b) Use the list utility to look at the file and find the start and end day/times of the data. The END key will move to the end of the file, and the HOME key will move to the start. For example:

```
    L C001.DAT

    101,69,15,-.296,307.9,306.9,6.608,7.4,.864,31.23
         |   |____ time 00:15
         |_____ Julian day 69
```

At the end of these instructions is a table you can use to convert from Julian day to month and date. Write down the start and end times of this file so you can put them in the data catalog later (c:\users\toga\archive\DISKETTS.WQ!).

c) Use SP2COMMA.EXE to replace the commas with spaces:

```
    sp2comma 1 filename
```
It creates a new file: filename.!!! which you will rename ssYYmmDD.dsk (YYmmDD is the first day of data)

D. Calibration of Raw Data

1. Summary

The same procedure and same programs are used on all data,
regardless of source. Data are processed in batches of raw data,
where a batch consists of one raw data diskette (about one month
of measurements) or a collection of satellite *.do files. In the
calibration process, the batch of raw data becomes a batch of
reduced data. These batches do not usually fill a complete month.
Rather, they often cover parts of two months. Therefore, subsets
of different batches must be combined in order to accumulate a
full month of measurements. The data files are kept on the PC
until a full month of reduced data is available.

There is a heirarchy of raw data which should be followed during
the calibration and merging. Data derived from diskettes
(ssYYmmDD.dsk) are preferred over satellite data (ssYYmmDD.sat)
because the diskette data usually have fewer missing times and
fewer bad values. Therefore, the data reduction should rely
primarily on diskette data. Satellite data will be used to fill in
the gaps of missing data. Satellite data are especially useful
for a diagnostic look at data because they are recent; it's
usually more than a month before the diskette data arrive at CSU.

Calibration coefficients for all of the stations are in file
TOGA.CAL. This file should be updated whenever new calibration
information is available. TOGA.CAL is automatically read by
programs which need it. Another file, TOGA.LIM, contains limits of
expected raw and calibrated values. Errors will be detected
whenever data values fall outside these limits. It is also read
automatically by programs which need it. TOGA.LIM can be modified
if necessary.

As mentioned earlier, data processing will go faster and easier if
you use the ram disk. There is a batch file, TO_D.BAT, which
copies all of the necessary programs to the ram disk. The
following is a detailed discussion of the calibration process.

2. First, create the raw ssYYmmDD.dsk or ssYYmmDD.sat file in a
workspace area, such as the ram disk.

3. Then get some basic statistics for the raw data using
RAWEXTRM.EXE. Examine the minimum and maximum values and note if
any are obviously out-of-range (temperature less than 0 or > 40
Celcius, etc.). Other programs will automatically trap out-of-
range values and will let you know.

   a) RAWEXTRM.EXE makes a small summary file (ssYYmmDD.Ext)
      Add this file to the archive of extreme values
      (batch file RAWEXZ.BAT will do this step for you)

4. View the raw data using RAWPLOT.EXE

   a) Look for holes in data (missing data). It is cause for alarm if lots of data are missing or if the holes show up frequently.

   b) Out-of-range values are detected by the program (it beeps and blinks).

   c) If there are many out-of-range proglems, note the date and type of problem. Then consult with Chris on how to interpret the problem, especially if it's mysterious or occurs often.

5. Calibrate the raw data using REDUCE.EXE

   a) It creates daily files, named ssYYmmDD.dat

   b) Note that the first and last days on a diskette data file (ssYYmmDD.dsk) are likely to be incomplete, meaning they will probably not begin at time 00:00 or end at 23:59. Therefore, you will have to look for data to fill in the missing times from adjacent diskettes or satellite data. For this filling-in, you will have to do some editting, pruning, and appending from one *.dat file to another. More on this later.

   c) Delete the ssYYmmDD.dsk or ssYYmmDD.sat file from the ram disk.

   d) Put all of the reduced data files from this batch into a zoo archive on the PC in directory c:\users\toga\reduced.
   Make the name of the archive the same as the raw file prefix (ssYYmmDD), for example:
   ```
   D:> zoo a ma921209 *.dat
   D:> copy ma921209.zoo c:\users\toga\reduced
   ```

   You are now done with the raw data, so you can delete the raw data from the hard disk (c:\users\toga\raw\##.zoo). If you need it again, you can always copy it from the archive 5-1/4" disks or from the original raw data diskettes.

6. Collect a complete month of data so it can be sent to *trueno*. You can extract to the ram disk the ssYYmmDD.dat files which are in zoo archives on c:\users\toga\reduced. To see which archives overlap (have a few days in common), refer to the Quattro spreadsheet DISKETTS.WQ! and to your processing log. You may have to cut and paste to assemble complete days at the start or end of a batch of days. There may also be complete overlap from two batches, in which case you do not have to cut or paste; you only have to extract the full days.

   For example, to get all of the May 1992 Chuuk data out of two zoo archives and put them onto the ram disk:
   ```
   D:>
   D:> zoo x c:\users\toga\reduced\tk920420 tk9205*.dat
   D:> del tk920528.dat (not a full day)
   D:> zoo x c:\users\toga\reduced\tk920525 tk9205*.dat
   ```

E. Moving Data Files to *trueno*

1. Summary

    This is a two step process and uses an intermediate computer, HP
    workstation named "lion".

2. Have a complete month of ssYYmmDD.dat files in your working
   directory (ram disk).

3. From the PC ("bud"), use ftp to connect to *lion* and log in to
   your account:
   ```
   D:> ftp lion
   ```

4. Change to the subdirectory where data files are stored for
   transfer to *trueno*:
   ```
   ftp> cd totrueno
   ```

5. Transfer all data files from the PC to *lion*:
   ```
   ftp> prompt (turns off interactive confirmation)
   ftp> mput *.dat
   ```

6. Quit the ftp session
   ```
   ftp> quit
   ```

7. Now use telnet to log on to *lion* as an interactive user:
   ```
   D:> telnet lion
   ```

8. Change to the data subdirectory on *lion*, put the data files into
   tar archives and compress them to create a tar.Z file. Note that
   upper/lower case is important, for example:
   ```
   lion: cd totrueno
   lion: tar -fvc DA9301.tar da*.dat
   lion: compress -v DA9301.tar
   lion: rm da*.dat
   ```

9. Overnight, all files in this subdirectory are automatically
   transfered from *lion* to a subdirectory on *trueno*:
   ```
   /data/users/ftp/pub/incoming/fromlion
   ```

10. The following day, log on to *trueno*, confirm that the new files
    were transfered from *lion*, and move them to the ftp/toga area, for
    example:
    ```
    $ cd  /data/users/ftp/pub/incoming/fromlion      (alias fromlion)
    $ ls -l
    $ mv  DA9301.tar.Z  /data/users/ftp/toga
    ```

11. Log on again to *lion* and delete the totrueno/tar.Z files which
    were sent over last night:
    ```
    lion: cd totrueno
    lion: rm *.tar.Z
    ```

F. Updating the Data Index

1. Summary

   File OOINDEX is for the ftp users outside of CSU. It lists the
   contents of the *.tar.Z archives and tells how much missing or bad
   data each monthly file contains. A program on *trueno* will scan
   through the daily files, which you will unpack, and calculate how
   complete the archives are.

2. Log onto *trueno*, put copies of the compressed archives into the
   daily file sub-directories and unpack them, for example:

   ```
   $ toga                  (alias cd /data/toga)
   $ cd Majuro
   $ cp /data/users/ftp/toga/MA9212.tar.Z .
       (NOTE: period is important_____↑)
   $ uncompress -v MA9212.tar.Z
   $ tar -fvx MA9212.tar
   $ rm MA9212.tar
   ```

   You have now unpacked all 31 of the ma9212*.dat files.

3. Run time_logger.x to find out how complete the daily files are.
   This information will be used in the OOINDEX file also.

   ```
   $ cd /data/toga
   $ time_logger.x          (then answer the questions)
   ```

   This creates a new file, such as   /data/toga/logs/ma92dec.log
   and appends summary information to /data/toga/logs/master_time.log

   One new line will be appended to the end of master_time.log, and
   you will probably have to edit it to put the new entries in the
   correct locations, that is, to group all Majuro entries together
   and to have them in chronological order.

4. Update the OOINDEX file using the new information from
   master_time.log, for example:

   ```
   $ cd /data/users/ftp/toga          (alias f)
   $ vi OOINDEX
   ```

   Move the cursor down to this line and delete everything below:

station	mon/yr	daily % range	hour % range	month %
ma	jul/91	0.0- 99.8	26.0- 29.0	27.4
ma	aug/91	0.0-100.0	54.0- 61.0	60.7
ma	sep/91	0.0- 99.8	76.0- 80.0	79.3

   Then read in the new information:
   ```
   :r /toga/logs/master_time.log
   ZZ                                  (exit from vi editor)
   ```

G. Data Processing Log

   1. Summary

      It is important to keep track of the status of data processing
      because there are many steps and many different files involved in
      the data processing. The following system is suggested as a guide.

   2. The steps in data processing are
         (1) Ingest
         (2) Calibration
         (3) Transfer to *trueno*
         (4) Update 00INDEX

      PROCESSG.WQ! is a Quattro spreadsheet on the PC that can be used
      to create a template with entries for individual months and
      individual stations. As you reduce each batch of data, make
      entries 1, 2, 3, and 4 in this template to monitor your progress
      and to help identify where gaps occur. It also tells you which
      archive has the raw data for particular time periods.

   3. The diskette data catalog (DISKETTS.WQ!) is also a Quattro
      spreadsheet, and you can use it to easily sort the entries by
      station name and by the dates covered by the data. This will help
      you find and fill the gaps with satellite data. For example, the
      raw data for September and October 1991 for Chuuk are on diskettes
      5 and 6 (also on zoo archives 5.zoo and 6.zoo).

                    start   end
            5: 910916.2204   911024.2210
            6: 911101.2216   911209.2222

      Although they are sequential, there is a gap in the data from
      October 24 to November 1. You can look for satellite data to fill
      in this gap. Search for *.do files with creation dates about 3
      days after the date you want. You can also extract all the *.do
      files from a do##.zoo archive covering the time period you want.
      Then you can process all these *.do files using SAT0.BAT and pull
      out the specific dates you want.

      After you have searched all the sources and extracted and reduced
      all available data for Chuuk in October 1991, you can then
      assemble the most complete set of tk9110*.dat files on the PC and
      transfer them to *lion* and *trueno*.

H. Suggestions to Improve Data Processing

1. Some diskettes are mailed here and have nothing written on the adhesive label to identify where it came from. This uncertainty is avoided by pre-formating and labeling the diskettes which CSU sends to each station. The DOS LABEL command could be used to write volume labels corresponding to the station identification.

2. Upgrade RAWPLOT.C to add an option to calculate and plot calibrated data, instead of just raw values. This should be fairly straightforward since REDUCE.C is very similar to RAWPLOT.C and has all the code to perform the calibrations. Another useful upgrade would be to put tick marks on the plots so you can estimate numerical values better.

3. Update RAWEXTRM.C to recognize the data source as satellite, Handar disk or Campbell disk. RAWPLOT.C and REDUCE.C already do this, so it should be easy to propagate this capability to RAWEXTRM.C.

4. RAWPLOT.C, RAWEXTRM.C, and REDUCE.C have some common functions: read_limits(), read_calibration_coefficients(), get_file_list(), data_ingest(), and open_data_file(). These are reproduced in each source code. It would be preferable to put these functions into a common include.h file so that changes would automatically be propagated into all three programs, and software maintenance would be simplified. Likewise, there are common declarations for variables and functions, and these should also be in a common include.h file.

TOGA-COARE RADIOMETRIC MEASUREMENTS - CATALOG OF ORIGINAL DATA DISKETTES
        file: **disketts.uql**
    updated: 30-Jun-93

disk #	station name	file name	file size	data start date.time	data end date.time	comments
			1.7E+07			
1	chuuk	2110327C.BDT	168166	910621.0437	910624.2337	
1	chuuk	2110327C.DAT	696058	910621.0437	910716.0437	
1	chuuk	211327C.BDT	25646			
2	chuuk	2110327C.BDT	255554	910716.0001	910801.0534	
2	chuuk	2110327C.DAT	451936			
3	chuuk	2110327C.BDT	255554	910708.2352	910815.2358	
4	chuuk	2110327C.BDT	255554	910806.0058	910913.0104	
5	chuuk	2110327C.BDT	255554	910916.2204	911024.2210	
6	chuuk	2110327C.BDT	255554	911101.2216	911209.2222	
7	chuuk	2110327C.BDT	255554	911220.2331	920127.2337	
8	chuuk	2110327C.DAT	1058094			
8	chuuk	2110327C.BDT	255554	920215.2310	920324.2316	
9	chuuk	2110327C.DAT	6400			
9	chuuk	2110327C.BDT	255554	920316.0519	920423.0525	
10	chuuk	2110327C.BDT	255554	920420.2337	920528.2343	
11	chuuk	2110327C.BDT	255554	920525.0622	920702.0628	
12	-x-	--no files--	0			
13	majuro	211007E6.BDT	228243			DPP.exe can't read
13	majuro	211007E6.DAT	237568	910705.2008	910714.0853	
14	majuro	211007E6.BDT	66750	910813.0302	910823.0050	
14	majuro	211007E6.DAT	275906	910813.0302	910823.0050	
15	majuro	211007E6.BDT	220666	910823.0053	910924.2023	
16	majuro	211007E6.BDT	255554	911114.2008	911222.2014	
17	majuro	211007E6.BDT	254042	920317.0408	920423.2250	
18	majuro	211007E6.BDT	255554	920208.0359	920317.0405	
19	majuro	211007E6.BDT	242618	911222.2017	920127.2211	
20	majuro	211007E6.BDT	61150	920609.2117	920618.2305	
21	majuro	211007E6.BDT	105726	920525.0414	920609.2114	
22	majuro	211007E6.BDT	255554	920622.0238	920730.0244	
23	chuuk	327C1022.BDT	255554	920914.0613	921022.0619	
23	pohnpei	210A1017.BDT	255554	920909.0434	921017.0440	
23	majuro	07E61012.BDT	255554	920904.0308	921012.0314	
24	majuro	211007E6.BDT	255554	920730.2123	920906.2129	
24	majuro	211007E6.DAT	5220			
25	majuro	MAJURO.BDT	129115	930131.2225	930228.2155	
26	majuro	MAJURO.DAT	0			
26	majuro	MAJURO.BDT	255483	921207.1240	930131.2220	
27	pohnpei	DATA.BDT	255483	930202.1240	930329.2220	
28	majuro	211007E6.DAT	59392	911209.1014	911211.1323	all garbage
28	majuro	211007E6.BDT	152			
29	??	D910702A.011	634880	521215.0000	850101.0000	invalid DPP data
30	chuuk	2110327C.BDT	255554	920724.0331	920831.0337	
31	chuuk	2110327C.BDT	255554	920828.0531	921005.0537	
32	chuuk	DATA.BDT	59067	921024.0630	921106.1110	
33	chuuk	DATA.BDT	189531	921106.0115	921217.0325	
34	chuuk	DATA.BDT	255483	921218.1545	930212.0125	
35	chuuk	DATA.BDT	255483	930105.1410	930301.1410	
36	kavieng	000.DAT	171626	930124.0640	930205.0325	
37	kavieng	C001.DAT	348977	930205.0330	930301.0405	
37	kavieng	C002.DAT	53			
38	darwin	TOGA1.DAT	87058	930119.0550	930125.0540	
39	darwin	C001.DAT	542229	930202.0540	930310.0010	
40	darwin	C001.DAT	409277	930310.0015	930405.2300	
41	majuro	MAJURO.BDT	148523	930228.2200	930402.0235	
42	chuuk	DATA.BDT	255483	930210.1235	930406.2216	
43	chuuk	DATA.BDT	255483	930310.1205	930504.2145	

44	majuro	MAJURO.BDT	255483	930312.1200	930506.2140	
45	majuro	211007E6.DAT	0			
45	majuro	211007E6.BDT	173592			DPP.exe read error
45	majuro	DATA.BDT	432	910613.0232	910613.0329	
46	darwin	C001.DAT	835053	921209.0135	930202.0535	
47	pohnpei?	DATA.BDT	171931	930329.2225	930506.0455	
48	darwin	C001.DAT	572917	930405.2305	930512.2350	
49	kavieng	000.DAT	439043	930401.0010	930430.2035	
50	kavieng	C002.DAT	101			
50	kavieng	C001.DAT	450014	930301.0415	930331.2355	
51	kavieng	000.DAT	439043	930401.0010	930430.2035	same as #49

TOGA-COARE RADIOMETRIC MEASUREMENTS
  data processing record

  file: status.wql
updated 2-July-1993

key: # = diskette of raw data
     1 = ingest
     2 = calibration
     3 = transfer to lion/trueno
     4 = update ODINDEX on trueno

month

station	9101	9102	9103	9104	9105	9106	9107	9108	9109	9110	9111	9112
Chuuk	░	░	░	░	░	1-1234	1-1234	3-1234	4-1234	5-1234	6-1234	6-1234
							2-1234	4-1234	5-12			7-12
Majuro	░	░	░	░	░	///	13-1234	14-1234	15-1234		16-1234	16-1234
						///		15-12				19-12
Pohnpei	░	░	░	░	░	///						
						///						

month

station	9201	9202	9203	9204	9205	9206	9207	9208	9209	9210	9211	9212
Chuuk	7-1234	8-1234	8-1234	9-1234	10-1234	11-1234	11-123	30-1234	23-1234	32-1234	33-1234	33-1234
			9-12	10-1234	11-1234		30-12	31-12	31-12	23-12		34-1234
										31-12		
Majuro	19-1234	18-1234	18-1234	17-1234	21-1234	20-1234	22-1234	24-1234	23-1234	23-1234		26-1234
			17-12			21-12	24-12		24-12			
						22-12						
Pohnpei									23-12	23-12		
Darwin	░	░	░	░	░	░	░	░	░	░	///	46-1234
	░	░	░	░	░	░	░	░	░	░	///	
Kavieng	░	░	░	░	░	░	░	░	░	░	///	///
	░	░	░	░	░	░	░	░	░	░	///	///

month

station	9301	9302	9303	9304	9305	9306	9307	9308	9309	9310	9311	9312
Chuuk	34-1234	34-1234	35-1234	42-1234								
		35-1234	42-1234	43-1234								
Majuro	25-1234	25-1234	41-1234	41-1234								
	26-1234	41-1234	44-1234	44-1234								
Pohnpei		27-12	27-1234	47-1234	47-12							
			47-1234									
Darwin	38-1234	39-1234	39-1234	40-1234	48-12							
	46-123		40-1234	48-12								
Kavieng	36-1234	36-1234	37-1234	49-1234								
		37-1234	50-1234									

file: 00INDEX
This index file is for reference by ftp users of TOGA radiometric data
and is intended to help find the data they want. These data files are
available to the scientific community-at-large via anonymous ftp on
trueno.atmos.colostate.edu.

See file 00README for additional information.

Percentages of data available for different months at the different sites
are shown in the following table. This information is periodically updated,
as new data files become available.

station	mon/yr	daily % range	hour % range	month %
ma	jul/91	0.0- 99.8	26.0- 29.0	27.4
ma	aug/91	0.0-100.0	54.0- 61.0	60.7
ma	sep/91	0.0- 99.8	76.0- 80.0	79.3
ma	nov/91	0.0- 99.8	51.0- 57.0	53.8
ma	dec/91	99.0- 99.8	95.0-100.0	99.8
ma	jan/92	0.0- 99.8	83.0- 87.0	86.7
ma	feb/92	0.0- 99.8	69.0- 76.0	75.1
ma	mar/92	96.9- 99.8	95.0-100.0	99.7
ma	apr/92	0.0- 99.8	73.0- 77.0	76.3
ma	may/92	0.0- 99.8	18.0- 23.0	22.0
ma	jun/92	0.0- 99.8	82.0- 90.0	89.3
ma	jul/92	21.7- 99.8	95.0-100.0	97.2
ma	aug/92	98.5- 99.8	95.0-100.0	99.8
ma	sep/92	87.5- 99.8	94.0-100.0	99.0
ma	dec/92	0.0- 99.7	71.0- 81.0	78.7
ma	jan/93	99.0- 99.7	92.0-100.0	99.6
ma	feb/93	99.0- 99.7	92.0-100.0	99.6
ma	mar/93	99.0- 99.7	92.0-100.0	99.7
ma	apr/93	99.0- 99.7	92.0-100.0	99.7
ka	jan/93	0.0- 99.7	21.0- 26.0	24.8
ka	feb/93	99.0- 99.7	92.0-100.0	99.6
ka	mar/93	82.3- 99.7	89.0-100.0	99.1
ka	apr/93	85.4- 99.7	91.0-100.0	99.2
da	dec/92	0.0- 99.7	65.0- 74.0	73.7
da	jan/93	99.0-100.0	92.0-100.0	99.7
da	feb/93	0.0-100.0	93.0- 96.0	95.6
da	mar/93	99.0-100.0	99.0-100.0	100.0
da	apr/93	95.8-100.0	93.0-100.0	99.6
pn	mar/93	95.8- 97.6	85.0-100.0	96.9
pn	apr/93	96.9- 97.6	85.0-100.0	97.1
tk	jun/91	0.0- 99.8	29.0- 33.0	32.6
tk	jul/91	99.0- 99.8	95.0-100.0	99.8
tk	aug/91	0.0- 99.8	46.0- 48.0	48.3
tk	sep/91	0.0- 99.8	44.0- 50.0	46.8
tk	oct/91	0.0- 99.8	74.0- 77.0	77.0

tk	nov/91	6.9- 99.8	92.0-100.0	96.7
tk	dec/91	0.0- 99.8	61.0- 65.0	64.2
tk	jan/92	0.0- 99.8	83.0- 87.0	86.9
tk	feb/92	0.0- 99.8	46.0- 51.0	48.3
tk	mar/92	99.0- 99.8	95.0-100.0	99.8
tk	apr/92	99.0- 99.8	95.0-100.0	99.8
tk	may/92	73.1- 99.8	92.0-100.0	98.9
tk	jun/92	99.0- 99.8	95.0-100.0	99.8
tk	jul/92	0.0- 99.8	28.0- 32.0	29.4
tk	aug/92	99.0- 99.8	95.0-100.0	99.8
tk	sep/92	99.0- 99.8	95.0-100.0	99.8
tk	nov/92	98.6- 99.7	92.0-100.0	99.6
tk	dec/92	13.9- 99.7	89.0- 97.0	94.7
tk	jan/93	99.0- 99.7	91.0-100.0	99.6
tk	feb/93	99.0-100.0	92.0-100.0	99.7
tk	mar/93	99.0- 99.3	83.0-100.0	99.3
tk	apr/93	99.0- 99.3	83.0-100.0	99.3

file: 00README
This file is for reference by ftp users of TOGA radiometric data.

See also file 00INDEX for a current index of data available via ftp.

Data files are available to the scientific community-at-large via anonymous ftp on trueno.atmos.colostate.edu. This 00README file identifies what these data sets are, describes how to interpret the columns of numbers, briefly identifies the instrumentation used at the sites, and provides instructions for finding and unpacking the archive files.

Additional technical information is in a hard copy report:
    $$$ title and number of blue book $$$
which is available from Colorado State University, Department of Atmospheric Science, Fort Collins Colorado, USA, 80523. If you have any question, corrections, additions or suggestions for this data set or the information files, please send your comments to:
    cornwall@trueno.atmos.colostate.edu.

```
----------------------------------------------------------------
-- GENERAL DESCRIPTION OF DATA --
```

Radiometric and other measurements are being taken to help estimate the
surface radiation budget in support of TOGA-COARE. Instrument sites
were established in the western Pacific Ocean in July 1991 and October
1992. These stations are:

| | | | | hours later | data |
station	identifier	latitude	longitude	than GMT	start
Majuro	MA	7deg 5'N	171deg 23'E	12	July 1991
Pohnpei	PN	6deg 58'N	158deg 13'E	11	July 1991
Chuuk	TK	7deg 27'N	151deg 50'E	10	July 1991
Darwin	DA	12deg 25'S	130deg 51'E	9.5	October 1992
Kavieng	KA	2deg 30'S	150deg 48'E	10	October 1992

Previous to October 1992, measurements were made every 3 minutes, and
thereafter, every 5 minutes.

The data are available as daily files, one for each station, covering
00:00:00 GMT through 23:59:59 GMT. The daily file names follow the
format ssYYMMDD.dat, where
        ss = Station abbreviation (MA, PN, TK, DA, KA)
        YY = Year (91, 92, 93)
        MM = Month (01, 02, 03, ... 12)
        DD = Day of month (01, 02, 03, ... 31)

These daily files are combined into monthly archives using the UNIX tar
utility into one file per month per station, and this file is compressed
to save on disk space. For example, data for January 13, 1993, for the
Kavieng site are in file ka930113.dat which is within the tar file
KA9301.tar, and this tar file is compressed as KA9301.tar.Z.
Instructions on obtaining and unpacking these files are given later in
this 00README file.

The daily files are ASCII text, arranged as columns of numbers, and each
line of data represents one instantaneous set of measurements. The
columns contain:
        Column 1: GMT in decimal hours, i.e. 1:30PM GMT = 13.500
        Column 2: Local time in decimal hours
        Column 3: Instantaneous infrared irradiance in Watts/meter^2
        Column 4: Instantaneous solar irradiance in Watts/meter^2
        Column 5: Instantaneous ultraviolet irradiance in Watts/meter^2
        Column 6: Instantaneous air temperature, kelvin

Missing data are indicated by entries of "-888.8" and bad data values
are indicated by "-999.9". Summaries of data quality are available in
log files.

```
---------------------------------------------------------------
-- OBTAINING AND UNPACKING DATA SETS VIA FTP --

Here is an example of how to get one month's TOGA radiometric data
by using "anonymous ftp" to access our computer via the Internet.
Commands --> inside of arrows <-- are those which the user should type.
The sequence begins with using ftp on your computer to connect to our
computer at CSU. Then select the data file you want, get a copy
transfered to your computer, disconnect from CSU, and unpack the data.


$ --> ftp 129.82.107.109 <--
Connected to 129.82.107.109.
220 trueno FTP server (SunOS 4.1) ready.
Name (129.82.107.109): --> ftp <--
331 Guest login ok, send ident as password.
Password: --> (type in your full internet email address here) <--
230 Guest login ok, access restrictions apply.

ftp> --> cd toga <--
250 CWD command successful.

ftp> --> dir <--
200 PORT command successful.
150 ASCII data connection for /bin/ls (129.82.155.5,1034) (0 bytes).
total 81
-rw-rw-r--  1 366       11              104 May 24 16:54 00INDEX
-rw-rw-r--  1 366       11              368 May 24 16:58 00README
-rw-rw-r--  1 366       11            80239 Jun 10 16:06 DA9301.tar.Z
226 ASCII Transfer complete.
205 bytes received in 0.33 seconds (0.61 Kbytes/s)

ftp> --> bin <--
200 Type set to I.

ftp> --> get DA9301.tar.Z <--
200 PORT command successful.
150 ASCII data connection for DA9301.tar.Z (129.82.155.5,1035) (80239 bytes).
226 ASCII Transfer complete.
local: DA9301.tar.Z remote: DA9301.tar.Z
80599 bytes received in 13 seconds (6 Kbytes/s)

ftp> --> quit <--
221 Goodbye.

$ --> ls -l <--
total 99
-rw-r--r--  1 johndoe     80239 Jan 30 07:29 DA9301.tar.Z

$ --> uncompress -v DA9301.tar.Z <--
DA9301.tar.Z:  -- replaced with DA9301.tar
```

```
$ --> ls -l <--
total 356
-rw-r--r--   1 johndoe     335872 Jan 30 07:29 DA9301.tar

$ --> tar -tvf DA9301.tar <--
rw-rw-r-- 358/11    10080 May  5 10:55 1993 da930101.dat
rw-rw-r-- 358/11    10080 May  5 10:55 1993 da930102.dat
rw-rw-r-- 358/11    10080 May  5 10:55 1993 da930103.dat
 (...etc...)

$ --> tar -xf DA9301.tar da930115.dat <--
$ --> ls -l <--
total 366
-rw-r--r--   1 johndoe     335872 Jan 30 07:29 DA9301.tar
-rw-r--r--   1 johndoe      10080 May  5   1993 da930115.dat

$ --> more da930115.dat <--
 0.000  9.500  451.7  179.4   14.1  299.6
 0.083  9.583  448.5  190.0   15.3  299.4
 0.167  9.667  442.6  297.3   23.0  299.5
 0.250  9.750  442.7  311.5   23.9  299.7
 (...etc...)
```

APPENDIX C

Stephens et al. 1993,1994

ON MEASURING THE GREENHOUSE EFFECT OF EARTH

Graeme L. Stephens, Anthony Slingo[+], and Mark Webb[+]
Department of Atmospheric Science
Colorado State University
Fort Collins, CO 80523

1. INTRODUCTION

A balance between the amount of sunlight absorbed by the planet and the thermal radiation emitted to space is the primary control of the Earth's climate. Almost 70% of the solar energy reaching the earth is absorbed by the planet (e.g., Vonder Haar and Suomi, 1971), mainly at the surface. This warms the surface which then emits radiation towards space at longer infrared wavelengths. Radiatively active gases, such as water vapour and carbon dioxide, together with cloud particles, absorb radiation emitted from the surface. These constituents also re–emit infrared radiation but at temperatures which are lower than the surface temperature. This absorption and re–emission provides an effective mechanism for 'blocking' the surface emission from escaping to space and helps to maintain higher temperatures than would otherwise occur in the absence of the atmosphere. We call this the greenhouse effect (GE) of the atmosphere based on an analogy with the operation of an actual greenhouse, although this analogy is itself contentious (Bohren, 1987).

Knowledge of GE is fundamental to our understanding of how atmospheres evolved in the past (e.g., Ingersoll,1969) and, in particular, how the Earth's atmosphere is likely to evolve in the future. It is thus crucial that we develop a clear understanding of the different roles of gases and clouds in producing the greenhouse effect, especially given the possibility of feedbacks between the emission of radiation and the concentrations of these constituents. It is also crucial that we develop ways to exploit current satellite data, both to quantify the GE and to provide important tests of current global models.

The purpose of this paper is to outline an observational strategy to provide a quantitative assessment of the role of water vapour in establishing the GE. The strategy is intended to be simple enough that it can be used to test present–day general circulation

---

+ Hadley Centre for Climate Prediction and Research, Met. Office, Bracknell, UK

models (GCMs) of climate. The paper hints at the potential of spectral infrared emission measurements in unravelling various complex issues such as the effects of water vapour and its distribution on GE. The focus of this paper is directed toward understanding water vapour and its role on the clear sky greenhouse effect. Discussion of the important role of clouds on this effect (e.g., Stephens and Greenwald, 1991a) is omitted.

2. OBSERVATIONS OF VERTICALLY INTEGRATED WATER VAPOUR

We show below that the principal component of the Earth's greenhouse is atmospheric water vapour. Knowledge about how water vapour is distributed in the atmosphere, how it is transported by atmospheric motions and, perhaps most importantly of all, how it is transformed into clouds is therefore fundamental to understanding the Earth's greenhouse effect. Unfortunately, water vapour is notoriously difficult to measure. Routine observations from weather balloons are limited in both their spatial and temporal coverage, generally accurate to no better than about 10 % and biased to the larger landmasses of the planet. Satellite radiometric observations are near the point where they can provide the spatial coverage necessary to obtain global information about water vapour. Unfortunately, present satellite observing methods suffer their own limitations. Recent microwave observations, such as from the Special Sensor Microwave/Imager (SSM/I, Hollinger, 1987), provide perhaps the most unambiguous measurements of water vapour, but these are restricted to ocean regions and provide information only about the vertically integrated water path (this is known as the precipitable water and we refer to this quantity by the symbol w). Current retrieval methods based on spectral infrared measurements provide, in principle, a more complete global coverage, as well as offering some limited vertical information. However, these observations are biased to clear skies and the accuracy of infrared retrievals is still in question and a matter for current research.

The research described below combines 12 months of microwave water vapour observations (from March 1988 to February 1989, inclusive) with sea surface temperature data and Earth radiation budget data available from the Earth Radiation Budget Experiment (ERBE, Barkstrom, 1984). The microwave water vapour data are a crucial part of the analyses and Fig. 1 provides a broad perspective on the methods used to derive
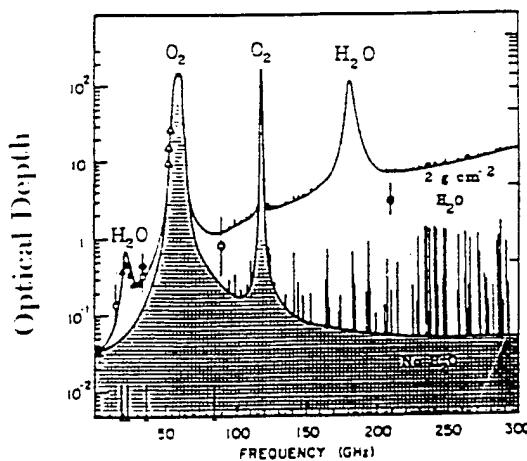
Fig. 1: The absorption spectrum of the atmosphere at microwave frequencies highlighting the location of the four SSM/ SSM/II channels at 19.35, 22.235, 37 and 85.5 GHz.

water vapour from microwave emission. The diagram presents the microwave emission spectrum (the function plotted is proportional to the microwave optical depth). The key feature of this spectrum for the data used in this study is the line centred at 22.235 GHz. The SSM/I provides measurements in and around this line and a number of retrieval methods have been developed to estimate w from these radiance measurements. The results of Jackson (1992) who compares four of these methods with selected radiosonde data are summarized in Table 1. The comparisons reveal that the microwave derived values of w agree with radiosonde values typically within 4 kgm^{-2}.

Figure 2 presents the mean of the 12 months analysed (labelled annual in the upper panel) and the 1989 January and 1988 July monthly mean values of w (middle and lower panels) obtained from the Greenwald et al. (1992) retrieval approach plotted respectively as a function of the corresponding mean sea surface temperatures (SSTs). The relationship between w and SST resembles one expected from simple thermodynamic principles (Stephens, 1990) and the general increase of w with increasing SST is an important and necessary condition for the existence of the water vapour feedback

(Stephens and Tjemkes, 1992). However, this relationship varies from season to season, as comparison of the January and July results in Fig. 2 reveal especially for SSTs less than about 290 K. Different relationships between w and SST for the summer and the winter hemispheres exist and are represented by the two branches in the scatter of points for both months considered. These results suggest that transport of water vapour in the middle latitudes during summer exceeds that during winter and this transport significantly enhances w in these regions thus altering the overall relationship between w and SST there. Independent observations of moisture transport that may be studied to confirm this interpretation are presently lacking although the climatologies described by Piexoto and Oort (1992) do not show any marked inter–hemispheric differences in seasonal moisture transports.

Table. 1: The root mean square (RMS), correlation (COR) and bias (BIS) of PWC (in kgm^{-2}) for the retrieval methods of Greenwald et al. (1992) (G), Alishouse et al. (1990) (A), Schluessel and Emery (1990) (SE) and Petty and Katsaros (1990) (PK).

NMC Radiosonde Statistics					
January 1989					
	G		AL	SE	PK
RMS	.25		4.41	4.52	4.96
COR	.925		.956	.947	.944
BIS	.21		.18	-.31	-.94
JULY 1989					
	G		AL	SE	PK
RMS	4.70		4.24	4.96	4.61
COR	.93		.940	.909	.927
BIS	.63		.16	-1.01	-.53

3.   A SIMPLE MODEL OF THE EARTH'S GREENHOUSE EFFECT

Before studying the Earth's GE and its relationship to water vapour in any detail, it is first necessary to introduce a quantity to define it. There are several ways to do this. Perhaps the simplest way is to use the difference between the mean radiating temperature of the planet and the surface temperature (Kondratyev and Moskalenko,
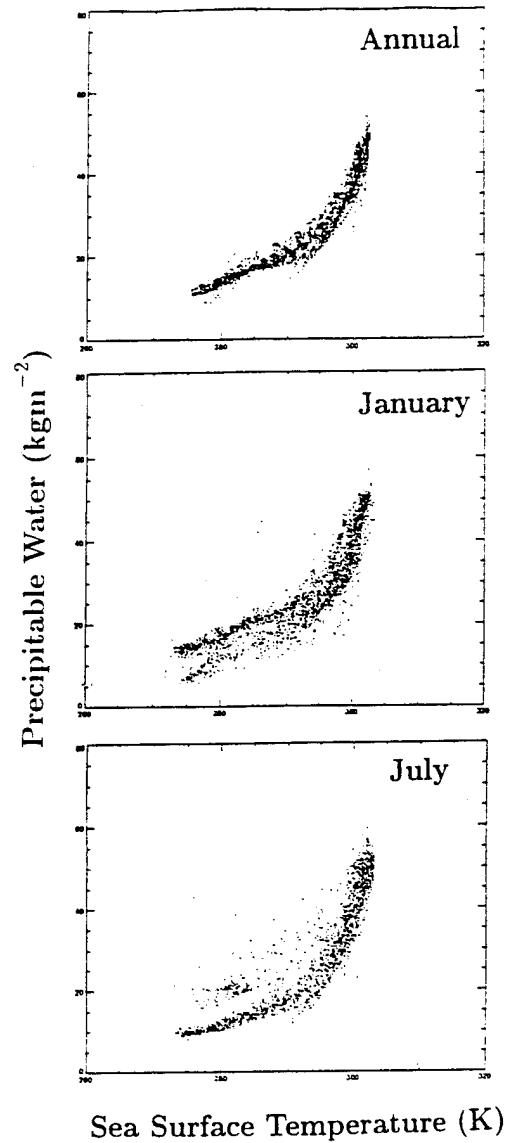
Fig. 2: The correlation of w with SST based on annual mean (upper panel), 1989 January mean (middle panel) and the 1988 July mean data (lower panel).

1984; Stephens and Tjemkes, 1992). However, the relationship between this temperature difference and the concentration of emitting species cannot be simply and conveniently defined. Raval and Ramanathan (1989) introduce the atmospheric absorption,

$$G_a = \sigma T_s^4 - F_\infty \tag{1}$$

as a convenient measure of GE where T_s is the sea surface temperature and F_∞ is the outgoing longwave radiation (OLR) at the top of the atmosphere. This definition, like that introduced below, applies only over the oceans where the surface emission may be taken to approximate closely a black body of temperature T_s. While we expect a general relationship between the absorption path of gas and G_a based on our physical understanding of molecular absorption, it is not clear *a priori* precisely what form this relationship should take. We now introduce a simple model of the greenhouse both as a means of defining the strength of the greenhouse and as a way of establishing such a relationship.

While the model adopted is described briefly in Stephens and Greenwald (1991b), a more detailed account is given here. The model of the greenhouse effect is based on simple considerations of radiative equilibrium. The radiative transfer equations for a non scattering atmosphere are

$$\mu \frac{dI(\tau,\mu)}{d\tau} = I(\tau,\mu) - B(T) \tag{2a}$$

$$-\mu \frac{dI(\tau,-\mu)}{d\tau} = I(\tau,-\mu) - B(T) \tag{2b}$$

where I is the intensity, $\mu = \cos\theta$ where θ is the angle of the beam from the zenith. The optical depth is defined as

$$\tau = \int_z^\infty k\rho_a dz \tag{3}$$

where k is the mass absorption coefficient, ρ_a is the density of the absorbing gas and z is the lowest end point of the path. Casting (2a) and (2b) into equations for upward ($F^\uparrow$) and downward ($F^\downarrow$) hemispheric fluxes leads to

$$\frac{dF^\uparrow}{d\tilde\tau} = F^\uparrow - \pi B, \tag{4a}$$

$$-\frac{dF^\downarrow}{d\tilde\tau} = F^\downarrow - \pi B, \tag{4b}$$

where

$$\tilde{\tau} = \frac{3}{2}\tau. \tag{5}$$

If we apply these equations to the broadband, then we can replace πB with σT^4 and treat $\tilde{\tau}$ as the greybody optical depth. It follows that in radiative equilibrium

$$F^{\uparrow}(\tilde{\tau} = 0) = Q_o(1 - \alpha) = F_{\infty}$$

where Q_o is the global–annual mean incoming solar radiation at the top of the atmosphere and α is the planetary albedo. It also follows that

$$F_{net} = F^{\uparrow}(\tilde{\tau}) - F^{\downarrow}(\tilde{\tau}) = const$$

which leads to the solution of (4a) and (4b) as

$$\sigma T_s^4 = \frac{F_{\infty}}{2}[2 + \tilde{\tau}_s] \tag{6a}$$

$$F_g^{\downarrow} = F^{\downarrow}(\tilde{\tau}_s) = \frac{F_{\infty}}{2}\tilde{\tau}_s \tag{6b}$$

at the surface where $\tau = \tau_s$ and $\tilde{\tau} = \tilde{\tau}_s$. This leads to a measure of the planetary greenhouse effect (e.g., Stephens and Greenwald, 1991b) as

$$\mathcal{G} = \frac{\sigma T_s^4}{F_{\infty}} = a + b\tau_s \tag{7}$$

where from (6a) and (5), a=1 and b=3/4. This definition identifies the grey body optical depth as the key parameter in defining the strength of the greenhouse. The spectral optical depth is a complex function of wavelength and several ways of spectrally averaging τ exist. The approach used here is one appropriate to the radiative equilibrium arguments introduced to arrive at (7) and follows from the following flux–mean mass absorption coefficient (Mihalas, 1978)

$$k_f = F_{\infty}^{-1} \int k_f F_{\infty,\lambda} d\lambda$$

The contribution to τ by water vapour, carbon dioxide and other minor greenhouse gases present in the Earth's atmosphere obtained using k_f in (3) is shown in Fig. 3. The spectral absorption data used to derive k_f are those tabulated by Rothman (1981). The total greybody optical depth derived from these data is $\tau = 3.9$ corresponding

to $w = 28$ kgm^{-2} which is close to the global mean values of w. The value $\tau = 3.9$ is larger than the value of the optical depth derived from (7). This highlights the ambiguity of the quantitative meaning of τ and to understand the value it is necessary to understand how it is derived. The advantage of the flux weighted value is that it allows us to estimate τ from spectral integration and thus the contributions by individual gases. These contributions are shown in Fig. 3 which clearly emphasizes the dominance of water vapour to the total greybody optical depth for the global mean conditions considered.
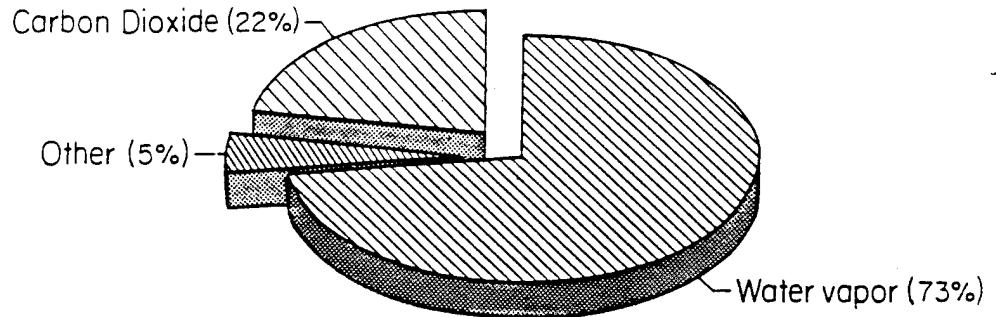

Fig. 3: A pie diagram showing the percentage of the grey body optical depth due to water vapour and other greenhouse gases in the Earth's atmosphere based on typical mean global concentrations of these gases.

4.   OBSERVATIONS OF THE GREENHOUSE EFFECT

Let us simply assume that in the case of water vapour, the flux-weighted mean optical depth is

$$\tau_f = \int k_f \rho_a dz \approx k_f w.$$

This assumption, together with (7) then leads to the following (e.g. Stephens and

Greenwald, 1991b)

$$\mathcal{G} = a + cw. \qquad (8)$$

The advantage of this relationship over others is that all factors in (8) are independently observed over the global oceans, primarily from satellites. For example, the SST can be obtained from independent analyses of blended ship, buoy and satellite data (e.g. Reynolds, 1984), the OLR available from ERBE data and w follow from microwave measurements described above. The annual, January and July monthly mean values of $\mathcal{G}$ derived in this way are plotted against corresponding mean values of w in Figure 4. The solid line through the scatter of annual mean points depicts the average of these points and the slope parameter $c = 0.00634$ $(\text{kgm}^{-2})^{-1}$ which is estimated via a least squares fit of the data (shown as the solid line in Fig 4) is a measure of how the greenhouse effect changes for given changes in w and is potentially important in analyses of water vapour feedback.

The analyses presented above provides a simple view of the influences of water vapour on the GE. However, a number of factors can potentially influence F_∞ independent of variations in w and thus introduce the scatter exhibited in Fig. 4. For example, increasing water vapour in the middle and upper troposphere only marginally affects w but can significantly alter F_∞. Variations in the vertical profile of temperature may also change F_∞ and thus $\mathcal{G}$. These two factors, we argue, are largely responsible for the observed scatter in the relationships shown.

If we suppose that w is a simple function of SST and express this function as (Stephens, 1990)

$$w = d \exp[r(T_s - 288)], \qquad (9)$$

then a simple combination of this expression with (8) yields

$$\mathcal{G} = a + cd \exp[r(T_s - 288)], \qquad (10)$$

and the sensitivity of $\mathcal{G}$ to SST follows as

$$g = \frac{d\mathcal{G}}{dT_s} = cdr \exp[r(T_s - 288)]. \qquad (11)$$

Figure 5 presents $\mathcal{G}$ as a function of SST and demonstrates a general increasing trend in $\mathcal{G}$ with increasing SST with a non–linear increase as the SST exceeds approximately
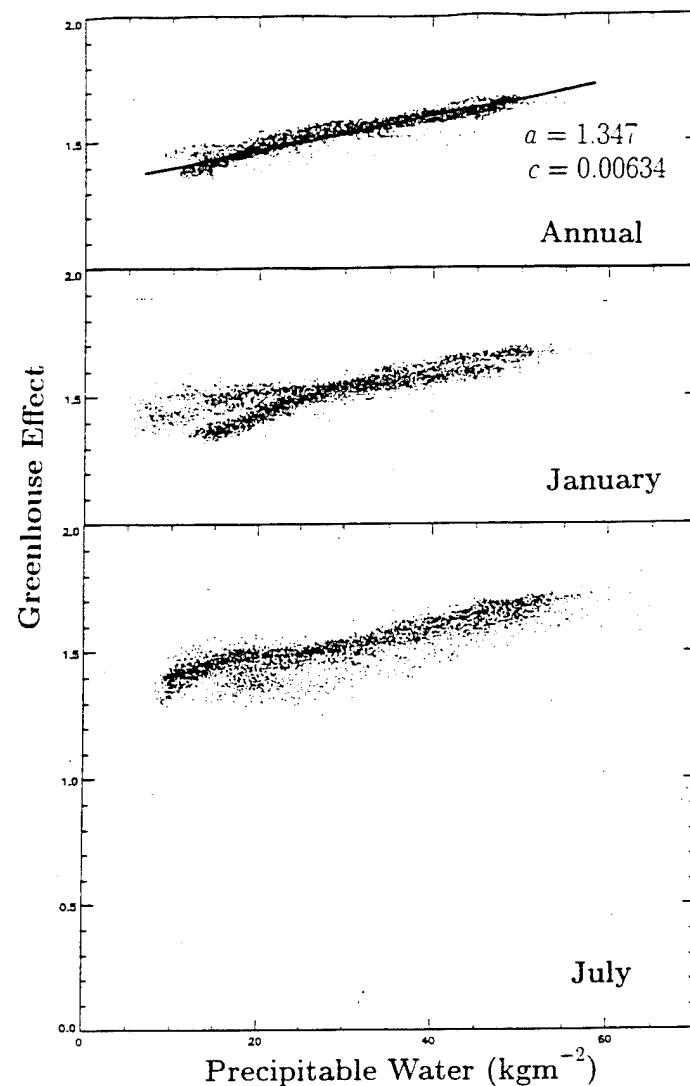
Fig. 4: The correlation of $\mathcal{G}$ with w based on annual mean (upper panel), 1989 January mean (middle panel) and the 1988 July mean data (lower panel). The unit of c is $(\text{kgm}^{-2})^{-1}$.

295 K. The relationship (11) and the results of Fig. 5 establish an important property of the Earth's greenhouse; that its sensitivity to changing SST is not uniform over the globe and is significantly greater over regions of warmer SST's. Ramanathan and Collins (1991) refer to this as a 'super–greenhouse' although Fig. 4 suggests that there is nothing special or 'super' in the relationship between $\mathcal{G}$ and w when $w > 30$ kgm^{-2}, which approximately corresponds to SST>295 K. The non–linear relationship observed in Fig. 5 arises primarily by thermodynamic controls on w and not on changes in the radiative transfer at these temperatures. The sensitivity parameter g highlights the relevance of the slope factor c and the r factor in the exponent of (11) in dictating the magnitude of this sensitivity.

5. ANALYSIS OF $\mathcal{G}$ FROM A SIMULATION SYSTEM–SAMSON

(a) Broadband simulations of the greenhouse effect

Slingo and Webb (1992) describe an analysis system (Simulation and Analysis of Measurements from Satellites using Operational aNalyses – SAMSON) which incorporates data from ECMWF operational analyses into a radiative transfer model to simulate the clear sky OLR and compare these simulations to matching ERBE clear sky data. Their analyses show how SAMSON simulations agree well with observations and point to two known systematic errors, a small overestimate in the clear sky ERBE fluxes (producing a bias in the ERBE clear sky OLR of approximately 5 Wm^{-2}, Harrison et al., 1990) together with a tendency for the ECMWF analyses to be too dry in the vicinity of the ITCZ and too moist in the subtropics (Liu et al., 1992)). Over most of the oceans, SAMSON simulations are within 5–10 Wm^{-2} of the ERBE data thus suggesting that it is possible to calculate clear sky OLR with an accuracy comparable to ERBE.

SAMSON is an ideal tool for understanding the effects of variations in the vertical distribution of water vapour and temperature on the kinds of relations shown in Fig. 4. We argue that these effects are largely responsible for the observed scatter in Fig. 4 and further analysis of SAMSON to verify this is a topic of ongoing research. Only preliminary and a limited number of results showing the application of SAMSON to the study of the clear sky greenhouse effect are presented here. These preliminary results are portrayed in Figs 6 and 7. Figure 6a contrasts the relationship between $\mathcal{G}$ and w
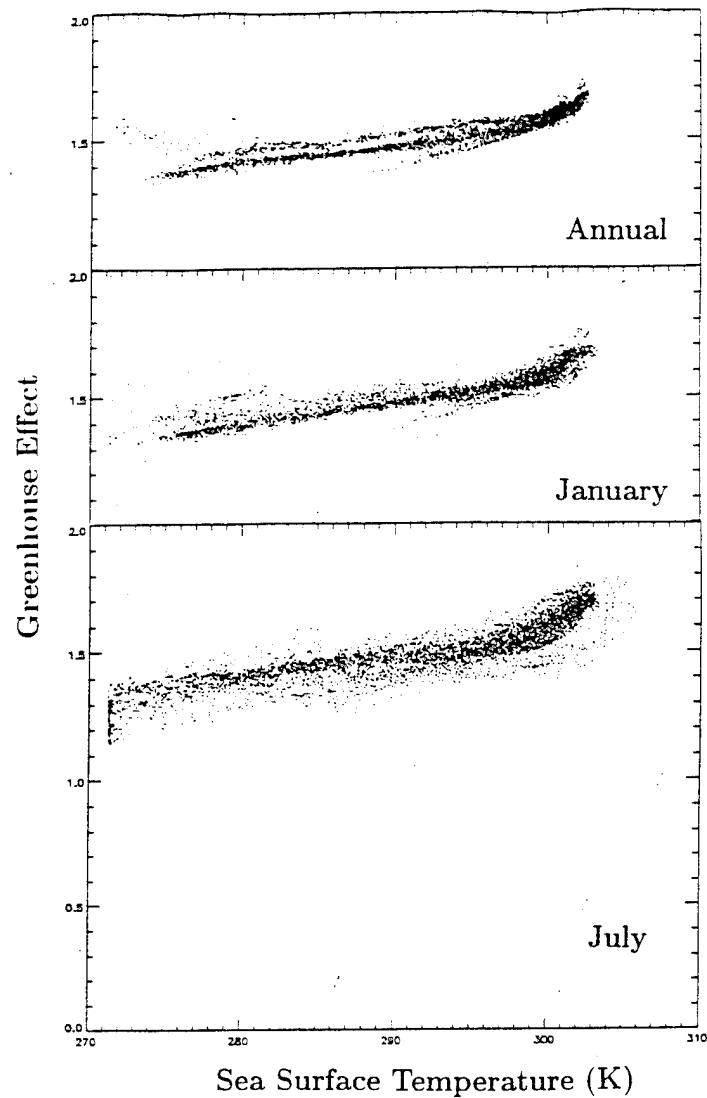
Fig. 5: The correlation of G with SST based on annual mean (upper panel), 1989 January mean (middle panel) and the 1988 July mean data (lower panel).
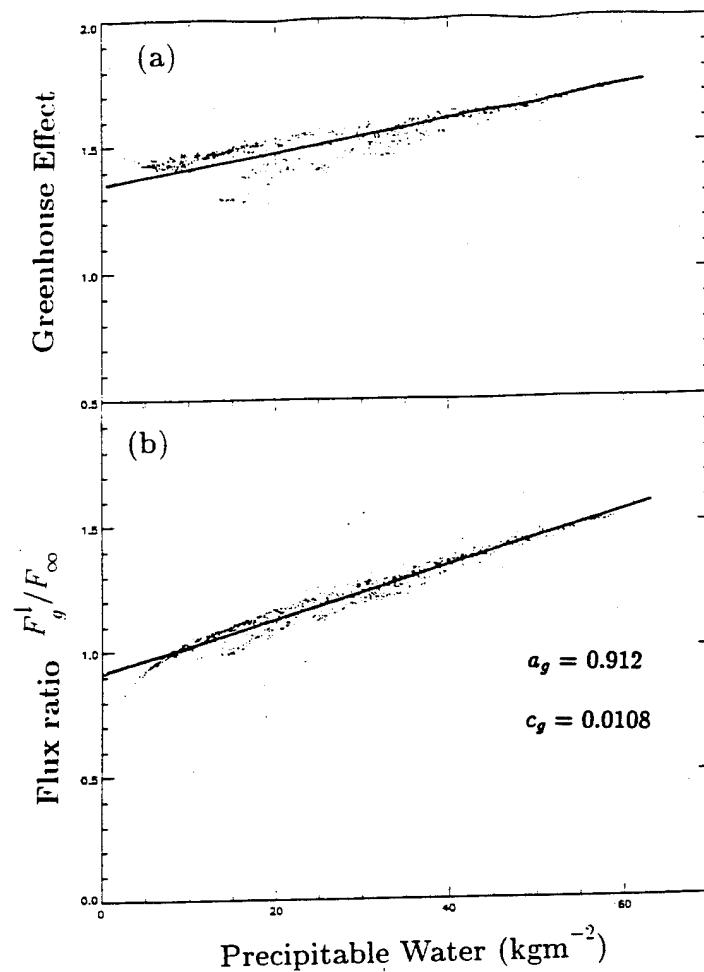
Fig. 6: (a) The correlation of $\mathcal{G}$ with w based on simulations of OLR using ECMWF July 1988 operational analysis for input into a radiative transfer model. The solid line is the fit to the annual mean relation given in Fig. 4. (b) As in (a) but for the ratio of fluxes $F^{\downarrow}/F_{\infty}$. The unit of c_g is $(\text{kgm}^{-2})^{-1}$.

derived from SAMSON simulations of July 1988 clear sky OLR and operational water vapour data (scattered points) and compares this result to the annual mean relationship represented by the solid line in Fig. 4.

If we adopt arguments equivalent to those used to obtain (10) then it also follows from (6b) that the ratio $F_g^\downarrow/F_\infty$ is a simple function of the precipitable water. This notion is confirmed by the results shown in Fig. 6b where the flux ratio is plotted as a function of w. Further insight into this relationship may also be obtained by studying the distributions of the July mean fluxes $F_g^\downarrow$, F_∞ and the flux ratio $F_g^\downarrow/F_\infty$ respectively shown in Fig. 7a,b and c. The distribution of $F_g^\downarrow$, especially in tropical latitudes, is more zonally symmetric than is the distribution of F_∞ despite the variations in w that exist in these latitudes (these variations occur as we move from the moist western Pacific, for instance, to the drier regions of the eastern Pacific– Jackson, 1992). These results are consistent with the impression that $F_g^\downarrow$ is influenced largely by near surface humidity and temperatures which are more zonally symmetric than are the variations in middle and upper tropospheric moisture which influence F_∞ . The rms error for simulations of $F_g^\downarrow$ based on a least squares linear fit of the ratio in Fig 6b (solid curve) and SAMSON values of both OLR and w is ±5 Wm^{-2}when compared to the direct SAMSON simulations of $F_g^\downarrow$. The shaded regions in Fig. 8 correspond to regions where the predicted values of $F_g^\downarrow$ differ by less than ±5 Wm^{-2}from the simulated fluxes and show how the predicted longwave flux to the ocean is mostly within this rms difference.

The results of Fig. 6b, and any predictive capability that follows from them, if confirmed with independent data, are quite remarkable and suggest that satellite observations of both w and clear sky F_∞ may provide a way of predicting the clear sky downward flux at the surface with an accuracy comparable to current measurements of these fluxes.

(b)   *Spectral simulations of the greenhouse effect*

Another advantage of SAMSON is that it can also be used to study spectral variations in GE. This information not only reinforces understanding derived from the broadband results, but also identifies spectral regions where GE is most sensitive to changes in either w or SST and perhaps relevant to monitoring long term changes in GE. SAMSON was used with the July 1988 ECMWF analysis data as input to simulate spectral inten-
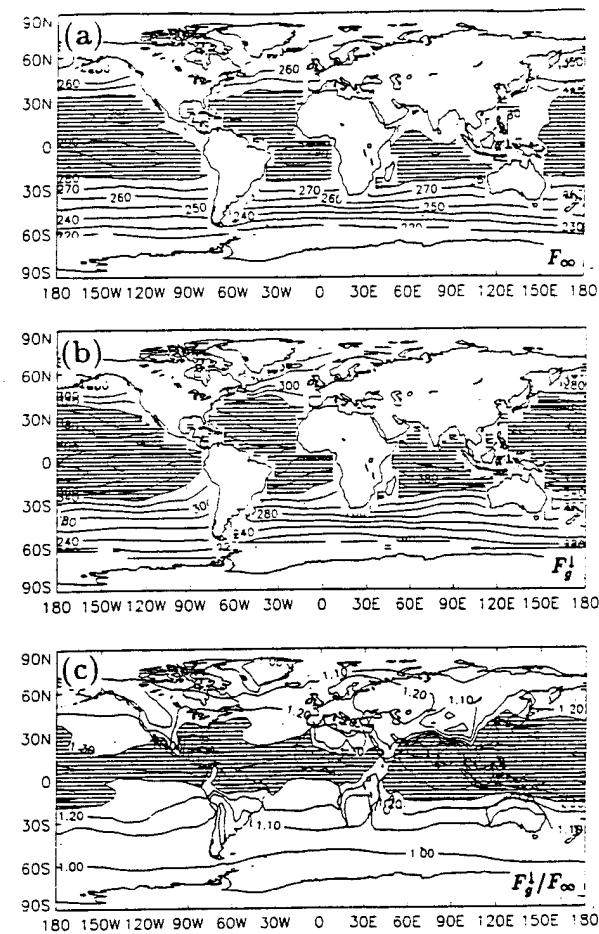
Fig. 7: (a) The distribution of simulated OLR F_∞ (in Wm^{-2}) using ECMWF July 1988 operational analysis for input into a radiative transfer model. **(b)** As in (a) but for the downward longwave flux $F_g^\downarrow$ at the surface and **(c)** the ratio of fluxes $F_g^\downarrow/F_\infty$.
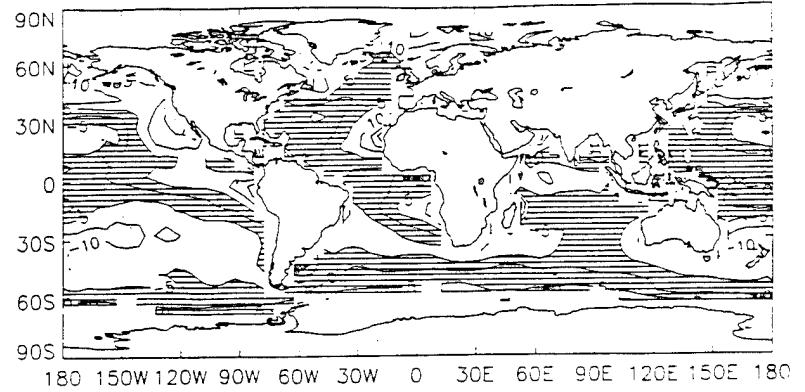
Fig. 8: The difference between the predicted values of $F_g^\downarrow$ at the
surface (derived from the least squares fit of the ratio $F_g^\downarrow/F_\infty$,
the OLR and w) and simulated values of $F^\downarrow$ (contours in units of
Wm^{-2}). Shaded areas denote differences of $\pm 5\ Wm^{-2}$.

sities corresponding to channels 10 (8.2 μm), 11 (7.3 μm) and channel 12 (6.3 μm) of
HIRS. The July mean simulations of channel 12 brightness temperature (derived from
calculated spectral nadir radiances) are contrasted against the July averages of HIRS
channels 11 and 12 brightness temperatures (Wu *et al.*, 1992) in Fig. 9a,b,c and d. The
distribution in the simulated temperatures resembles the measured brightness temper-
atures and showing regions (shaded in Fig. 9b and d) that are associated with large
scale subsidence (Wu et al., 1992). The differences between the simulated and observed
brightness temperatures exhibit a well known bias and no attempt has been made to
tune the simulations to the observations by accounting for the filter response functions
and other factors. The detailed differences between the observed temperatures of this
channel and simulated temperatures using a TOVS simulation program which are ap-
propriately tuned against observations are discussed more fully by Eyre et al. (1992,
this volume).

Spectral flux simulations of channels 10, 11 and 12 were analysed to examine the
behaviour of the spectral greenhouse parameter and its variations with w. We refer
to these spectral quantities in terms of the matching HIRS channel number. The GE
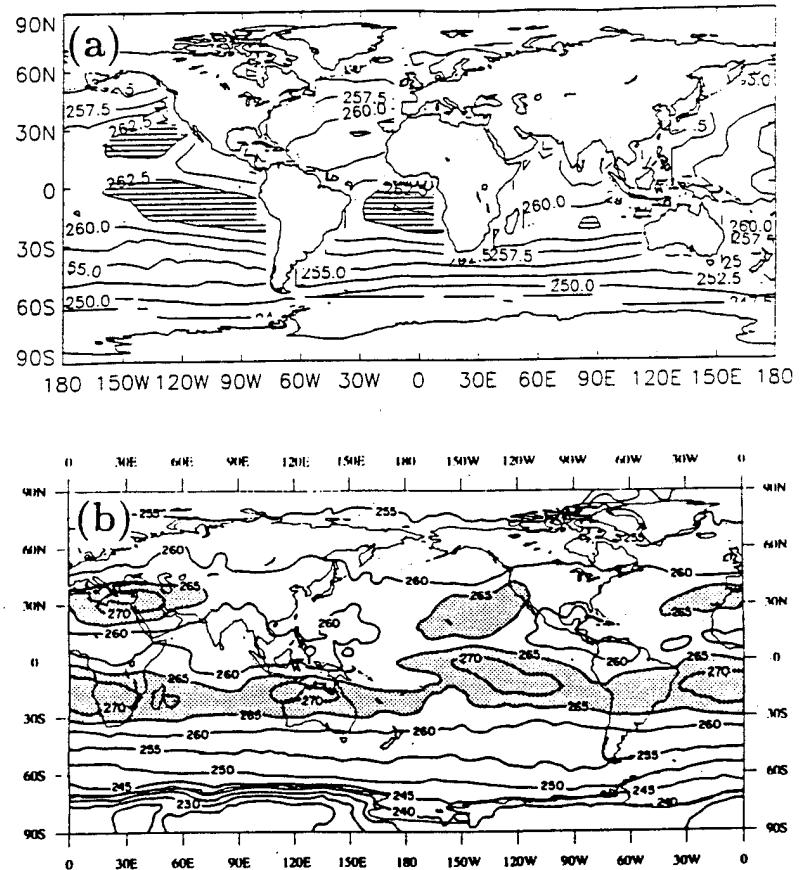
Fig. 9: (a) SAMSON simulations of the HIRS channel 11 brightness temperatures based on ECMWF analyses of July 1988. (b) Observed channel 11 brightness temperatures obtained from the climatological analyses of Wu et al., (1992).
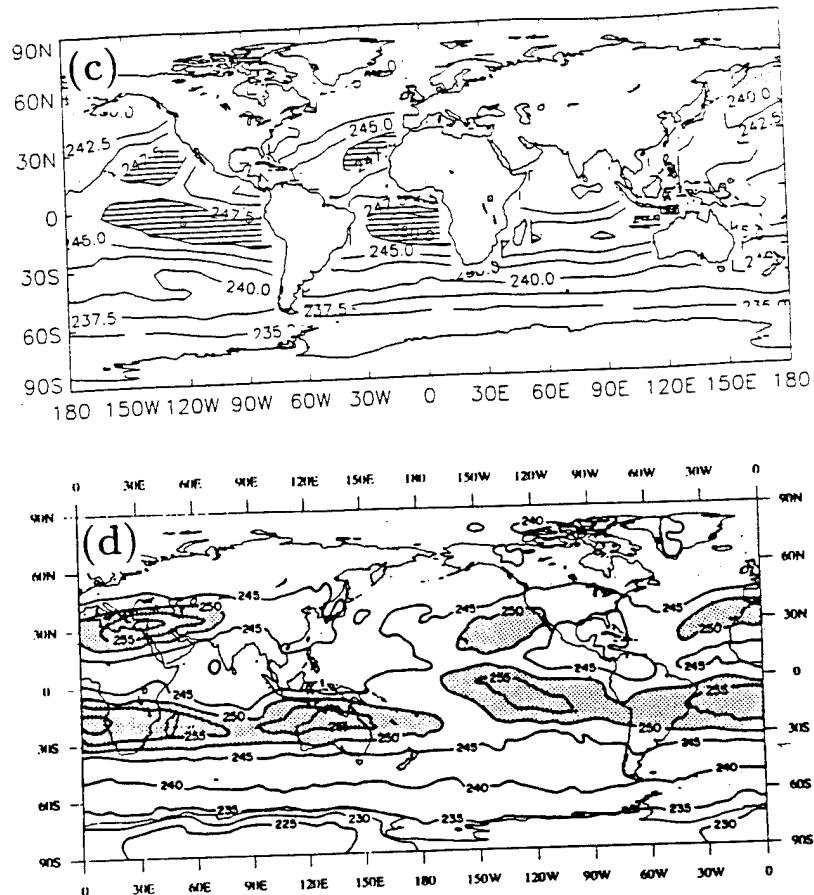
Fig. 9: (c) SAMSON simulations of the HIRS channel 12 brightness temperatures based on ECMWF analyses of July 1988. (d) Observed channel 12 brightness temperatures obtained from the climatological analyses of Wu et al., (1992).

parameters, $\mathcal{G}_{10,11,12}$ are presented as functions of w in Fig. 10 together with an estimate of the slope parameter. A number of aspects of these simulated relationships warrant comment. The relationship between $\mathcal{G}$ and w becomes less distinct as the wavelength varies from the more transparent channel 10 to the more opaque wavelengths of channel 12. The spectral OLR of the latter channel is influenced significantly by middle and upper tropospheric moisture rather than by w as well as by changes in temperature profile at these levels in the atmosphere. The relationship between $\mathcal{G}_{10}$ and w resembles the broadband relationship shown in Figs 4 as previously predicted by Stephens and Greenwald (1991b). Another point to note is that the slope factor c derived for each of the simulated channels varies by an order of magnitude from channel 10 to channel 12. The parameter c_{10} closely matches the broadband sensitivity expressed in Fig. 4. The more opaque channels 11 and 12 are more sensitive to changes in water vapour although there is considerably more scatter to these relationships. These results are at least consistent with the idea that the variations of vertical temperature and moisture tend to account for the observed scatter in the broadband results. A more detailed analyses of these simulations and others is in progress.

6. SUMMARY

This paper outlines an observational strategy that provides both a quantitative assessment of the role of water vapour in establishing the clear sky GE on Earth yet is simple enough to be used to test simulations of the GE by present day general circulation models (GCM) of climate. The virtue of this strategy is that it uses present day satellite observations to make this assessment.

We can conclude from the research presented in this paper that:

(i) under global mean conditions, approximately 75 % of the strength of the greenhouse, which is introduced in this paper in terms of the greybody optical depth of the atmosphere, is due to water vapour. We show how this contribution can be measured in terms of the ratio of the emission from the sea surface and the outgoing longwave radiation and explore the relation between this ratio and the integrated column water vapour amount w using satellite observations of w and outgoing longwave radiation.

(ii) We extend the analysis of the global greenhouse to consider the longwave flux
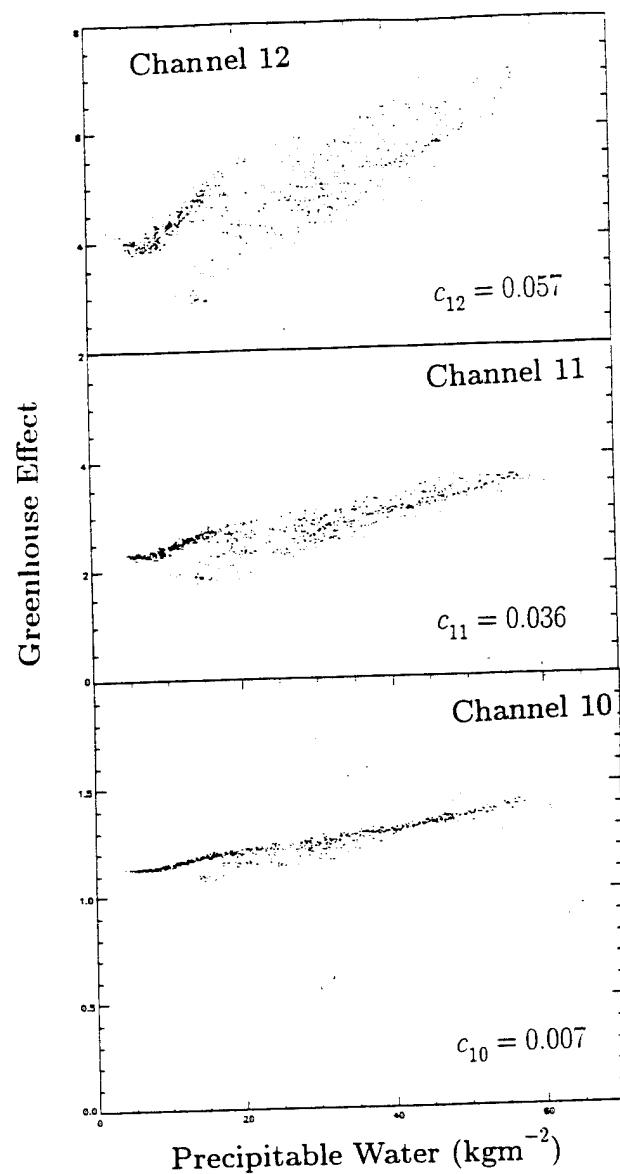
Fig. 10: Simulated $\mathcal{G}_{10,11,12}$ as a function of w together with slope parameters expressed in units of $(kgm^{-2})^{-1}$.

emitted by the atmosphere to the surface. Using equivalent arguments, we suggest a simple linear relationship between the ratio of broadband fluxes $F_g^{\downarrow}/F_{\infty}$ and w and demonstrate this relationship with simulations. Based on the single month of analyses, this relation, together with measured OLR and w offers a way of predicting monthly mean clear sky fluxes $F_g^{\downarrow}$ within ± 5 Wm^{-2} of the simulated fluxes.

(iii) We provide a preliminary glimpse at the spectral contributions to the GE as a first stage in unravelling various complex issues such the effects of vertical variations in water vapour and temperature on the observed relationships mentioned above. Based on simulations of fluxes in spectral regions characteristic of selected HIRS channels, we are able to show the close similarity between the observed broadband relationships and those of channel 10 (centred on 8.2 μm). We also show how the relationship between $\mathcal{G}$ and w begins to break down in the more opaque regions, characterized by channels 11 and 12.

(iv) Because of the non-linear relation between w and sea surface temperature, the clear-sky greenhouse effect is also non-linearly related to SST. The change in the GE with changing SST, which we refer to as the greenhouse–SST sensitivity, is shown to increase with SST also in a non-linear way with the greatest sensitivity occurring over the warmest oceans. This is in direct contrast to the simple analysis of water vapour feedback which is often described in terms of the Budyko sensitivity parameter B (e.g. North et al., 1981) which is taken to be a global quantity.

The feedback between surface temperature and water vapour is thought to contribute substantially to the projected global warming induced by rising levels of carbon dioxide. The sensitivity parameter g introduced in this paper and which can readily be estimated from available satellite data should not be misconstrued as a measure of feedback between $\mathcal{G}$ and the SST. We note that many factors other than SST influence $\mathcal{G}$ and thus g. Among these factors are the vertical profiles of water vapour and temperature. The parameters used to estimate g in this study correspond to a set of conditions which do not remain fixed but vary in association with changing SST. A fundamental issue, and a topic of a further study, concerns the robustness of relationships shown here and whether the same sensitivities derive from climate states which are different from the present day state observed in this study.

7. ACKNOWLEDGMENTS

8. REFERENCES

Alishouse JC, Synder SA, Vongsathorn J, Ferraro RR, (1990) Determination of oceanic total precipitable water from the SSM/I. IEE Trans Geosci Remote Sensing 28:811-816

Barkstrom BR (1984) The Earth Radiation Budget Experiment (ERBE). Bull Amer Meteorol Soc 65:1170-1185

Bohren C (1987) Clouds in a glass of beer. In: Wiley & Sons, New York, p 187 (discussion on page 83)

Eyre JR, Andersson E, McNally AP (to be published) Direct Use of Satellite Sounding Radiances in Numerical Weather Prediction. In: Chedin A, Chahine, MT (eds) High Spectral Resolution Infrared Remote Sensing for Earth's Weather and Climate Studies. NATO ASI Series, D. Reidel Publishing Company Dordrecht Boston Lancaster Tokyo

Greenwald TJ, Stephens GL, Vonder Haar TH, Jackson DL (to be published) A physical retrieval of cloud liquid water over the global oceans using SSM/I observations. J Geophys Res

Harrison EF, Minnis P, Barkstrom BR, Ramanathan V, Cess RD, Gibson GG (1990) Seasonal variation of cloud radiative forcing derived from the Earth Radiation Budget Experiment. J Geophys Res 95:18687-18703

Hollinger J, Lo R, Poe C, Savage R, Pierce J (1987) Special Sensor microwave/imager user's guide. Report Nav Res Lab Washington DC

Ingersoll AP (1969) The runaway greenhouse effect: A history of water on Venus. J Atmos Sci 26:1191-1198

Jackson DL (1992) On the role of SSM/I derived precipitable water over the globe and tropical Pacific. M Sc thesis, Colo State Uni, Ft. Collins, CO

Kondratyev KY, Moskalenko NI (1984) The role of carbon dioxide and other minor gaseous components and aerosols in the radiation budget. In: Houghton JT (ed) The Global Climate, p 225-232

Liu WT, Wang T, Wentz F (1992) Precipitable water and surface humidity over the global oceans from SSM/I and ECMWF. J Geophys Res 97:2251-2264

Mihalas D (1978) Stellar Atmospheres. In: Freeman WF (ed) Freeman and Co 2nd edn. Freeman and Co, San Franscisco p 569

North GR, Cahalan RF, Coakley JA (1981) Energy balance climate models. Rev Geophys Space Phys 19:91-121

Petty GW, Katsaros K (1990) New geophysical algorithm for the special sensor microwave imager. 5th Conf on Sat Met and Oceanog Sept. 3-7 London Eng

Piexoto JP, Oort A (1992) Physics of Climate. American Inst of Phys, New York, p 520

Ramanathan V, Collins W (1991)Thermodynamic regulation of ocean warming by cirrus clouds deduced from observations of the 1987 El Nino. Nature 351:27-32

Raval A, RamanathanV (1989) Observational determination of the greenhouse effect. Nature 342:758-761

Reynolds RW (1988) A real-time global sea surface temperature analysis. J Climate 1: 75-86

Rothman LS (1981) AFGL atmospheric absorption line parameters compilation: 1980 version. Appl Opt 20:791-795

Schluessel P, Emery WJ (1990) Atmospheric water vapour over oceans from SSM/I measurements. Int J Remote Sensing 11:753-766

Slingo A, Webb MJ (to be published) Simulation of clear-sky outgoing longwave radiation over the oceans using operational analyses. Q J Roy Meteorol Soc

Stephens GL (1990) On the relationship between water vapour over the oceans and sea surface temperature. J Climate 3:634-645

Stephens GL, Greenwald TJ (1991a) Observations of the Earth's Radiation Budget in Relation to Atmospheric Hydrology. Part II: Cloud Effects and Cloud Feedback. J Geophys Res 96:15,325-15,340

Stephens G L, Greenwald TJ (1991b) Observations of the Earth's Radiation Budget in Relation to Atmospheric Hydrology Part I: Clear Sky Greenhouse Effect and Water vapour Feedback. J Geophys Res 96:15,311-15,324

Stephens GL, Tjemkes S (to be published) Water vapour and its role in the Earth's greenhouse. Australian J Phys

Vonder Haar TH, Suomi V (1971) Measurements of the earth's radiation budget from satellite during a five-year period. Part I: Extended time and space means. J Atmos Sci 28:305-314

Wu X, Bates JJ, Khalsa SJS (in preparation) Upper tropospheric water vapour climatology derived from TOVS data

Observations of the Earth's Radiation Budget in relation to atmospheric hydrology
4. Atmospheric column radiative cooling over the world's oceans

Graeme L. Stephens,[1] Anthony Slingo,[2] Mark J. Webb,[2] Peter J. Minnett,[3] Peter H. Daum,[3] Lawrence Kleinman,[3] Ian Wittmeyer,[1] and David A. Randall[1]

Abstract. This paper introduces a simple method for deriving climatological values of the longwave flux emitted from the clear sky atmosphere to the ice-free ocean surface. Simulations of the clear sky longwave fluxes to space and to the surface are employed in this study to assist in the development of this flux retrieval which requires monthly averaged column-integrated water vapor w and the clear sky top–of–atmosphere (TOA) outgoing longwave flux (both available from satellite measurements). It is shown using both theory and data from simulations how the ratio of the surface to TOA flux is a simple function of w and a validation of the simple relationship is presented based on a limited set of surface flux measurements. The rms difference between the retrieved surface fluxes and the simulated surface fluxes is approximately 6 W m^{-2}. The clear sky column cooling rate of the atmosphere is derived from the Earth Radiation Budget Experiment (ERBE) values of the clear sky TOA flux and the surface flux retrieved using Special Scanning Microwave Imager (SSM/I) measurements of w together with ERBE clear sky fluxes. The relationship between this column cooling rate, w, and the sea surface temperature (SST) is explored and it is shown how the cooling rate systematically increases as both w and SST increase. The uncertainty implied in these estimates of cooling are approximately ± 0.2 K d^{-1}. The effects of clouds on this longwave cooling are also explored in a limited way by placing bounds on the possible impact of clouds on the column cooling rate based on certain assumptions about the effect of clouds on the longwave flux to the surface. While a more global assessment of the cloud effect must await use of new satellite data that will allow us to estimate the contributions by clouds to these surface fluxes, it is shown in this paper how the longwave effects of clouds in a moist atmosphere where the column water vapor exceeds approximately 30 kg m^{-2} may be estimated from presently available satellite data with an uncertainty estimated to be approximately 0.2 K d^{-1}. Based on an approach described in this paper, we show how clouds in these relatively moist regions decrease the column cooling by almost 50% of the clear sky values and the existence of significant longitudinal gradients in column radiative heating across the equatorial and subtropical Pacific Ocean.

1. Introduction

The energy balance of the Earth, the distribution of energy in space, and its variation in time are fundamental characteristics of the Earth's climate system. It

[1] Department of Atmospheric Science, Colorado State University, Ft. Collins, Colorado.

[2] Hadley Center for Climate Prediction and Research, Bracknell, England.

[3] Brookhaven National Laboratory, Upton, New York.

is crucial to understand how this energy balance is altered in response to increased concentrations of greenhouse gases to understand and ultimately predict any impending global climate change. Unfortunately, quantitative estimates of the individual components of this energy budget, even in its most rudimentary annual and global–mean form, are subject to large uncertainties since many of the key fluxes of energy are yet to be measured over the globe. For instance, the fluxes of energy to and from the surface, at least on the global scale, are primarily derived from model calculations or estimated from empirical formulae and must be considered highly uncertain [e.g., *Randall et al.*, 1992; *Gupta et al.*, 1992]. Methods using satellite observations for retrieving these fluxes, with the exception of the solar flux to the surface

[e.g., *Schmetz*, 1989; *Pinker and Laszlo*, 1992; *Cess et al.*, 1991], remain largely undeveloped. Despite this situation, important but limited advances to our view of this global energy balance have emerged from satellite measurements of the radiative fluxes at the top of the atmosphere. These advances began in the late 1960s and continue into the present through the Earth Radiation Budget Experiment (ERBE), [*House et al.*, 1986].

This paper is the final in a series [*Stephens and Greenwald*, 1991a,b, hereafter referred to as parts 1 and 2; *Stephens et al.*, 1993, hereafter part 3], which seek to explore new uses of global satellite data to study relationships between certain components of the energy budget and the hydrological cycle of the climate system. The motivation, in part, is to develop useful diagnostic tests of current global climate models and, in part, to study rudimentary relationships between radiation and the atmospheric branch of the Earth's hydrological cycle. The main aim of this paper is to introduce a simple method for deriving climatological values of the longwave flux emitted from the clear sky atmosphere to the surface (hereafter denoted as F_g) and in so doing explore the connection between the longwave radiation budget and the water vapor content of the atmosphere. The flux F_g is one of the principal drivers of the planet's greenhouse effect. It is the emission of infrared radiation from the atmosphere to the surface that maintains the mean surface temperature of the Earth (approximately 288 K) above the mean effective temperature of the planet (approximately 255 K). It is also the amplification of this flux due to increased concentrations of water vapor, driven by increased concentrations of other greenhouse gases, that is thought to establish the water vapor feedback [*Manabe and Wetherald*, 1967].

We currently estimate that the globally averaged atmosphere constantly loses energy by radiation at a rate of approximately 100 W m^{-2} [*Ramanathan et al.*, 1989]. It is a related goal of this study to estimate the clear sky longwave contribution to this loss as well as the longwave contributions by clouds in selected regions of the globe. The loss of radiative energy by the atmosphere is compensated by energy transfer from the surface via convective and turbulent transfer processes. The global balance achieved in the atmosphere through the combination of the radiative and nonradiative processes is generally referred to as a radiative–convective equilibrium. The major contributors to this equilibrium is the flux of heat supplied by latent heating, associated with precipitation in the atmosphere, and the loss of longwave radiant energy by the atmosphere. It is common to express this loss of radiant energy as the rate of cooling of the atmospheric column. Global scale changes in this cooling imply compensating changes in latent heating and thus changes in the Earth's hydrological cycle. It is appropriate then to consider this cooling as a fundamental measure of the activity of the Earth's greenhouse effect and in turn an indirect measure of the activity of the hydrological cycle in heating the atmosphere.

Section 2 offers a brief account of the data used in the present study, and section 3 introduces results from the simulation system of *Slingo and Webb* [1992], which are subsequently used in section 4 to develop a new diagnostic method for the retrieval from satellite data of F_g. Results of this retrieval approach and a limited validation of the method are presented in sections 4 and 5 respectively. Once the clear sky longwave flux to the surface is known, the clear sky atmospheric longwave cooling is then determined in the manner described in section 6, where the correlation between the magnitude of this cooling and the column water vapor is also explored.

It remains, however, a considerable challenge to establish meaningful ways of using present-day space measurements to estimate the contributions by clouds to the surface longwave fluxes and therefore to the column heating rates. Despite these unmet challenges, we demonstrate in section 6 of this paper how upper and lower bounds can be placed on these cloud effects and furthermore demonstrate how the longwave effects of clouds in a moist atmosphere, where the column water vapor exceeds approximately 30 kg m^{-2}, may be estimated from presently available satellite data with an accuracy of approximately 0.2 K d^{-1}. Based on the approach described in section 6, we show how clouds in these relatively moist regions decrease the column cooling by almost 50 % of the clear sky values and we infer the presence of significant gradients of column radiative heating across the equatorial Pacific.

2. Data Sources

The main sources of the global data analyzed in this study are those described and used previously in part 3. These data include the ERBE fluxes, the column water vapor retrieved by *Greenwald et al.* [1993] based on passive microwave measurements obtained from the Defense Meteorological Satellite Program's (DMSP) SSM/I instrument [*Hollinger et al.*, 1987], and the sea surface temperature (SST) data of *Reynolds* [1988]. The results from the Colorado State University General Circulation Model (GCM) defined in part 3 are also utilized but more sparingly in this study.

An important new source of data for this study is the simulation of the clear sky longwave radiative fluxes obtained from the system of *Slingo and Webb* [1992] for the simulation and analysis of measurements from satellites using operational analyses (SAMSON). These simulations use initialized analyses from the operational archive at the European Centre for Medium-Range Weather Forecasts (ECMWF) but with the column water vapor constrained to the SSM/I values, as described by *Webb et al.* [1993]. Temperature and specific humidity data on 19 model levels were directly incorporated into the simulations along with analyzed surface pressure.

SAMSON is constructed around a high spectral resolution radiative transfer model [*Shine*, 1991] that incorporates the ECMWF analyses from the operational archive. The accuracy of the radiation model employed

by SAMSON was checked using a single-column version applied to Intercomparison of Radiation Codes for Climate Models (ICRCCM) test profiles [*Ellingson et al.*, 1991]. Calculations of clear sky outgoing longwave radiation (hereafter represented as F_∞) for five standard atmospheres with effects of water vapor, carbon dioxide, and ozone differed from line–by–line calculations of F_∞ by approximately 1 W m^{-2}, suggesting excellent agreement with these reference calculations [*Slingo and Webb*, 1992]. Comparison of clear sky values of F_g depends to a small extent on the specific details of how the continuum absorption is dealt with in the model. The treatment of the continuum is described by *Shine* [1991] and is based on the far-wing treatment of *Clough et al.* [1986]. Variations of the treatment of this continuum can introduce uncertainties in calculations of the surface flux up to 10 W m^{-2} [*Ellingson et al.*, 1991]. SAMSON simulations of F_g agreed with reference ICRCCM calculations of this flux within 3 W m^{-2}.

For the simulations shown below, the effects of minor trace gases of nitrous oxide, methane, CFC11, and CFC12 were included in addition to water vapor, carbon dioxide and ozone, and the volume mixing ratios of these gases, which are assumed to be uniformly mixed in the atmosphere, are given by *Slingo and Webb* [1992].

The research described in this paper also introduces surface radiation flux data collected during two oceanographic research cruises by the R/V *Alliance* in the Mediterranean Sea off Crete in June 1990 and off Corsica in the fall of 1991 and by the USCGC *Polar Sea* cruise in the Arctic Sea in July and August 1992 [*Minnett*, 1992, 1993; *NEWATER*, 1993]. For the present purposes the relevant data from these cruises consist of measurements of downwelling infrared fluxes at the surface measured by Eppley pyrgeometers mounted on a mast at 16 m above sea level, observed cloud amounts, and concurrent radiosonde data. During the 1990 Mediterranean experiment the ship was overflown on four occasions by the U.K. meteorological research flight C–130 which carried a precision pyrgeometer. The differences between the ship measurements and the aircraft measurements were 7,18,-4, and 4 W m^{-2} which represents 2-5% range of differences from the measured flux.

Surface radiation budget data also collected in support of the Tropical Ocean Global Atmosphere (TOGA) Coupled Ocean Atmosphere Response Experiment (COARE) at four island sites; the atoll of Majuro in the Republic of the Marshall Islands at 7 ° 05' N latitude and 171° 23' E longitude and the islands of Pohnepi and Chuuk in the Federated States of Micronesia at 6° 58' N latitude and 158° 13' E longitude and 7° 27' N latitude and 151° 50' E longitude and the island site of Kavieng 2° 30'S 150° 48'E. In addition to these island sites a site located at Darwin 12° 25'S.130° 51'E, Australia is also used in this study. The details of the TOGA data, its quality control, calibration, and its accessibility will be described in a forthcoming paper by the principal author and is described in the report of *Cornwall et al.* [1993].

3. SAMSON Simulations

Simulations of the monthly mean clear sky fluxes over the ice-free oceans were carried out for the period March 1988 to February 1989 which is also a period for which both ERBE and SSM/I observations are available. As in the original study of *Slingo and Webb* [1992], these simulations apply to a horizontal resolution of 5°. The radiation code was applied to each daily analyses (a mean of four 6 hourly analysis for each day) and then averaged to produce the monthly mean flux distributions which are used in the analyses described below. Both *Slingo and Webb* [1992] and *Webb et al.* [1993] discuss the differences between the simulated fluxes from SAMSON and the clear sky values of F_∞ obtained from ERBE. Figure 1 presents examples of scatter diagrams of the SAMSON F_∞ versus the ERBE F_∞ for April, July, and September 1988 and January 1989 to highlight some gross features of these comparisons. For instance, a slight positive bias of 3-5 W m^{-2} exists between the SAMSON and ERBE fluxes, a bias similar in both sign and magnitude to that of the ERBE clear sky flux data [*Harrison et al.*, 1988]. As *Webb et al.* [1993] show, there are regions (not shown) where the differences between the simulated fluxes and the ERBE-derived fluxes exceed this small bias, such as over the areas of marine boundary layer clouds off the west coasts of the major continents where differences may be as large as 10 W m^{-2}. These areas can be traced to biases in the ECMWF water vapor data [e.g., *Liu et al.*, 1992; *Stephens et al.*, 1994].

Except for these particular regions the simulations of clear sky F_∞ from SAMSON generally agree with ERBE estimates of this flux to within 5-10 W m^{-2}, which is considered to be of the same order of uncertainty of the latter. There are also no a priori reasons to expect the SAMSON simulations of clear sky F_g to be grossly in error although it is noted above how the specific details of how the continuum absorption is modeled may introduce an uncertainty of the order of 10 W m^{-2}. Bearing this possibility in mind, simulated distributions of F_g over the ice-free oceans are presented in Plates 1a and 1b in the form of the surface net flux (i.e., $\sigma T_s^4 - F_g$). The maps of the surface net flux shown in Plates 1c and 1d are those derived by the approach described below and are presented here for comparison. The smallest net fluxes of around 40-50 W m^{-2} occur in the tropical convergence zones over the Pacific and Indian Oceans and in the Northwest Pacific in July. A significant annual variation close to the northern continents also appears to exist which is associated with changes in the atmospheric circulation associated with the summer and winter monsoons. There is also a close correspondence in the tropics between column-integrated water vapor w (discussed later in relation to Plates 2c and 2d) and the surface net longwave fluxes shown in Plate 1. This arises because atmospheric temperatures are relatively uniform in the tropics, so the net flux is mainly determined by the lower tropospheric humidities, which also dominate w [e.g., *Stephens*, 1990].
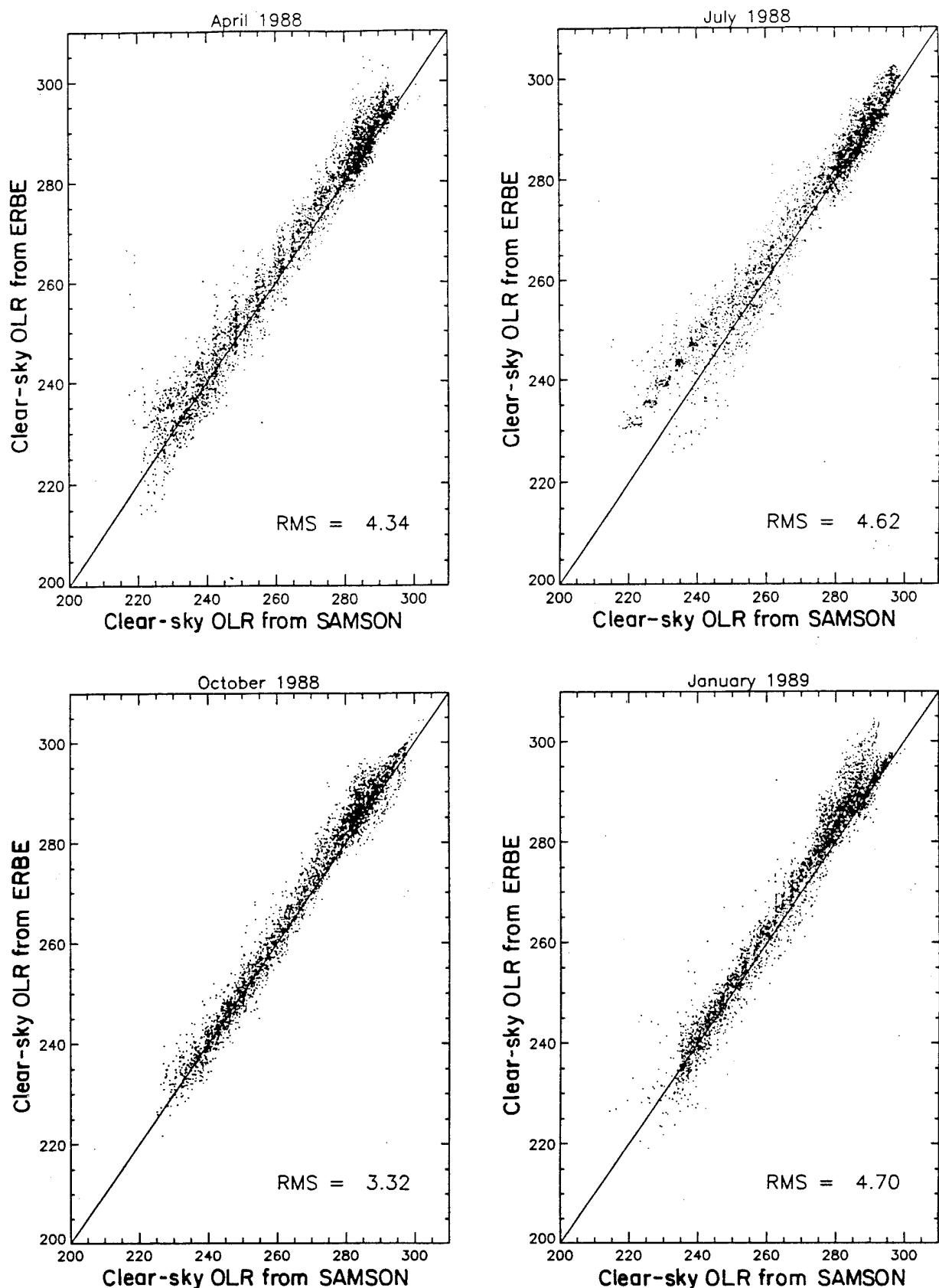
Figure 1. Scatter diagrams of (SAMSON) simulated F_∞ versus (ERBE) analyses of clear sky longwave fluxes for April, July, and September 1988 and January 1989.

SAMSON Simulation
JUL 1988

SAMSON Simulation
JAN 1989

(a)

(b)

40 50 60 70 80 90 100 110 120

40 50 60 70 80 90 100 110 12(

Linear fit from ERBE and SSM/I
JUL 1988

Linear fit from ERBE and SSM/I
JAN 1989

(c)

(d)

40 50 60 70 80 90 100 110 120

40 50 , 60 70 80 90 100 110 12(
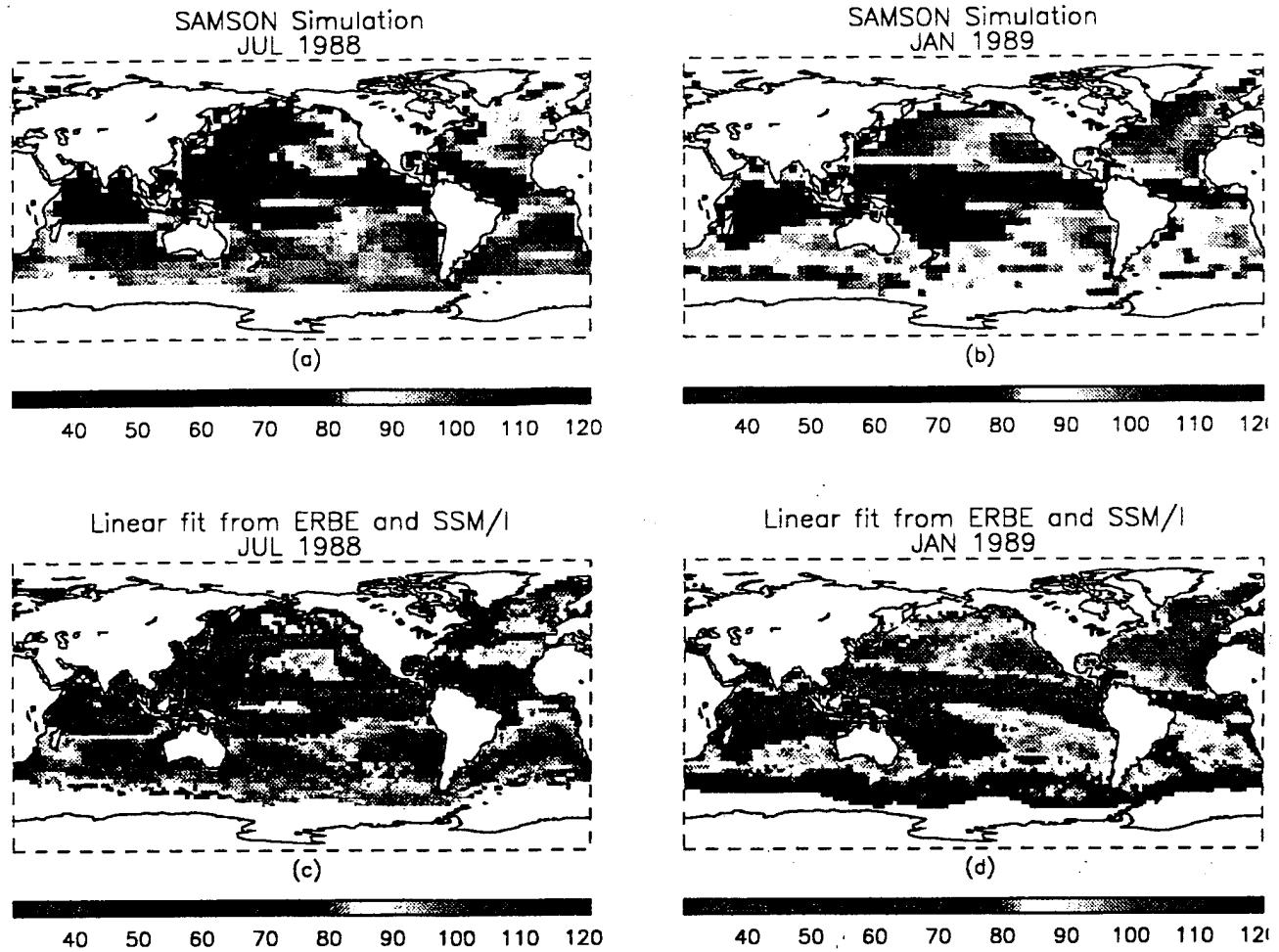
Plate 1. (a) and (b) Distributions over the oceans of the July and January SAMSON simulations of surface net longwave flux. (c) and (d) Same as Plates 1a and 1b but the net flux deduced using a linear regression of the flux ratio according to (7b) and ERBE and (SSM/I) precipitable water.

Except at a few isolated locations, there exist very little independent, research–quality data to validate the simulations of F_g shown in Plates 1a and 1b or the simple retrieval of F_g introduced later and shown in Plates 1c and 1d. A limited attempt to validate the latter is described below.

4. Flux Ratios and a Simple Description of the Planetary Greenhouse Effect

Part 1 introduced a simple model of the clear sky Earth's greenhouse effect. While that model is described briefly in that paper, a more detailed account is given here because a new relationship defined by this model is explored. As in part 1, the model is based on simple considerations of radiative equilibrium and is introduced here merely as a diagnostic guide providing a framework for analyses of the data. Its use should not be misconstrued as an assumption on our part that the Earth's climate exists in such an equilibrium state. The model derives from the radiative transfer equation applicable to a nonscattering atmosphere, namely,

$$\mu \frac{dI(\tau,\mu)}{d\tau} = I(\tau,\mu) - B(T) \qquad (1a)$$

$$-\mu \frac{dI(\tau,-\mu)}{d\tau} = I(\tau,-\mu) - B(T), \qquad (1b)$$

where I is the intensity, $\mu = \cos\theta$ where θ is the angle of the beam from the zenith.

The optical depth is defined as

$$\tau = \int_z^\infty k\rho_a dz, \qquad (2)$$

where k is the mass absorption coefficient, ρ_a is the density of the absorbing gas and z is the lowest end point of the path. Casting (1a) and (1b) into equations for upward ($F^\uparrow$) and downward ($F^\downarrow$) hemispheric fluxes leads to

$$\frac{dF^\uparrow}{d\tilde{\tau}} = F^\uparrow - \pi B, \qquad (3a)$$

$$-\frac{dF^\downarrow}{d\tilde{\tau}} = F^\downarrow - \pi B, \qquad (3b)$$

where

$$\tilde{\tau} = \frac{3}{2}\tau. \tag{4}$$

If we apply these equations to the broad band, then σT^4 replaces πB and $\tilde{\tau}$ is taken to be a gray body optical depth. Radiative equilibrium then implies that

$$F^\uparrow(\tilde{\tau} = 0) = Q_o(1 - \alpha) = F_\infty,$$

where Q_o is the global annual–mean incoming solar radiation at the top of the atmosphere and α is the planetary albedo. It also follows that

$$F_{net} = F^\uparrow(\tilde{\tau}) - F^\downarrow(\tilde{\tau}) = \text{constant}$$

which leads to the solution of (3a) and (3b) as

$$\sigma T_s^4 = \frac{F_\infty}{2}[2 + \tilde{\tau}_s] \tag{5a}$$

$$F_g = F^\downarrow(\tilde{\tau}_s) = \frac{F_\infty}{2}\tilde{\tau}_s \tag{5b}$$

where $\tau = \tau_s$ and $\tilde{\tau} = \tilde{\tau}_s$.

Part 1 uses (5a) to introduce a parameter $\mathcal{G}$ in the form

$$\mathcal{G} = \frac{\sigma T_s^4}{F_\infty} = a + b\tau_s, \tag{6a}$$

which is taken to be a measure of the strength of the planetary greenhouse effect where from (5a) and (4), $a=1$ and $b=3/4$. In a similar way the relationship (5b) provides a second flux relationship

$$\mathcal{F} = \frac{F_g}{F_\infty} = b\tau_s \tag{6b}$$

which we explore in further detail in the next section.

The flux ratio quantity given in (6a) is not only a convenient measure of the planetary greenhouse effect but it also identifies the gray body optical depth as a crucial parameter is defining the magnitude of this effect. It was also shown in part 1 that under clear sky conditions, a proportional relation between $\mathcal{G}$ and the column-integrated water vapor exists and has the form

$$\mathcal{G} = a_1 + c_1 w. \tag{7a}$$

The advantage of (7a) over other definitions is that all factors in (7a) may be independently observed over the global oceans using current satellite observations and so its viability can be tested. For example, $\mathcal{G}$ is calculated from the SST which is available from blended analyses of ship, buoy, and satellite data [e.g., *Reynolds*, 1988] and from the clear sky F_∞ which is available from ERBE data prior to 1991. The column water vapor amount w is also available over the oceans from microwave measurements obtained from the SSM/I, which have flown on the DMSP satellites since 1987. Using these data, we determine the coefficients in (7a) are $a_1 = 1.39$ and $c_1 = 0.005$ kg^{-1} m^2.

Similarly, (6b) leads us to suppose that a simple relation exists between $\mathcal{F}$ and precipitable water w of the form

$$\mathcal{F} = a_2 + c_2 w \tag{7b}$$

in an entirely analogous way to (7a) where $a_2 = 0.937$ and $c_2 = 0.0102$ kg^{-1}m^2. Unfortunately, we do not have global observations of F_g and thus we cannot derive $\mathcal{F}$ solely from independent observations to test this relationship. We propose to use the flux simulations of SAMSON in lieu of these much needed observations.

4.1. Results

Scatter plots of $\mathcal{G}$ derived from ERBE clear sky F_∞ satellite data and from SAMSON simulations of the clear sky F_∞ are compared in Figures 2a and 2b for July and Figures 2c and 2d for January 1989. In this diagram, $\mathcal{G}$ is plotted as a function of SST rather than of w, as described previously in part 1 and *Webb et al.* [1993] and *Stephens et al.* [1993]. When plotted in this way, a dramatic branching of the relation between $\mathcal{G}$ and SST appears which *Webb et al.* [1993] identify as largely due to a seasonal effect associated with changes in the vertical profile of atmospheric temperature in the middle latitudes.

The flux ratio quantity $\mathcal{F}$ derived from the same SAMSON simulations presented in Figure 2b are also given in Figure 3a. Similar flux ratios derived from monthly mean clear sky flux data obtained from simulations of the UKMO climate model are also shown in Figure 3b. The results from both sets of data show a well-defined relationship between the flux ratio and w and how this relationship is approximately linear, as predicted by (7b) for $w > 20$ kg m^{-2}. The model results exhibit a similar relationship between $\mathcal{F}$ and w and more clearly show its nonlinear but well–behaved character when $w < 20$ kg m^{-2} which resembles the well-known characteristics of the curve of growth of emission as w increases.

A simple linear fit applied over the range $w > 20$ kg m^{-2} was carried out to determine the coefficients a_2 and c_2 of (7b). The values of these coefficients are given in Figure 3a and together with SSM/I observations of w and ERBE observations of the clear sky F_∞ are then used to obtain monthly mean values of F_g over the oceans. Examples of the results of this simple retrieval are presented in Plates 1c and 1d in the form of the net longwave flux at the ocean surface. These distributions are directly comparable with the SAMSON simulations of net flux shown in Plates 1a and 1b although the higher spatial resolution of both the ERBE data and the SSM/I precipitable water data allows us to produce results in Plates 1c and 1d at a resolution of 2.5° × 2.5° compared to the 5° × 5° resolution of the SAMSON data. Despite this difference the retrieved distributions are both qualitatively and quantitatively very similar to those of SAMSON. The rms difference between the retrieved and the simulated fluxes is ±6 W m^{-2}, which is considerably smaller than the uncertainty presently expected from the direct radiometric measurements of this flux [*Dutton*, 1993]. We interpret this rms difference as a confirmation the viability of the method.

a) ERBE – July 1988

b) SAMSON – July 1988

c) ERBE – January 1989

d) SAMSON – January 1989
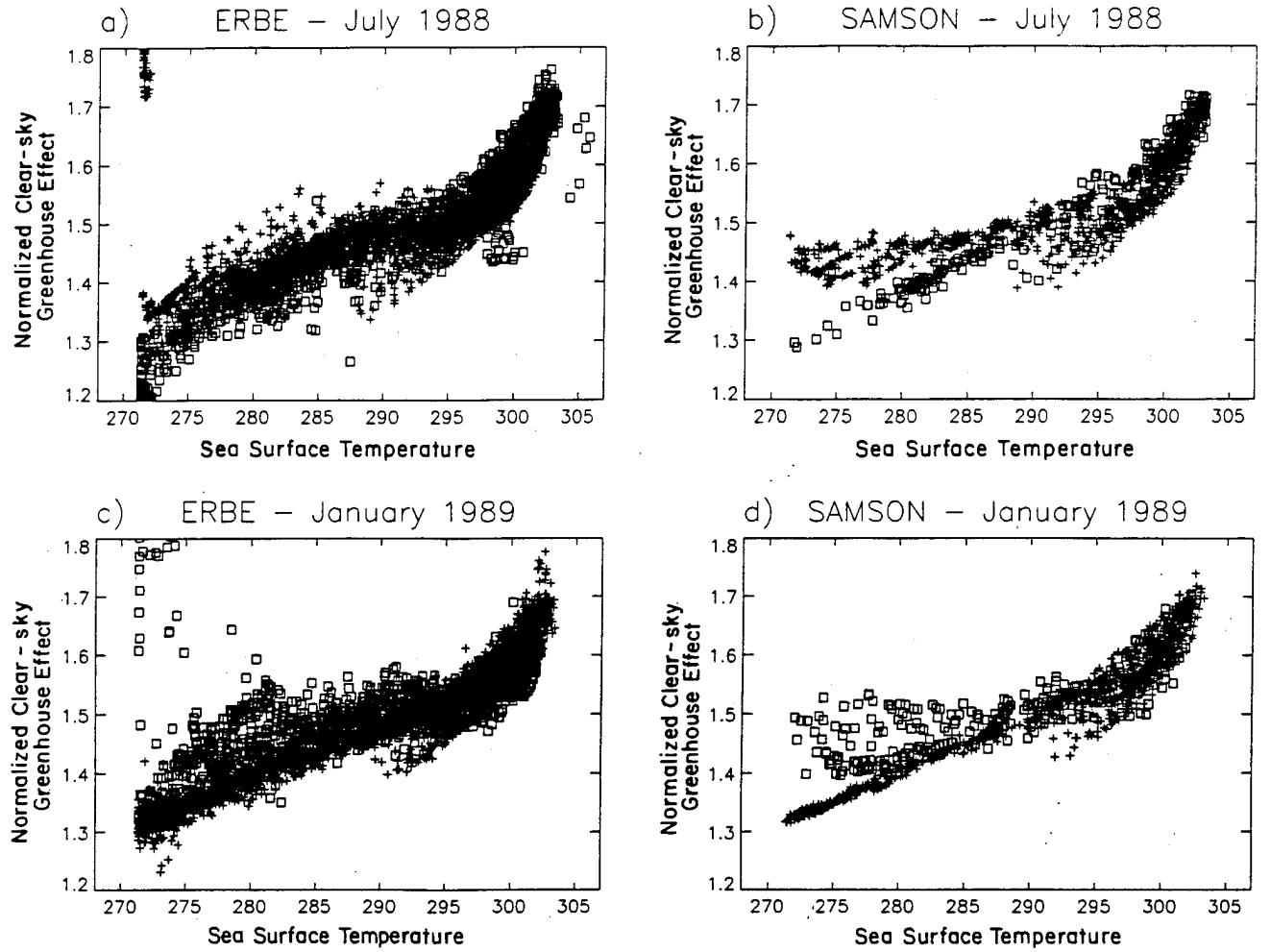
Figure 2. (a) The derived $\mathcal{G}$ from ERBE data and the Reynolds (SST) data as a function of SST for July 1988.(b) The corresponding relation using SAMSON values of F_∞. (c) and (d) Same as Figures 2a and 2b but for January 1989 defined using SAMSON simulations of F_∞.

4.2. Simple Interpretation of Flux Ratios

Webb et al. [1993] provide a simple analysis of the influences of the bulk effects of lapse rate on $\mathcal{G}$. Here we extend this analyses to $\mathcal{F}$ and consider how other factors can also potentially influence F_∞ independent of any significant change in w. In this way we offer a relatively simple framework for understanding some factors that produce the scatter in the relationships depicted in Figures 2a and 2b and Figures 3a and 3b. For example, increasing water vapor in the middle and upper troposphere only marginally affects w but may significantly alter F_∞. With all other factors fixed, increasing (decreasing) upper tropospheric moisture leads to respective decreases (increases) in F_∞ and thus to an increase (decrease) in $\mathcal{G}$. Similarly, variations in the vertical profile of temperature also alter F_∞ and thus $\mathcal{G}$. For example, a warmer (colder) atmospheric column (assuming water vapor as fixed) leads to an increase (decrease) in F_∞ and thus to a decrease (increase) in $\mathcal{G}$. These two factors, we argue, are principally responsible for producing the observed scatter.

Here we adapt and extend the simple model introduced by *Webb et al.* [1993] to explore the sensitivities of both $\mathcal{G}$ and $\mathcal{F}$ to variations in the vertical profiles of both temperature and moisture. Consider a single-layer atmosphere, as shown in the left portion of Figure 4. The upwelling radiation from the top of this atmosphere is F_∞ and the downwelling radiation at the base is F_g. These fluxes may be simply related to the radiating temperature of the atmosphere T_a (roughly the 800-mbar temperature), the emissivity of the layer ε_a, and the SST T_s via the approximate transfer equations

$$F_\infty = (1 - \varepsilon_a)\sigma T_s^4 + \varepsilon_a \sigma T_a^4$$

$$F_g = \varepsilon_a \sigma T_a^4$$

which on substitution into (6a) and (6b) and with some rearrangement give

$$\mathcal{G} = \frac{1}{1 - \varepsilon_a[1 - (T_a/T_s)^4]} \tag{8a}$$

$$\mathcal{F} = \frac{\varepsilon_a(T_a/T_s)^4}{1 - \varepsilon_a[1 - (T_a/T_s)^4]}. \tag{8b}$$
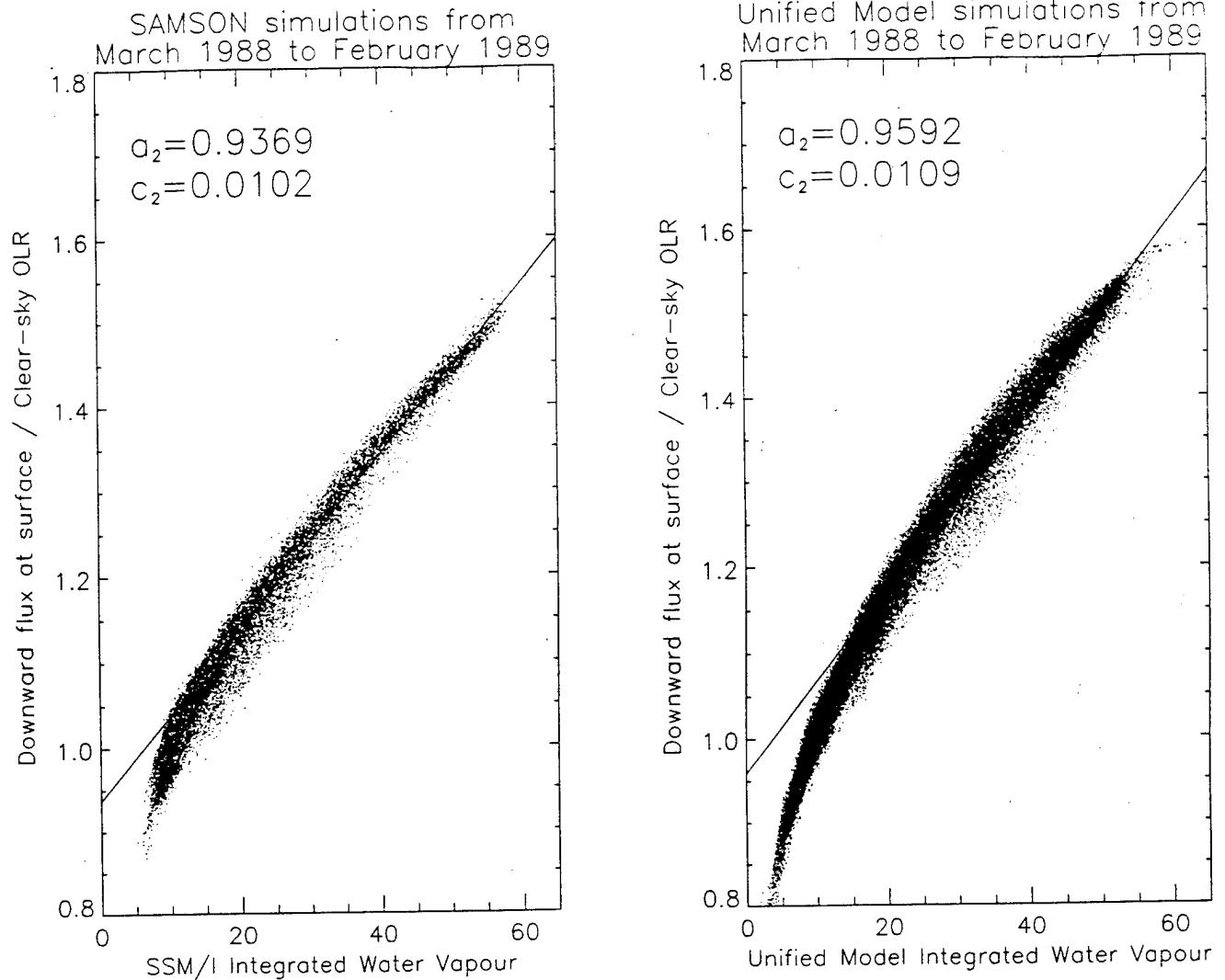
Figure 3. The flux ratio $\mathcal{F}$ derived from combined SAMSON simulations of January and July fluxes as a function of w. (b) As in Figure 3a but for the flux ratio derived using monthly mean clear sky fluxes from (CSU GCM) simulations.

Two important factors govern the behavior of both ratio quantities in these expressions, namely, the temperature profile which we associate with the temperature ratio T_a/T_s and the total column water vapor which is


Figure 4. (left) A simple-single layer atmosphere used to highlight sensitivities in flux ratio quantities (right) and a two-layer atmosphere used to identify effects of upper tropospheric moisture.

implied in ε_a. *Webb et al.* [1993] using (8a) demonstrated that the branching of the relationship between $\mathcal{G}$ and SST when T_s <285 K occurs through changes in T_a/T_s from summer to winter. During winter the lapse rate in these regions is increased (we think of this as a reduction in T_a/T_s relative to summertime conditions) and this increase in turn produces smaller values of the denominator and hence larger values of $\mathcal{G}$ relative to summertime conditions. Conversely, larger values of w lead to larger values of ε_a, a smaller denominator and thus a larger $\mathcal{G}$ which is consistent with (7a).

The effect of temperature on $\mathcal{F}$ is not so simple to diagnose as are the effects of temperature on $\mathcal{G}$ since the T_a/T_s factor appears in both the denominator and the numerator of (8b). We infer from this simple expression that the effects of changing T_a/T_s are largely canceled in this ratio.

To illustrate possible effects of the vertical structure of moisture on these ratios in a simple way, consider a two-layer atmosphere, as shown to the right of Figure 4. The properties of each layer are labeled as shown on this diagram. The fluxes to space and to the surface

simply follow as

$$F_\infty = (1 - \varepsilon_1)F_2 + \varepsilon_1 \sigma T_1^4$$

$$F_g = (1 - \varepsilon_2)\varepsilon_1 \sigma T_1^4 + \varepsilon_2 \sigma T_2^4$$

where

$$F_2 = (1 - \varepsilon_2)\sigma T_s^4 + \varepsilon_2 \sigma T_2^4.$$

A change in these fluxes due to a change in the water vapor path will be denoted as $\Delta F^{(1),(2)}$ depending on whether this change occurs either in the top layer 1 or the bottom layer 2, respectively. It is trivial to show that these flux changes are

$$\Delta F_\infty^{(1)} = \Delta \varepsilon_1 [\sigma T_1^4 - F_2]$$

$$\Delta F_\infty^{(2)} = \Delta \varepsilon_2 (1 - \varepsilon_1)[\sigma T_2^4 - \sigma T_s^4]$$

and that

$$\Delta F_g^{(1)} = \Delta \varepsilon_1 (1 - \varepsilon_2)\sigma T_1^4$$

$$\Delta F_g^{(2)} = \Delta \varepsilon_2 [\sigma T_2^4 - \varepsilon_1 \sigma T_1^4]$$

for a given change in layer emissivity that occurs as a result of respective changes in water vapor path. The change in flux ratios due to these path changes is then

$$\frac{\Delta \mathcal{F}}{\mathcal{F}} = \frac{\Delta F_g}{F_g} - \frac{\Delta F_\infty}{F_\infty}$$

$$\frac{\Delta \mathcal{G}}{\mathcal{G}} = -\frac{\Delta F_\infty}{F_\infty}.$$

Estimates of the flux changes $\Delta F_\infty^{(1),(2)}$ and $\Delta F_g^{(1),(2)}$ together with the changes in the ratios $\Delta \mathcal{F}^{(1),(2)}/\mathcal{F}$ and $\Delta \mathcal{G}^{(1),(2)}/\mathcal{G}$ are given in Table 1 based on radiative transfer calculations using the two-stream model of *Stackhouse and Stephens* [1991] applied to the *McClatchey et al.* [1972] midlatitude summer atmosphere. In these calculations we have taken layer 2 to represent the layer from the surface to approximately 500 mbar with a path $u_1 = 28.2$ mm and layer 1 to represent the layer above 500 mbar with $u_2 = 1.8$ mm. The quantities given in the table are derived for a specified change in layer emissivities and the parameter values given. The emissivity values given were derived from the formulae of *Rodgers* [1967] and the quoted changes in emissivity are a result of 10% changes in u_1 and u_2, respectively. According to these results a 10% change in upper tropospheric moisture (i.e., an increase in u_1 of 0.2 mm) has a threefold larger effect on F_∞ than does an equivalent percentage change (but significantly larger absolute change of 2.8 mm) in lower tropospheric water vapor. This is due to a combination of the nonlinear curve of growth of emissivity as a function of u where small changes in path in an existing dry layer leads to a larger change in emissivity than occurs when the path of moist layer is increased by the same amount. This feature is indicated by the a factor of 2 difference in $\Delta \varepsilon$ listed in the table. This disproportionate influence of upper tropospheric moisture on F_∞ and, subsequently, on $\mathcal{G}$ has also been noted by others in a slightly different context [e.g., *Shine and Sinha*, 1991]. According to the results

Table 1. Changes in Fluxes and Flux Ratios

$\Delta \varepsilon_1$	$\Delta \varepsilon_2$	ΔF_∞	ΔF_g	$\Delta \mathcal{G}/\mathcal{G}$	$\Delta \mathcal{F}/\mathcal{F}$
0.02	$\cdots$	-1.4	0.8	0.005	0.007
$\cdots$	0.01	-0.48	1.8	0.0017	0.0066

The values in this table were derived for the following: $\sigma T_s^4 = 423$, $F_\infty = 289$, $F_g = 338$, $F_2^\uparrow (\approx F_{500mb}^\uparrow) = 338$, $F_2^\downarrow (\approx F_{500mb}^\downarrow) = 139$, $u_2 = 28.2$, $u_1 = 1.8$, $\varepsilon_1 = 0.85$, $\varepsilon_2 = 0.52$ where the fluxes are in W m^{-2} and the path quantities are in mm.

listed in Table 1, changes in upper tropospheric moisture, which go undetected by sensors such as the SSM/I, can also affect $\mathcal{F}$ and it is reasonable to expect that the scatter in the relationship shown in Figure 3 is due to variations in the moisture profile, including changes in the upper tropospheric moisture that are not necessarily reflected in variations in w.

5. Validation of the $\mathcal{F}$ Ratio

The $\mathcal{F}-w$ relationship shown above is now checked using both independent surface longwave flux measurements and concurrent radiosonde data. These observational data were obtained from both ship-borne and island-based measurements, but unfortunately they were available only after the failure of the ERBE scanning radiometers. Thus the clear sky values of F_∞ used to derive the ratio $\mathcal{F}$ were obtained from radiative transfer calculations using the column version of the SAMSON and profile information prescribed by the radiosonde data collected at the measurement site as input.

The surface flux data were first analyzed to identify clear sky periods and the fluxes at these times were then averaged to produce 30-min averaged fluxes. Coincident ship-borne observer reports of cloudiness were used to determine these clear sky conditions which were

Table 2a. Monthly Mean Infrared Fluxes

Cruise	F_g	F_∞	w	$\mathcal{F}$
Mediterranean	315	293	19	1.074
	355	313	18	1.133
	340	321	20	1.060
	360	324	21	1.112
	350	317	21	1.104
	360	320	23	1.125
	345	319	19	1.081
	350	323	17	1.083
	335	316	20	1.060
	355	319	20	1.112
	335	305	21	1.096
	375	302	26	1.241
Arctic	250	260	13	0.961
	235	259	11	0.906
	225	249	7	0.904
	220	248	7	0.887
	210	250	6	0.840
	225	247	7	0.904

Monthly mean (mm) infrared fluxes (in W m^{-2}) and colocated sonde precipitable water content (in mm) measured during two cruises. Calculated values of F_∞ are also presented.

Table 2b. Monthly Mean and Standard Deviation of the Infrared Fluxes

Site	Month	All Sky						Clear Sky				
		F_g	σ_F	w	σ_w	N	F_g	σ_F	w	σ_w	N	F_∞
Chuuk	12/92	405.0	11.7	40.7	7.1	8	399.4	2.0	41.4	10.4	3	298.7
	1/93	417.4	15.2	48.2	11.0	29	407.0	9.5	44.5	9.5	9	300.9
	2/93	414.0	11.4	45.8	10.2	25	411.0	8.7	43.7	7.0	12	295.6
Majuro	12/92	423.0	11.7	46.0	9.6	22	411.6	9.7	40.4	7.1	6	309.4
	1/93	427.4	12.8	51.6	10.7	27	419.5	12.3	45.4	9.9	8	300.1
	2/93	422.8	15.1	47.5	11.2	24	408.7	9.7	38.7	8.0	10	299.5
Kavieng	1/93	443.9	6.0	52.6	3.4	6	441.4	0.5	54.0	0.2	2	284.2
	2/93	435.6	4.6	53.3	4.9	25	433.9	2.8	51.6	3.8	11	288.1
Darwin	12/92	446.7	9.7	46.4	6.3	20	451.1	4.7	42.1	6.2	6	302.6
	1/93	447.6	9.9	52.9	8.4	29	449.0	10.0	47.7	6.6	11	296.0
	2/93	441.6	7.3	50.5	5.4	24	441.5	9.6	48.9	4.7	7	286.6

Monthly mean and standard deviation of the infrared fluxes (in W m^{-2}) and co-located sonde precipitable water content and standard deviation (in mm) during TOGA/COARE. The fluxes indicated by the superscript 's' are those derived from SAMSON.

defined when cloud amounts of 3/10 cloudiness or less prevailed during the time of measurement. The flux measurements, simulated values of F_∞, the values of w derived from the radiosondes as well as values of the flux ratio are given in Table 2a. Simulated values of F_g are not given but the rms differences between these simulated fluxes and measured fluxes is 12.7 and 9.4 W m^{-2} for the Mediterranean and Arctic measurements, respectively.

Surface observations of cloudiness over the island sites were not available at the time of the analyses reported here, so a method was established for identifying clear skies based on the measurements of the accompanying solar flux data. The effects of possible cloud contamination in the day time TOGA data are not considered to be a significant problem since most cloudiness conditions could be readily identified in the solar flux time series and even deep clouds produce only a relatively small change in the longwave flux in the moist conditions that prevail at the TOGA island sites. The more subtle effects of broken clouds or thin clouds that are more difficult to detect in the surface solar flux measurements also have little effect on the measurements of F_g. Table 2b presents the longwave fluxes measured at the TOGA sites separated into all–sky and clear sky conditions and provides the SAMSON simulation of F_∞ and the derived flux ratio for clear sky conditions. The simulated fluxes of F_g are also not presented in this table and the rms differences between the measured and the simulated values of F_g fluxes are within 10 W m^{-2} for these TOGA stations. The data in Table 2b support the assertion that the higher-moisture content of the tropical atmosphere masks the effects of emission from clouds measured at the surface. This may be seen from the difference between cloudy and clear sky fluxes obtained from the subtraction of all-sky fluxes F_g and F_g obtained under clear sky conditions as well as the standard deviations of each of these fluxes. The smallness of both the flux differences and their variability is consistent with the notion that the effects of partially cloudy skies which may be incorrectly diagnosed as clear skies

are not likely to be significantly larger than 10 W m^{-2}.

Values of the flux ratio $\mathcal{F}$ obtained from the measurements of F_g and the simulations of F_∞ are presented in both Figure 5 as well as in Tables 2a and 2b as a function of the radiosonde derived precipitable water w. Ratio values for the Arctic, Mediterranean and tropical Pacific are identified in Figure 5 by different symbols. The linear regression of the SAMSON simulations taken from Figure 3a is also shown in the diagram (dashed line) for reference as well as simulated ratios obtained with the SAMSON radiative transfer model and five McClatchey et al. [1972] model atmospheres. The latter calculations, indicated by pluses connected by lines, are the results of a series of three calculations carried out for each of the five model atmospheres. The water vapor profiles of these atmospheres was multiplied at each level by one of three constant factors (0.75, 1.0, and 1.25, respectively). These calculations provide a reference for comparison with the measurements, espe-
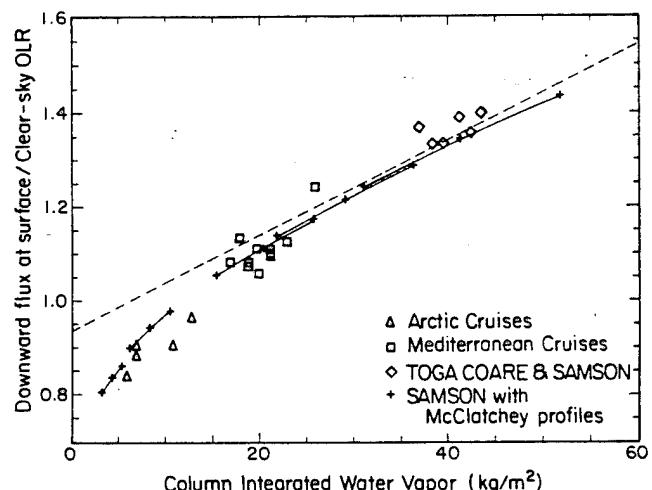

Figure 5. The flux ratio $\mathcal{F}$ as a function of w for model-derived relationships (points connected by lines), the regression line derived from the results of Figure 3a and from the measurements indicated.

cially those over the Arctic where the values of w are smallest and the relationship between $\mathcal{F}$ and w is most nonlinear. The calculations using these model atmospheres produce a relationship that also closely fits both the SAMSON regression relation and the flux ratio data measurements. The agreement between the two modeled relationships and the data is offered as a form of validation of the $\mathcal{F}-w$ relationship.

6. Column Infrared Cooling Rates

The loss of longwave radiative energy by the atmosphere is governed by the emissions of infrared radiation from the atmosphere to space and toward the surface. We can define this loss in terms of the following infrared budget:

$$\Delta F = (\sigma T_s^4 - F_\infty - F_g), \qquad (9)$$

where the first term of the right hand side is given by the SST data,

the second term is derived from ERBE measurements and the third term in the balance follows from (7b) using values of the parameters a_2 and c_2 derived from SAMSON together with satellite observations of w and F_∞ for clear sky conditions.

6.1. Clear Sky Cooling Rates

It is common to express the loss of radiant energy by the atmosphere as the rate of cooling of the atmospheric column which follows from (9) as

$$\frac{dT}{dt} = \frac{g}{c_p p_s} \Delta F \qquad (10)$$

where g is the acceleration due to gravity, c_p is the specific heat of air at constant pressure and p_s is the surface pressure. After rearrangement the column heating becomes

$$\frac{dT}{dt} = \frac{g F_\infty}{c_p p_s}[\mathcal{G} - \mathcal{F} - 1], \qquad (11)$$

where according to (7a) and (7b) the two terms in brackets vary in a systematic way with w. Furthermore for a given w the heating of the column varies proportionally with the clear sky outgoing longwave radiation F_∞ which is a result consistent with the empirical findings obtained from balloon measurements of radiative fluxes by *Sabatini and Suomi* [1962].

We use our retrieval strategy to estimate clear sky values of F_g from satellite measurements of F_∞ and w as described above and substitute a value of 1013 mbar for p_s and use the monthly mean SST of Reynolds for T_s in (10) and (11) to arrive at monthly mean distributions of the column-averaged clear sky heating rates shown in Plates 2a and 2b (negative values represent cooling) for July 1988 and January 1989, respectively. A reasonable estimate of the uncertainty of the monthly averaged values of F_∞ and F_g is ±10 W m^{-2} based on published estimates in ERBE clear sky flux uncertainties and in the uncertainties in F_g expressed by the rms differences

discussed in relation to the comparisons shown in Plate 1. These flux uncertainties in turn imply an uncertainty of approximately ±0.2 K d^{-1} in the column cooling rate. The SSM/I fields of w for July 1988 and January 1989 which are used to produce these heating rate distributions are also shown in Plates 2c and d for comparison. It is evident that the clear sky column heating rate distributions resemble the distributions of w which is consistent with (11) and the relationship among $\mathcal{G}$, $\mathcal{F}$, and w. The largest coolings occur in the moist equatorial regions and in the areas of moisture convergence over the northwest Pacific and Atlantic Oceans during July as well as in the South Pacific convergence zone.

The association between the column-averaged heating rate and w is explored further in Figures 6a and b, where the data displayed in Plates 2a and c and 2b and d respectively, are plotted against each other. Based on (11) and the relationships assumed in (7a) and (7b), we expect the cooling rate to increase in an approximate linear way with increasing w, as shown in Figures 6a and 6b. Linear fits of both $\mathcal{F}$ and $\mathcal{G}$ as a function of w yield the following slope coefficients: $c_2 = 0.01015$ (kg m^{-2})$^{-1}$ and $c_1 = 0.00524$ (kg m^{-2})$^{-1}$, respectively, which according to (11) implies a slope of -0.005 (kg m^{-2})$^{-1}$. An example of a relationship with this slope, defined using the global-mean value $F_\infty = 266$ W m^{-2} is also given on each diagram for reference. The column cooling rate deviates from this simple linear dependence on w in such a way that the rate of increase of column cooling with increasing w above about 40 kg m^{-2} decreases.

When the column cooling rate is expressed as a function of SST rather than as a function of w, as it is shown in Figures 6c and 6d, a number of features emerge. The first is the general change in the cooling SST slope for SST exceeding approximately 295 K due to the rapid increase in w as the SST increases beyond this value. The second feature that emerges from Figures 6c and 6d are the winter-summer hemispheric branches in the column cooling similar to those noted in the $\mathcal{G}$-SST relationship. The characteristics of the relation between the column cooling rate and the SST, especially the increased rate of cooling with increasing SST, may be better understood by reference to Figure 7. This diagram presents scatter diagrams of fluxes as a function of SST. The left panels are F_∞ and F_g derived from satellite data for July 1988 (left panels) as a function of SST and the matching fluxes derived from SAMSON are shown to the right. We can deduce that the enhanced rate of change of cooling for SSTs greater than about 295 K is a result of the enhanced emission from the atmosphere to the surface associated with the increasing water vapor with SST at these temperatures. The rate of increase of emission from the atmosphere as the SST increases exceeds the rate of change of the emission from the surface (i.e., σT_s^4). The latter is represented by the solid line in the bottom two panels of Figure 7. For the SST> 290 K, we deduce that $\Delta F_g/\Delta$SST ≈ 15 W m^{-2} K^{-1} and that $\Delta\sigma T_s^4/\Delta$SST ≈ 6 W m^{-2} K^{-1}.
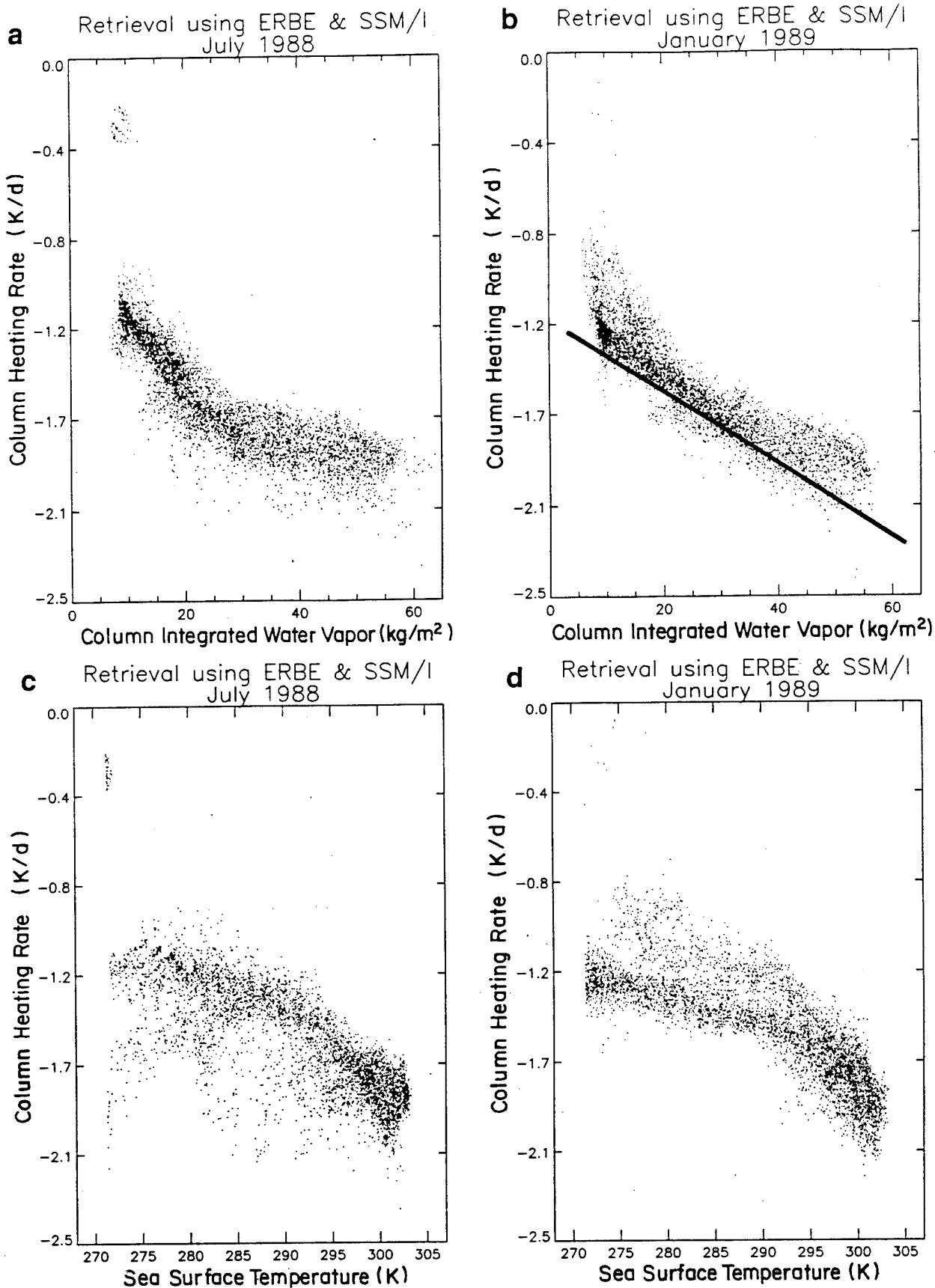
Figure 6. The clear sky column cooling rate correlated with the SSM/I-derived column water vapor obtained from the data of (a) July 1988 and (b) January 1989. The solid line are simple linear relationships implied by equations (11), (7a), and (7b) and $F_\infty = 266$ W m^{-2}.   The clear sky column cooling rate correlated with SST for (c) July 1988 and (d) January 1989.

Column Heating Rates from SSM/I and ERBE
JUL 1988

(a)

-2.2   -2   -1.8   -1.6   -1.4   -1.2   -1   -0.8
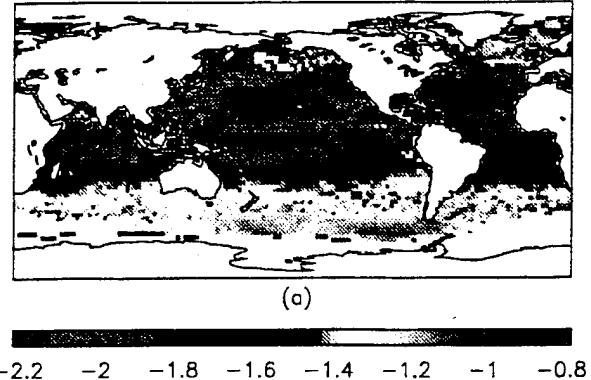
Column Heating Rates from SSM/I and ERBE
JAN 1989

(b)

-2.2   -2   -1.8   -1.6   -1.4   -1.2   -1   -0.8
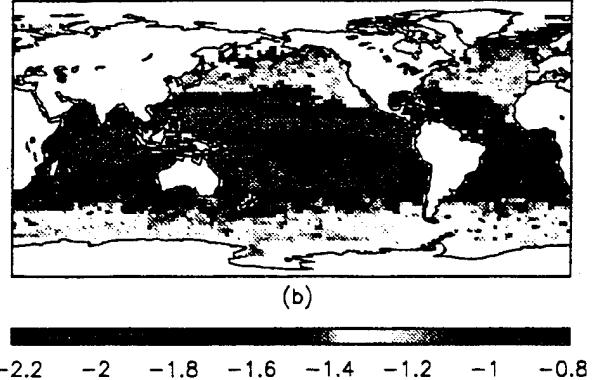
SSM/I Precipitable Water
JUL 1988

(c)

0 5 10 15 20 25 30 35 40 45 50 55 60 65
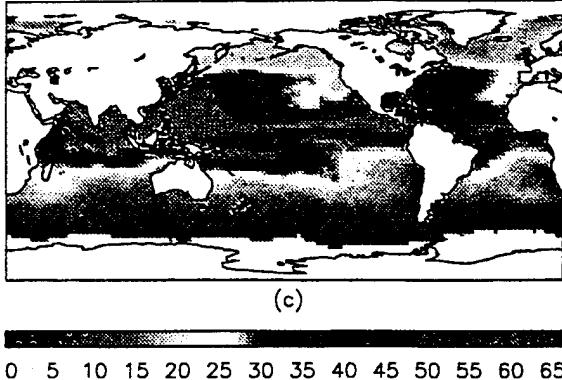
SSM/I Precipitable Water
JAN 1989

(d)

0 5 10 15 20 25 30 35 40 45 50 55 60 65
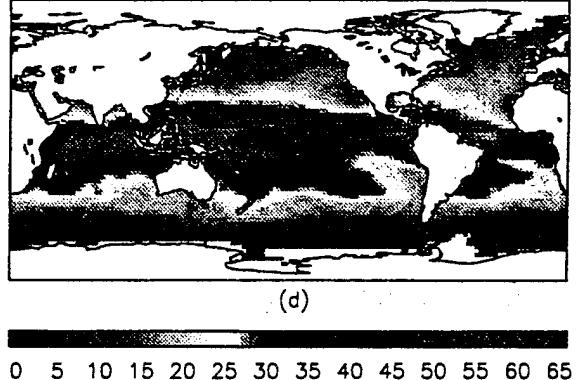
Plate 2. (a) and (b) Clear sky column cooling rate distributions for July 1988 and January 1989 (in units of K d^{-1}). (c) and (d) Same as Plates 2a and 2b except for vertically integrated water vapor (in units of kg m^{-2}).

6.2. Cloudy Sky Cooling Rate Differences

We introduce the effects of clouds on the column cooling rate in terms of the following difference quantity

$$\Delta\left(\frac{dT}{dt}\right) = \left(\frac{dT}{dt}\right)_{\text{cloudy}} - \left(\frac{dT}{dt}\right)_{\text{clear}},$$

which, in flux form, is

$$\Delta\left(\frac{dT}{dt}\right) = -\frac{gF_\infty}{c_p p_s}[\Delta F_g + \Delta F_\infty], \qquad (12)$$

where ΔF_g and ΔF_∞ are the respective differences between all (cloudy) sky and clear sky fluxes. Since the fluxes emitted to the surface under normal cloudy conditions exceed the clear sky fluxes, $\Delta F_g > 0$, so that this term contributes to the radiative cooling of the column. Conversely, since the radiating temperature of clouds is typically colder than the equivalent radiating temperature of the surrounding clear sky, $\Delta F_\infty < 0$, so the second term of (12) contributes to column heating. Therefore the net effect of clouds on the column longwave heating rate occurs as a result of the difference between two competing factors, a cooling factor associated with increased emission by clouds in the atmosphere to the surface and a heating factor associated with decreased emission by clouds in the atmosphere to space.

The flux difference quantity ΔF_∞ is available from ERBE analyses (this is the negative of the longwave cloud radiative forcing), whereas global estimates of ΔF_g is a function of unknown cloud base temperatures among other parameters. It is therefore not possible to estimate the global effect of clouds on the column heating rate using presently available measurements from satellites and this remains a topic of some challenge for future research. However, it is possible to provide upper and lower bounds on the effects of clouds on the column heating rate. One extreme, we propose, may be obtained simply by setting ΔF_g either to zero or more realistically, as we show below to a small, constant value $\delta_{\min}$. With $\delta_{\min} = 0$, we obtain the maximum possible heating potential of clouds and for convenience refer to this extreme as the heating limit. The other extreme occurs when ΔF_g is set to its maximum possible value which we propose occurs when the downwelling long-
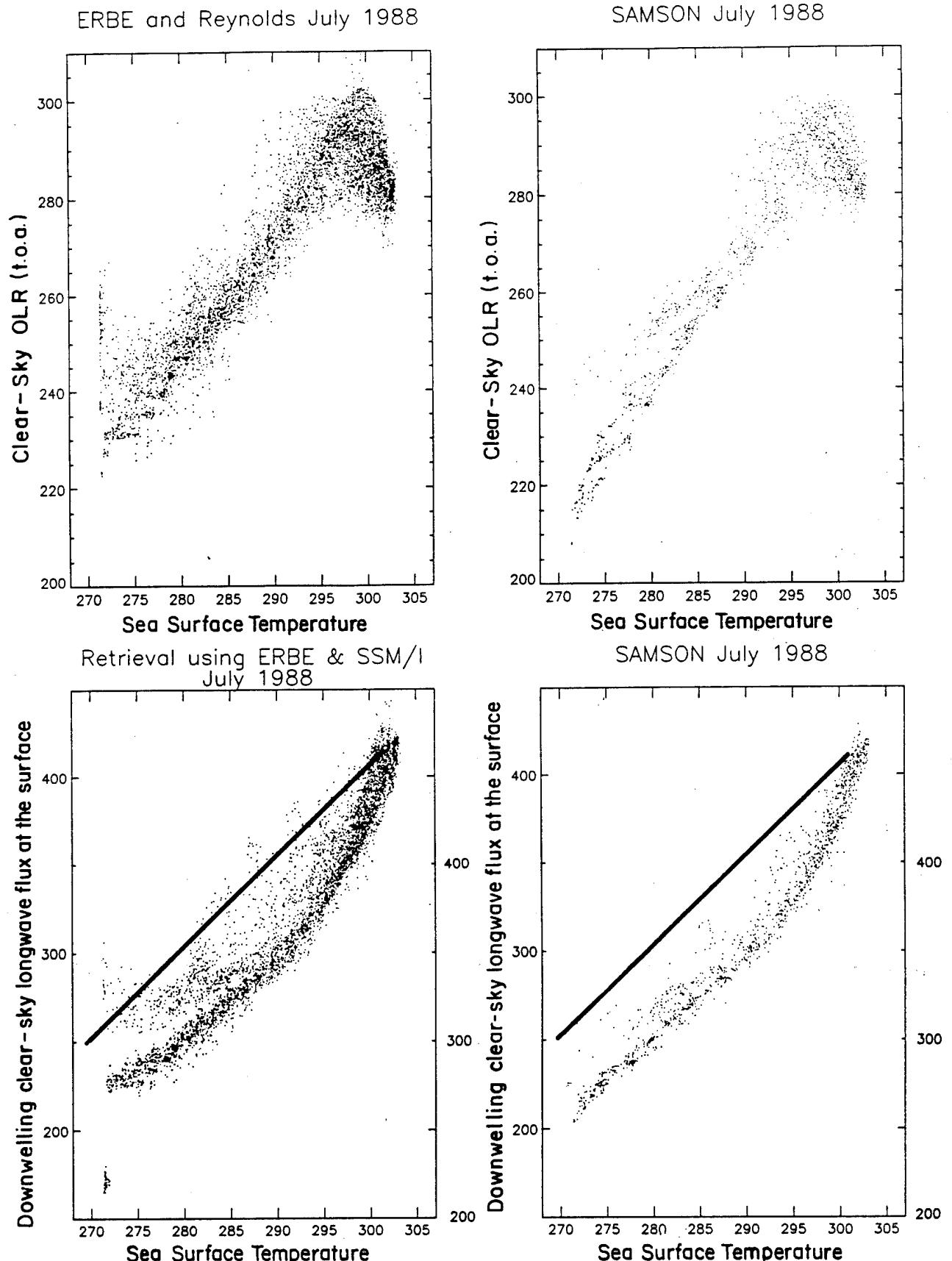
Figure 7. F_∞ as a function of SST (top two panels) from ERBE (left) and SAMSON (right). F_g as a function of SST (bottom panels) derived from the retrieval method described in the text (left) and from SAMSON (right). The solid line on each of the bottom panels represents blackbody emission at the prescribed value of the SST and the scale on the left represents the scale of this blackbody flux.

-0.70 -0.50 -0.30 -0.10 0.10 0.30 0.50 0.70

-0.80 -0.60 -0.40 -0.20 0.00 0.20 0.40 0.60 0.80

(a) Heating Limit

-0.70 -0.50 -0.30 -0.10 0.10 0.30 0.50 0.70

-0.80 -0.60 -0.40 -0.20 0.00 0.20 0.40 0.60 0.80
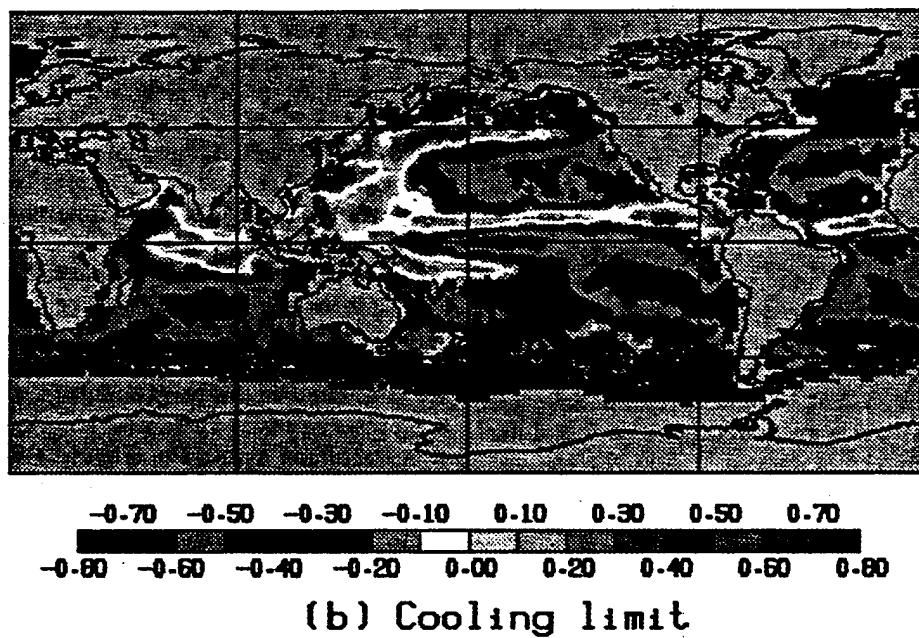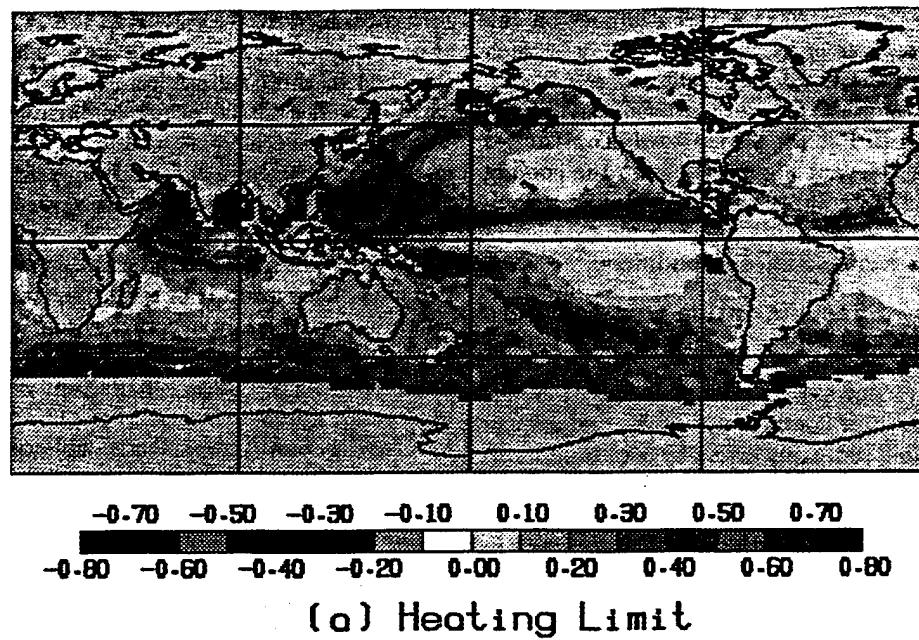
(b) Cooling limit

Plate 3. (a) The heating limit of clouds on the column radiative cooling rate and (b) the cooling limit defined assuming a cloud base temperature that is 2 K less than the SST. Both results are for July 1988.

wave flux to the surface under cloudy skies equals the blackbody flux emitted by the surface and specified by the given SST. For convenience, we represent this extreme by δ_{max}, and define it in terms of a small temperature difference ΔT according to

$$\delta_{max}(\Delta T) = \sigma(T_s - \Delta T)^4 - (F_g)_{clear},$$

where T_s is the given SST. Although the maximum cooling potential of clouds obviously occurs when $\Delta T = 0$, this clearly represents an extreme circumstance that oc-

curs, for example, in the case of thick fog on the ground. We propose that a more realistic cooling limit is one that corresponds to a non–zero value of ΔT and we use $\Delta T = 2$ K for the example given below.

Distributions of the heating and cooling limits of clouds are presented in Plates 3a and 3b, respectively, for July 1988. The distribution shown for the heating limit (Plate 3a) is just the distribution of the longwave cloud forcing expressed here in heating rate units rather than in the more usual flux units. Regions of low clouds, such as over the eastern portions of the subtropical Pa-

cific and Atlantic Oceans, have a small impact on the heating, whereas regions of high, cold–top clouds, such as in the vicinity of the the Asian monsoon, the Pacific and Atlantic InterTropical Convergence Zones (ITCZs) and into the northern Pacific, dramatically contributes to this heating. A relevant highlight of the the cooling limit distribution (Plate 3b) is the large cooling associated with regions of low clouds and the persistence of column heating in regions of deep cloudiness.

6.3. Cloudy Sky Effects Relative to a Moisture Threshold

It is reasonable to propose that the effects of clouds on the infrared column cooling in certain regions can be more tightly defined than given by the bounds illustrated in Plates3a and 3b. For example, under conditions of marine boundary layer stratiform cloud we may be able to define ΔF_g with tolerable accuracy in a manner very similar to that given above where δ_{max} was defined for $\Delta T = 2$. In fact, the cloud effect on the column cooling in these regions as shown in Plate 3b, is probably a reasonable estimate of the actual effect of these low–level clouds.

We also suggest that where there is a sufficient water vapor burden, introduced here in terms a threshold value of w, the difference between cloudy and clear sky longwave flux to the ground is sufficiently small that uncertainties in the value of this difference are also acceptably small within say 10 W m^{-2}. In these regions the impact of clouds on the column cooling rate will thus resemble the heating limit illustrated in Plate 3a. It thus remains to test this hypothesis and establish the appropriate threshold value of w.

Flux difference data derived from three different sources, all displayed in Figure 8 as a function of w, are used to test this idea. The curves drawn represent the relationships between ΔF_g obtained from model calculations, and the symbols are monthly mean flux differ-

ences obtained from analyses of the TOGA surface radiation budget and radiosonde data. The horizontal bars attached to these points indicate the range of variability of clear sky w that occurred during the given month. The solid line is the relationship obtained using monthly mean flux differences derived from simulations using the CSU GCM and thus represent a variety of cloud altitude conditions (it is relevant to recall that the CSU GCM does not have partial cloudiness). The remaining two curves are a result of radiative transfer calculations assuming completely overcast conditions with an optically thick cloud layers located between 8–9 km and 1–2 km, respectively. These calculations were performed using the *Stackhouse and Stephens* [1991] model and the McClatchey et al. tropical atmosphere and, as above, w was varied by multiplying the specific humidity at each level by a constant multiplicative factor.

The largest flux differences occur when overcast low cloud conditions prevail. According to the results presented in Figure 8, we assume that the monthly mean value of ΔF_g for $w > 30$ kg m^{-2} is 15 W m^{-2} and that a reasonable measure of the uncertainty of this value is of the order of 10 W m^{-2} based on the spread shown in Figure 8 and on the measured variances of the TOGA cloudy sky and clear sky longwave fluxes (Table 2b).

The July 1988 and January 1989 cloud heating difference distributions in regions where $w > 30$ kg m^{-2} are presented in Plates 4a and 4b. This heating is largest in the western Pacific approaching a magnitude of 0.9 K d^{-1} which, when contrasted against the results shown in Plates 2a and 2b, is approximately half of the clear sky column cooling in these regions. The net longwave radiative heating of the atmospheric column is then obtained as the sum of the heatings given in Plates 4a and 4b and the clear sky column cooling shown previously in Plates 2a and b. The combined heating distributions are presented in Plates 4c and 4d and these suggest the presence of a substantial longwave heating gradients stretching across the tropical Pacific south of the ITCZ in January (Plate 4c) and north of the ITCZ in July (Plate 4d). The eastern portions of the tropical Pacific are regions of prevalent low cloudiness and the net column cooling in these regions exceeds the clear sky values which are approximately 2 K d^{-1}. In contrast to this strong cooling in the eastern portions of the tropical and subtropical Pacific is the weaker cooling of approximately 1 K d^{-1} in the western Pacific where heating by deep convective cloud systems (Plates 4a and 4b) approximately halve the clear sky values of the column cooling.

The longitudinal radiative heating gradients that are set up across the Pacific have the same sign as the gradients associated with latent heating due to precipitation. The significance of these heating gradients and the possible circulations they induce is studied by *Slingo and Slingo* [1989].

7. Summary and Conclusion

This paper is the final in a series of papers which seek to explore new uses of global satellite data to study rela-
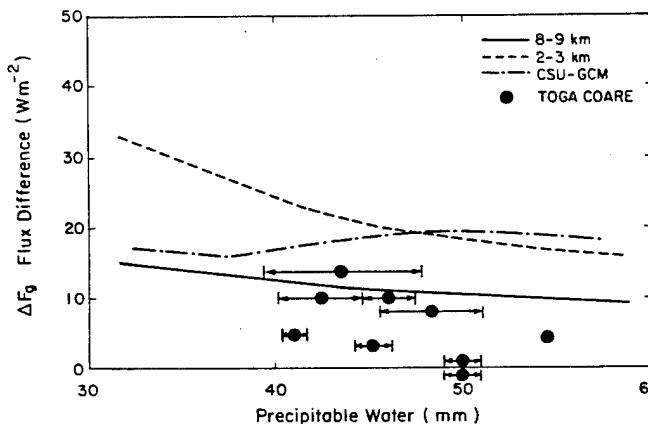

Figure 8. The difference between cloud sky and clear sky longwave flux to the surface as a function of the integrated water vapor content. Shown are flux differences derived from a radiative transfer model, the CSU GCM, and from the TOGA surface radiation budget data.
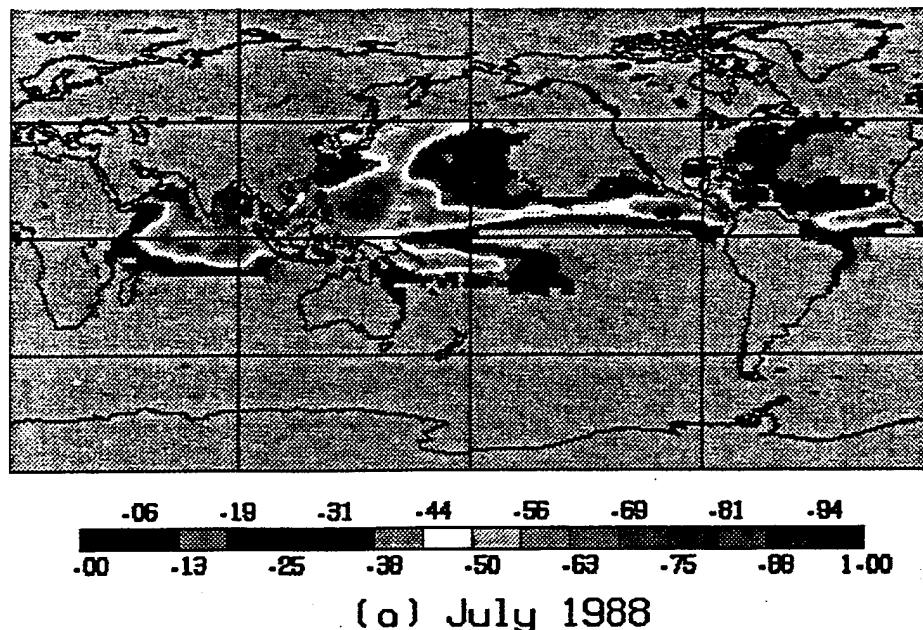
(a) July 1988
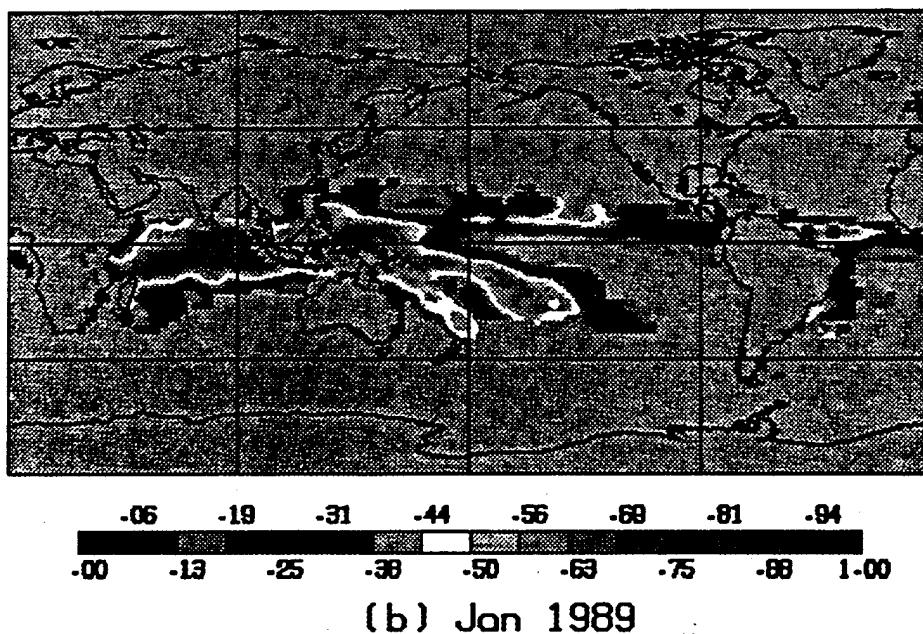
(b) Jan 1989

Plate 4. (a) and (b) The longwave column heating by clouds in an atmosphere for which $w > 30$ kg m^{-2} derived assuming $\Delta F_g = 15$ W m^{-2} for July 1988 and January 1989, respectively. (c) and (d) The net longwave column cooling (sum of Plates 2a and 2b and Plates 4a and 4b for July 1988 and January 1989, respectively, for those regions where $w > 30$ kg m^{-2}.

tionships between certain aspects of the energy budget of the climate system and its hydrological cycle. The motivation, in part, is to develop useful diagnostic tests of current global climate models. The present paper introduces a simple method for deriving climatological values of the longwave flux emitted from the clear sky atmosphere to the ground and presents a validation of this approach. A related goal of the research described

in this paper is to apply these fluxes to the calculation of the column cooling rate of the atmosphere. We consider it appropriate to view this cooling as a fundamental measure of the activity of the Earth's greenhouse effect and the global character of this cooling in turn as an indirect measure of the Earth's hydrological cycle. As such, we explore bulk relationships between the clear sky column cooling rate and the hydrological cy-

-2.01　-1.84　-1.66　-1.49　-1.31　-1.14　-.96　-.79

-2.10　-1.92　-1.75　-1.57　-1.40　-1.23　-1.05　-.88　-.70

(c) Net Cooling　July 1988

-2.01　-1.84　-1.66　-1.49　-1.31　-1.14　-.96　-.79

-2.10　-1.92　-1.75　-1.57　-1.40　-1.23　-1.05　-.88　-.70

(d) Net Cooling　Jan 1989
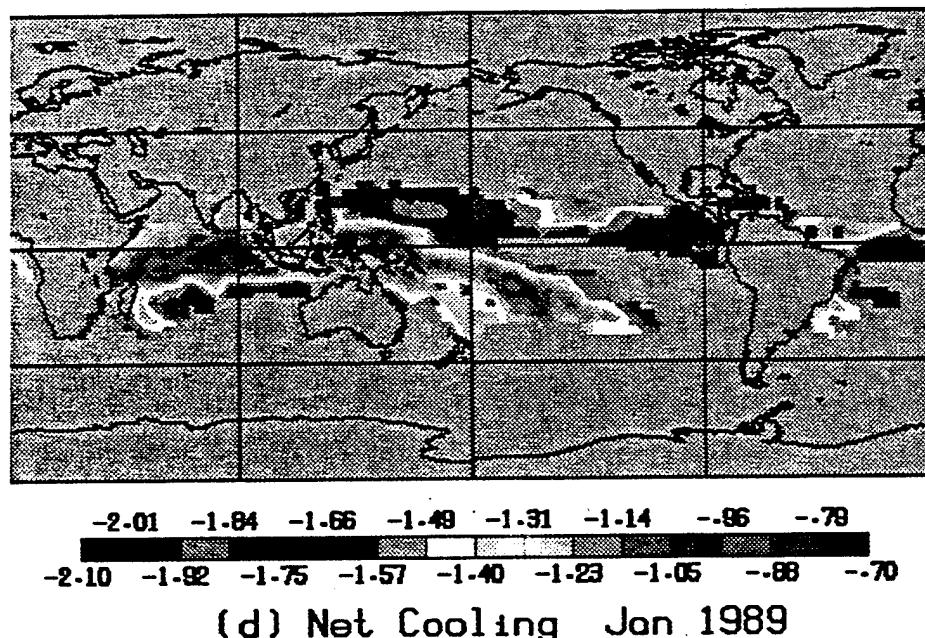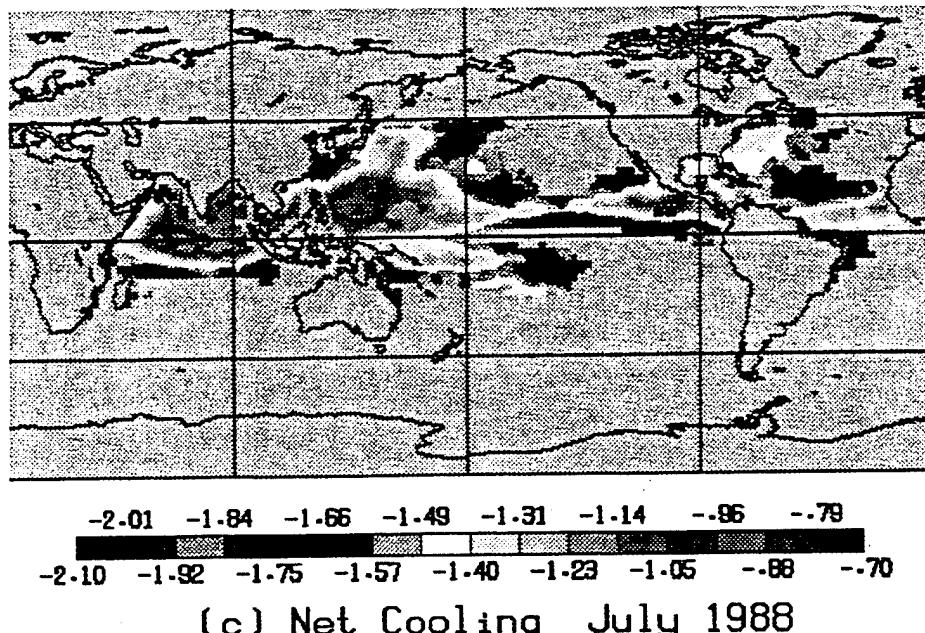
Plate 4. (continued)

cle as diagnosed by the column water vapor amount. We also explore, in a limited way and for specific regions, how we might assess the effects of clouds on this longwave cooling although it is clear that a more global assessment must await use of new satellite data that will allow us to estimate the contributions by clouds to the surface longwave fluxes and therefore to the column heating rates in a meaningful way.

The major results and conclusions of this study are as follows: 1. SAMSON simulations of the clear sky longwave fluxes to space and to the surface are employed in this study to assist in development of a retrieval of F_g. Simulations of the flux to space, F_∞, as reported

previously by *Slingo and Webb* [1992], generally match the ERBE estimates of the same fluxes within 5–10 W m^{-2} with a small bias (of approximately 3 W m^{-2}) which also happens to be of a similar magnitude and sign of a reported bias in the ERBE clear sky flux data [*Harrison et al.*, 1988]. The uncertainty in the SAMSON clear sky monthly mean F_g is also probably of the order of 10 W m^{-2} although we have little data to confirm this uncertainty.

2. A new relationship between the ratio of F_g and F_∞ and the column water vapor w is introduced. This relationship is derived over ocean surfaces that emit as an assumed blackbody. It is demonstrated using the SAM-

SON results how this ratio is approximately linear when $w > 20$ kg m^{-2}, as predicted by graybody radiative equilibrium arguments. When the water vapor amount is below 20 kg m^{-2}, the relationship, while still distinct, takes on a nonlinear curve of growth form. Independent surface longwave flux measurements, combined with F_∞ simulated using measured radiosonde temperature and moisture profiles in a radiative transfer model, confirm the existence of this general flux ratio–w relationship. The extent to which this relationship exists over land is not explored in this study, although it is likely that the relation will break down over surfaces of variable emissivity such as may occur over arid land regions.

3. A simple linear fit applied over the range $w > 20$ kg m^{-2} was carried out to determine the slope and intercept coefficients. The values of these coefficients, together with SSM/I observations of w and ERBE observations of the clear sky F_∞, are used to obtain monthly mean values of F_g over the oceans. Examples of the results of this simple retrieval are presented and contrasted with those from SAMSON and the rms difference between the retrieved and the simulated fluxes is ±6 W m^{-2}, which is considerably smaller than the uncertainty presently expected from the direct radiometric measurements of this flux.

4. We use our retrieval of F_g from satellite measurements of F_∞ and w together with climatological values of surface pressure and SST to arrive at monthly mean distributions of the column–averaged clear sky longwave heating rates and propose that this heating rate has an uncertainty of approximately ±0.2 K d^{-1}. These column heating rates, when contrasted with the SSM/I fields of w that were used to produce them, demonstrate a systematic increase (in cooling) as w increases in an almost linear manner, as predicted by a simple analysis given in this paper. Under moist conditions, where $w > 40$ kg m^{-2}, the rate of growth of cooling with increasing w slightly decreases due to a decreasing sensitivity of F_∞ with increasing w. However, when viewed as a function of SST rather than as a function of w, the column cooling rate dramatically increases with increasing SST. This is shown to be due to the increase of emission from the atmosphere to the surface associated with increasing w which is linked to the increasing SST. We deduce that this increase in the flux emitted from the atmosphere is more than twice the rate of increase of the flux emitted from the surface.

5. Upper and lower bounds on the effects of clouds on the column cooling rate of the atmosphere are established and, furthermore, we demonstrate how the longwave effects of clouds in a moist atmosphere where the column water vapor exceeds approximately 30 kg m^{-2} may be estimated from presently available satellite data with an uncertainty estimated to be not significantly larger than 0.2 K d^{-1}. Based on the approach described in section 6, we show how clouds in these relatively moist regions decrease the column cooling by almost 50 % of the clear sky values and how we infer the presence of significant longitudinal gradients in column radiative heating across the equatorial and subtropical Pacific Ocean.

References

Cess, R. D., E. G. Dutton, J. J. Deluisi, and F. Jiang, Determining surface solar absorption from broadband satellite measurements for clear skies: Comparison with surface measurements, *J. Clim.*, 4, 236–247, 1991.

Clough, S. A., F. X. Kneizys, L. S. Rothman, G. P. Anderson, and E. P. Shettle, Current issues in infrared atmospheric transparency, in *Atmospheric Transparency for Satellite Applications*, edited by G.V. Silvestini, CUEN, Capri, Italy, 1986.

Cornwall, C. R., C. L. Combs, J. M. Davis, G. L. Stephens, and S. K. Cox, CSU Radiation Budget pilot study for TOGA COARE, *CSU Atmos. Sci. Pap. 532*, 57 pp., Colo. State Univ., Fort Collins, 1993.

Dutton, E. G., An extended comparison between LOWTRAN7 computed and observed broadband thermal radiances: Global extreme and intermediate surface conditions, *J. Atmos. Oceanic Technol.*, 10, 326–336, 1993.

Ellingson, R. G., J. Ellis, and S. Fels, The intercomparison of radiation codes in climate models: Longwave results, *J. Geophys. Res.*, 96, 8929–8953, 1991.

Greenwald, T., G. L. Stephens, T. VonderHaar, and D. Jackson, A physical retrieval of cloud liquid water over the global oceans using SSM/I observations, *J. Geophys. Res.*, 98, 18,471-18,488, 1993.

Gupta S., W. L. Darnell, and A. C. Wilber, A parameterization for longwave surface radiation from satellite data: Recent improvements, *J. Appl. Meteorol.*, 31, 194–211, 1992.

Harrison, E. F., D. R. Brooks, P. Minnis, B. A. Wielicki, W. F. Staylor, G. G. Gibson, D. F. Young, F. M. Denn, and the ERBE Science Team, First estimates of the diurnal variation of longwave radiation from the multiple–satellite Earth Radiation Budget Experiment (ERBE), *Bull. Am. Meteorol. Soc.*, 69, 1144–1151, 1988.

Hollinger, J., R. Lo, C. Poe, R. Savage, and J. Pierce, Special Sensor microwave/imager user's guide, *NRL Rep.*, Nav. Res. Lab., Washington, D. C., 1987.

House, F. B., A. Gruber, G. Hunt, and A. T. Mecherikunnel, History of satellite missions and measurements of the Earth Radiation Budget (1957–1984), *Rev. Geophys.*, 24, 357–377, 1986.

Liu, W. T., T. Wang, and F. Wentz, Precipitable water and

surface humidity over the global oceans from SSM/I and ECMWF, *J. Geophys. Res.*, *97*, 2251-2264, 1992.

Manabe, S., and R. T. Wetherald, Thermal equilibrium of the atmosphere with a given distribution of relative humidity, *J. Atmos. Sci.*, *24*, 241-259, 1967.

McClatchey, R. A., R. W. Fenn, J. C. Selby, F. E. Volz and J. S. Goring, *Optical Properties of the Atmosphere*, 3rd ed., 107 pp., Air Force Cambridge Res. Labs, 1972.

Minnett, P. J., Surface oceanographic and atmospheric measurements made during the Mediterranean Aircraft-Ship Transmission Experiment (MASTEX) from the R/V *Alliance*, *SACLANT Cent. Memo.*, *SM-264*, 131 pp. SACLANT Undersea Res. Cent., La Spezia, Italy, 1992.

Minnett, P. J., Measurement for satellite validation made from the RV Alliance during October and November 1991, *SACLANT Cent. Memo.*, *SM-273*, 268 pp. SACLANT Undersea Research Centre, La Spezia, Italy, 1993.

NEWATER Steering Committee and Principal Investigators, Collaborative research on the Northeast Water Polynya: Initial results from the 1992 *polar sea* cruise, *ES Trans. AGU.*, *74*, 185 and 195-196, 1993.

Pinker, R. T., and I. Laszlo, Modeling surface solar irradiance for satellite applications on a global scale, *J. Appl. Meteorol.*, *31*, 194-211, 1992.

Ramanathan, V., B. R. Barkstrom, and E. F. Harrison, Climate and the Earth's Radiation Budget, *Phys. Today*, 22-32, 1989.

Randall, D.A., et al., Intercomparison and interpretation of surface energy fluxes in atmospheric general circulation models, *J. Geophys. Res.*, *97*, 3711-3724, 1992.

Reynolds, R. W., A real-time global sea surface temperature analysis, *J. Clim.*, *1*, 75-86, 1988.

Rodgers, C. D., The use of emissivity in atmospheric radiation calculations, *Q. J. R. Meteorol. Soc.*, *93*, 43-54, 1967.

Sabatini, R. R., and V. E Suomi, On the possibility of atmospheric infrared cooling estimates from satellite observations, *J. Atmos Sci.*, *19*, 349-350, 1962.

Schmetz, J., Towards a surface radiation climatology: Retrieval of downward irradiance from satellites , *Atmos. Res.*, *23*, 287-321, 1989.

Shine, K. P., On the cause of the relative greenhouse strength of gases such as halocarbons, *J. Atmos. Sci.*, *48*, 1513-1518, 1991.

Shine, K. P., and A. Sinha, Sensitivity of the Earth's climate to height dependent changes in the water vapor mixing ratio, *Nature*, *354*, 382-384, 1991.

Slingo, A., and J. M. Slingo, The response of a general circu-

lation model to cloud longwave radiative forcing. I. Introduction and initial experiments, *Q. J. R. Meteorol. Soc.*, *114*, 1027-1062, 1989.

Slingo, A., and M. J. Webb, Simulation of clear sky outgoing longwave radiation over the oceans using operational analyses, *Q. J. R. Meteorol. Soc.*, *118*, 1117-1144, 1992.

Stackhouse, P. W., Jr., and G. L. Stephens, A theoretical and observational study of the radiative properties of cirrus: Results from FIRE 1986, *J. Atmos. Sci.*, *48*, 2044-2059, 1991.

Stephens, G.L., On the relationship between water vapour over the oceans and sea surface temperature. *J. Clim.*, *3*, 634-645, 1990.

Stephens, G. L., and T. J. Greenwald, Observations of the Earth's Radiation Budget in Relation to Atmospheric Hydrology, 1, Clear sky greenhouse effect and water vapor feedback, *J. Geophys.Res.*, *96*, 15,311-15,324, 1991a.

Stephens, G. L., and T. J. Greenwald, Observations of the Earth's Radiation Budget in relation to atmospheric hydrology, 2, Cloud effects and cloud feedback, *J. Geophys. Res.*, *96*, 15,325-15,340, 1991b.

Stephens, G. L., D. A. Randall, I. L. Wittmeyer, and D.A. Dazlich, Observations of the Earth's Radiation Budget in relation to atmospheric hydrology, 3, Comparison of observations over oceans with a GCM, *J. Geophys. Res.*, *98*, 4931-4950, 1993.

Stephens, G.L., D.L. Jackson and J.J Bates, A comparison of SSM/I and TOVS column water vapor data over global oceans, *Meteorol. Atmos. Phys.*, in press, 1994.

Webb, M.J., A. Slingo, and G.L. Stephens, Seasonal variations of the clear sky greenhouse effect: The role of changes in atmospheric temperatures and humidities, *Clim. Dyn.*, *9*, 117-129, 1993.

P.H. Daum and L. Kleinman, Environmental Chemistry Division, Brookhaven National Laboratory, Upton, NY 11973-5000.

P.J. Minnett, Oceanographic and Atmospheric Sciences Division, Brookhaven National Laboratory, Upton, NY 11973-5000.

D.A. Randall, G.L. Stephens, and I. Wittmeyer, Department of Atmospheric Sciences, Colorado State University, Fort Collins, CO 80523.

A. Slingo and M.J. Webb, Hadley Center for Climate Prediction and Research, Meteorological Office, Bracknell, England.